

AD-A141 943

AFATL-TR-83-90

Generalized Roughness Effects on Turbulent Boundary Layer Heat Transfer

A Discrete Element Predictive Approach for Turbulent Flow Over Rough Surfaces

Hugh W Coleman
B Keith Hodge
Robert P Taylor

MISSISSIPPI STATE UNIVERSITY
DEPT OF MECHANICAL & NUCLEAR ENGINEERING
P O DRAWER ME
MISSISSIPPI STATE, MISSISSIPPI 39762

NOVEMBER 1983

FINAL REPORT FOR PERIOD NOVEMBER 1981-SEPTEMBER 1983

Approved for public release; distribution unlimited



Air Force Armament Laboratory
AIR FORCE SYSTEMS COMMAND * UNITED STATES AIR FORCE * EGLIN AIR FORCE BASE, FLORIDA

SEARCHED
SERIALIZED
MAY 29 1984

84 05 28 020

A

DTIC FILE COPY

NOTICE

Please do not request copies of this report from the Air Force Armament Laboratory. Additional copies may be purchased from:

**National Technical Information Service
5285 Port Royal Road
Springfield, Virginia 22161**

Federal Government agencies and their contractors registered with Defense Technical Information Center should direct requests for copies of this report to:

**Defense Technical Information Center
Cameron Station
Alexandria, Virginia 22314**

20. ABSTRACT (CONCLUDED)

equations which describe momentum and energy transport in turbulent flows. The model includes the necessary empirical information on the interaction between the roughness elements and the flow around and between the elements in a general way which does not require experimental data on each specific surface. This empirical information is input via algebraic models for the local element drag coefficient and Nusselt number. These models have been calibrated by comparison with base data sets from surfaces with three-dimensional (distributed) roughness elements.

Calculations using the present discrete element model are compared with experimental data from 118 separate experimental runs. The results of these comparisons range from good to excellent. The calculations are shown to compare equally well with both transitionally rough turbulent flow and fully rough turbulent flow without modification of the roughness model.

In the course of the present work it was discovered that the definitive data set of Schlichting is flawed. Corrected values are presented for this data set.

TABLE OF CONTENTS

Section	Title	Page
I.	INTRODUCTION	1
	1. Prediction Approaches	1
	2. Objective	3
	3. Contents	3
II.	BACKGROUND	4
	1. Equivalent Sand-Grain Roughness	7
	2. The Discrete Element Approach	15
III.	DERIVATION OF THE DISCRETE ELEMENT MODEL	20
	1. Derivation of the Boundary Layer Equations	21
	2. Quantification of Roughness Geometry	31
	a. Uniform Arrays	31
	b. General Roughness	34
	3. Empirical Closure	37
	a. Turbulence Model	37
	b. Roughness Model	38
	4. Remarks on the Discrete Elements Model	38
	5. Definition of Skin Friction, Stanton Number, Integral Length Scales, and the Element Temperature	39
IV.	METHOD OF SOLUTION	41
	1. Equations and Boundary Conditions	41
	2. The Modified Illingsworth Transformation	42
	3. The Implicit Finite Difference Method	45
	4. Fully Developed Flows	51
	5. Computer Program	51
V.	CALIBRATION OF THE MODEL	53
	1. Smooth Surface Runs	53
	2. Momentum Transport Model	53
	3. Wall Location for Most Densely Packed Spheres	56
	4. Energy Transport Model	59
VI.	FULLY DEVELOPED FLOW RESULTS	61
	1. Schlichting's Experiment	61
	2. Chen's Experiment	67

TABLE OF CONTENTS (CONCLUDED)

Section	Title	Page
VII.	BOUNDARY LAYER FLOW RESULTS	72
	1. Description of the Stanford Experiments . . .	72
	2. Application of the Discrete Element Model . .	72
	3. Comparisons with the Data of Healzer and Pimenta	73
	4. Comparisons with the Data of Coleman	74
VIII.	SUMMARY, CONCLUSIONS, AND RECOMMENDATIONS	96
	1. Summary	96
	2. Conclusions	97
	3. Recommended Future Research	98
	REFERENCES	99
Appendix		
A.	REEVALUATION OF SCHLICHTING'S SURFACE ROUGHNESS EXPERIMENT	103
	1. Schlichting's Experiment	103
	2. Schlichting's Evaluation of C_f	106
	3. Reevaluation of C_f	107
	4. Reevaluation of Equivalent Sand Roughness . .	114
B.	INTEGRAL BOUNDARY LAYER EQUATIONS FOR FLOW OVER A ROUGH WALL	117
C.	ON THE PROBLEM OF ROUGHNESS ELEMENT TEMPERATURE . .	121

LIST OF FIGURES

Figure	Title	Page
1.	Plot of Nikuradse's [1] Friction Factor Data Versus Pipe Reynolds Number	5
2.	Typical Velocity Profiles for a Fully Rough Turbulent Boundary Layer in Zero Pressure Gradient	10
3.	Effective Sand-Grain Roughness Correlation of Dirling [13]	12
4.	Schematic of a Rough Surface	16
5.	General Layout of Control Volume	22
6.	Mass Balance Control Volume	23
7.	Momentum Balance Control Volume	25
8.	Energy Balance Control Volume	27
9.	Local Element Diameters for Cones, Spheres and Spherical Segments	32
10.	Layout for Averaging α_x	33
11.	Typical Profilometer Traces	34
12.	Layout of the Expanding Finite Difference Grid.	45
13.	Matrix Form of Linearized Equations; a) Tridiagonal Form, b) Canonical Form	49
14.	Comparison of Calculations with the Smooth Wall Data of Kearney [36]; $U_e = 7$ m/s	54
15.	Roughness Element Drag Coefficient Model . . .	57
16.	Schematic of Most Densely Packed Spheres . . .	58
17.	Roughness Element Nusselt Number Model	60
18.	Comparison of Calculations with the Corrected Skin Friction Data of Schlichting for Spheres .	64
19.	Comparison of Calculations with the Corrected Skin Friction Data of Schlichting for Spherical Segments	65
20.	Comparison of Calculations with the Corrected Skin Friction Data of Schlichting for Cones . .	65

LIST OF FIGURES (CONTINUED)

Figure	Title	Page
21.	The Effect of Roughness Element Spacing on Skin Friction for Schlichting's Spheres; Re \approx 200,000	66
22.	Comparison of Calculations with the Data of Chen; $l/k = 18.5$	68
23.	Comparison of Calculations with the Data of Chen; $l/k = 10.7$	69
24.	Comparison of Calculations with the Data of Chen; $l/k = 6.4$	70
25.	Comparison of Calculations with the Data of Healzer; $U_e = 9.75$ m/s	75
26.	Comparison of Calculations with the Data of Pimenta; $U_e = 15.8$ m/s	76
27.	Comparison of Calculations with the Data of Pimenta; $U_e = 27$ m/s	77
28.	Comparison of Calculations with the Data of Pimenta; $U_e = 39.6$ m/s	78
29.	Comparison of Calculations with the Data of Healzer; $U_e = 58$ m/s	79
30.	Comparison of Calculations with the Data of Healzer; $U_e = 74$ m/s	80
31.	Typical Comparison of Calculated and Measured Velocity Profiles; Pimenta, $U_e = 27$ m/s	81
32.	Typical Comparison of Calculated and Measured Temperature Profiles; Pimenta, $U_e = 27$ m/s	81
33.	Typical Comparison of Calculated and Measured Reynolds Stress; Pimenta, $U_e = 27$ m/s	82
34.	Typical Comparison of Calculated and Measured Turbulent Heat Flux; Pimenta, $U_e = 27$ m/s	82
35.	Edge Velocity Distributions for Coleman's Equilibrium Pressure Gradient Runs	84

LIST OF FIGURES (CONTINUED)

Figure	Title	Page
36.	Comparison of Calculations with the Data of Coleman; $K_r = 0.15 \times 10^{-3}$; Constant Wall Temperature	85
37.	Comparison of Calculations with the Data of Coleman; $K_r = 0.29 \times 10^{-3}$; Constant Wall Temperature	86
38.	Comparison of Calculations with the Data of Coleman; $K_r = 0.5 \times 10^{-3}$; Constant Wall Temperature	87
39.	Comparison of Calculations with the Data of Coleman; $K_r = 0.15 \times 10^{-3}$; First Six Plates Unheated	88
40.	Edge Velocity Distribution for Coleman's Nonequilibrium Pressure Gradient Run; $K = 0.28 \times 10^{-6}$	89
41.	Comparison of Calculations with the Data of Coleman; Nonequilibrium Run; Constant Wall Temperature	90
42.	Comparison of Calculations with the Data of Coleman; Nonequilibrium Run; First Six Plates Unheated	91
43.	Wall Temperature Distribution for the Data of Coleman; Both Cases with Zero Pressure Gradient .	92
44.	Comparison of Calculations with the Data of Coleman; Linear Wall Temperature Distribution . .	93
45.	Comparison of Calculations with the Data of Coleman; Bi-linear Wall Temperature Distribution.	94
46.	Typical Comparison of Calculated and Measured Reynolds Stress for Coleman's Equilibrium Pressure Gradient Run; $K_r = 0.29 \times 10^{-3}$	95
A-1.	Nomenclature for Schlichting's Experiment	104
A-2.	Rough Wall Coordinate System Definitions	104

LIST OF FIGURES (CONCLUDED)

Figure	Title	Page
A-3.	Demonstration of Influence of Effective Wall Location on Skin Friction Calculated From Velocity Profile Slope; Plate III, $Re \approx 107,000$.	112
A-4.	Standard Error of Estimates for Velocity Profile Regressions for the Effective Wall Locations in Figure A-3	113
C-1.	Roughness Element Heat Transfer Schematic and Nomenclature	123

LIST OF TABLES

Table	Title	Page
1.	Comparison with Schlichting's Results	62
A-1.	Description of Schlichting's Surface Roughness and Corrected Equivalent Sand-Grain Roughness . .	105
A-2.	Comparison of Original and Corrected Skin Friction Coefficients	108

NOMENCLATURE

A^+	Van Driest Damping factor
A_e	Roughness element heat transfer area; Equation (14)
A_p	Projected frontal area
A_x	Area open to x-direction flow; Figure 5
A_y	Area open to y-direction flow; Figure 5
C_D	Drag coefficient
C_f	Skin friction coefficient; $2\tau_w/\rho U_e^2$
C_p	Specific heat at constant pressure
$d(y)$	Local element diameter
Ec	Eckert number; Equation (21)
f	Stream function; Equation (48)
F_D	Drag force on roughness elements
g	Enthalpy ratio; h/h_e , H/H_e
h	Specific enthalpy
H	Time mean specific enthalpy
K	Thermal conductivity; also $(\nu/U_e^2)(dU_e/dx)$
k	Roughness element height
K_r	Boundary layer pressure gradient parameter, $(\frac{1}{2} k/U_e)(dU_e/dx)$
k_s	Equivalent sand-grain roughness
L	Roughness element spacing in x-direction; Figure 5
l	Roughness element spacing in z-direction; Figure 5
l_m	Prandtl mixing length; Equation (34)
L_x	Profilometer trace length in x-direction
L_z	Profilometer trace length in z-direction
$N_x(y)$	Number of elements in x-profilometer trace at y-location
$N_z(y)$	Number of elements in z-profilometer trace at y-location
Nu_d	Local roughness element Nusselt number
p	Pressure
P	Time mean pressure
Pr	Prandtl number
Q	Rate of heat transfer to a roughness element
q_y	Local heat flux
R	Geometrically expanding grid parameter

NOMENCLATURE (CONTINUED)

Re	Reynolds number
Re _{k_s}	Roughness Reynolds number; u^*k_s/ν
Re _d	Reynolds number based on local element diameter; $Ud(y)/\nu$
St	Stanton number; Equation (39)
t	Temperature
T	Time mean temperature
u	Velocity component in x-direction
U	Time mean value of u
u*	Friction velocity; $\sqrt{\tau_w/\rho}$
U _{ave}	Average velocity in a conduit
U _{max}	Maximum velocity in a conduit
v	Velocity component in the y-direction
V	Time averaged value of v
x	Streamwise coordinate
y	Normal coordinate
y ⁺	Nondimensional y; yu^*/ν
z	Transverse coordinate

Greek

α_x	Blockage factor for a surface normal to the x-direction
α_y	Blockage factor for a surface normal to the y-coordinate
β_x	Blockage factor; $= (1 - \alpha_x)$
β_y	Blockage factor; $= (1 - \alpha_y)$
δ	Boundary layer thickness
δ^*	Displacement thickness; Equation (B-17)
δ_d	Dissipation thickness; Equation (B-15)
δ_h	Enthalpy thickness; Equation (B-14)
δ_{h_0}	Stagnation enthalpy thickness; Equation (B-19)
δ_T	Thermal boundary layer thickness
η	Transformed coordinate; Equation (46)
θ	Momentum thickness; Equation (B-6)
κ	Von Karman constant; taken as $\kappa = 0.4$
μ	Viscosity
ν	Kinematic viscosity

NOMENCLATURE (CONCLUDED)

ξ	Transformed coordinate; Equation (45)
ρ	Density
τ	Shear stress
ψ	Stream function; Equation (47)

Subscripts

c	Corrected value
e	Values at the edge of the boundary layer
R	Roughness element values
r	Rough surface values
s	Smooth surface values
T	Turbulent values
w	Values at the wall

Superscripts

'	Turbulent fluctuating values
---	------------------------------

SECTION I
INTRODUCTION

The skin friction and heat transfer can be significantly larger for turbulent flow over a rough surface as compared with an equivalent turbulent flow over a smooth surface. Many surfaces of engineering interest are rough in the aerodynamic or hydraulic sense (to be defined in the following sections). Examples of systems for which surface roughness is an important concern are re-entry vehicles, missiles, stores carried externally on high performance aircraft, ships' hulls, turbines, heat exchangers, piping networks, and atmospheric flows. In light of this broad interest and applicability, there is a significant interest in accurate predictive models for turbulent flow over a rough surface.

1. PREDICTION APPROACHES

Some possible schemes for predicting the momentum and enthalpy fields (and by consequence the skin friction and heat transfer) for turbulent flow over a rough surface are:

1. Solve the complete unsteady Navier-Stokes equations in a micro-grid.
2. Solve the time-averaged Navier-Stokes equations in a micro-grid.
3. Solve the time-averaged Navier-Stokes equations in a macro-grid.
4. Solve the time-averaged boundary layer equations in a macro-grid.

The first scheme is a one-hundred percent first principles approach. The complete set of descriptive equations is solved numerically in a grid system that is fine enough to resolve the details of both the turbulence and the geometry of the rough surface. Such an effort would be well beyond the state of the art. The computer storage and computational time required for such an effort would be astronomical.

The second scheme does not attempt to temporally resolve the turbulent fluctuations but does use a grid network that is fine enough to resolve the geometry of the rough surface. The grid for such a scheme

would still be beyond the present computer storage capabilities. For this scheme a turbulent closure model would be required since the time averaging process introduces new variables (the so-called Reynolds stresses) but, unfortunately, no new equations. Therefore, empirical inputs are required to close the system of equations.

The third scheme does not attempt to resolve either the temporal details of the turbulent fluctuations or the minute details of the rough surface geometry. That is, the numerical finite difference grid is coarse compared with the scales of the turbulence and of the roughness. This relatively coarse grid allows the problem to be placed on current large computers. Here, as in the second scheme, a turbulent closure model is required. Also, since the details of the roughness geometry are not resolved, some form of roughness model must be introduced to account for the effect of the roughness on the flow field.

The fourth set is actually a subset of the third and is mentioned here for completeness. The well-known boundary layer approximations lead to a simplified version of the Navier-Stokes equations, the so-called boundary layer equations. These equations are parabolic as opposed to the elliptic Navier-Stokes equations and are readily solved by many computer codes. Here, as with the third scheme, both a turbulence closure model and a roughness model are required. Because of the simplification mentioned above, the boundary layer equations offer comparative computational efficiency. Also, many flows of engineering interest meet the boundary layer assumptions. Furthermore, it should be pointed out that as turbulence closure models that were developed for boundary layers are readily extended to turbulent Navier-Stokes calculations, so too would be roughness models that are developed for boundary layers.

From the above discussion it is apparent that, if the flow over a rough surface is to be computed, some efficient, accurate roughness model must be supplied. There are two main schools of thought on the modeling of rough surfaces that are discussed in detail in Section II. They are: (1) a wholly empirical method known as the equivalent sand-grain approach, and (2) a semi-empirical method known as the discrete element approach. While both methods require experimental inputs, the equivalent sand-grain approach may require experimental data on the particular surface under consideration. On the other hand, the discrete element

approach incorporates more basic physics of the process and uses a more generalized empirical input. It is therefore applicable to a broader spectrum of rough surfaces without requiring specific experimental data.

2. OBJECTIVE

The objective of the present work was to develop and verify a predictive model for turbulent flow over rough surfaces consisting of distributed (or three-dimensional) roughness elements. The desired model should:

1. Accurately predict both skin friction and heat transfer.
2. Not require a data base for each particular surface under consideration.

3. CONTENTS

The general organization of the work presented in this report is described below. Section II is a discussion of the background of predictive methods for turbulent flow over rough surfaces. The present predictive model is derived and discussed in Section III. In Section IV the method of solution is presented and discussed. The calibration of the present model is given in Section V. In Section VI the results of the present model are compared with experimental data for fully developed flow. In Section VII the results of the model are compared with experimental data for developing boundary layers. The conclusions of the work and recommendations are contained in Section VIII.

Ancillary information is contained in the appendices.

SECTION II

BACKGROUND

The rigorous study of the effects of surface roughness on fluid flow and heat transfer had its origin with the classic work of Nikuradse [1] in 1933. He took pressure drop and velocity profile measurements in pipes roughened with tightly sized grains of "Goettingen" sand. He made an extensive number of experimental runs covering 6 sand grain sizes ($r/k_s = 15, 30.6, 60, 126, 252, 507$; where r is the pipe radius and k_s is the sand grain size) and pipe Reynolds numbers ranging from 500 to 1,000,000. Inspection of Figure 1, which shows a plot of Nikuradse's friction factor versus Reynolds number, reveals the magnitude of this data base. In this paper Nikuradse introduced the roughness Reynolds number as a measure of the state of the flow over the rough surface

$$Re_{k_s} = u^*k_s/\nu \quad (1)$$

where u^* is the friction velocity ($\sqrt{\tau_w/\rho}$) and k_s is the size of the sand grains. He also documented the three regimes of rough surface flow:

hydraulically smooth	$Re_{k_s} < 5$
transitionally rough	$5 < Re_{k_s} < 55 - 70$
fully rough	$Re_{k_s} > 55 - 70$

Hydraulically (or aerodynamically) smooth flow is flow over a rough surface that has the same resistance as flow over a smooth surface at the same Reynolds number. That is, the surface appears smooth to the fluid. It is characterized by the skin friction coefficient depending on the Reynolds number of the gross flow but not depending on the roughness size, shape, density, etc. Fully rough flow is flow where the skin friction coefficient does not depend on the Reynolds number of the gross flow and does depend solely on the character of the roughness. Transitionally rough flow (not to be confused with the transition between laminar and turbulent flow) is, as its name suggests, between hydraulically smooth and fully rough. It is characterized by dependence of the skin friction coefficient on both flow Reynolds number and roughness character.

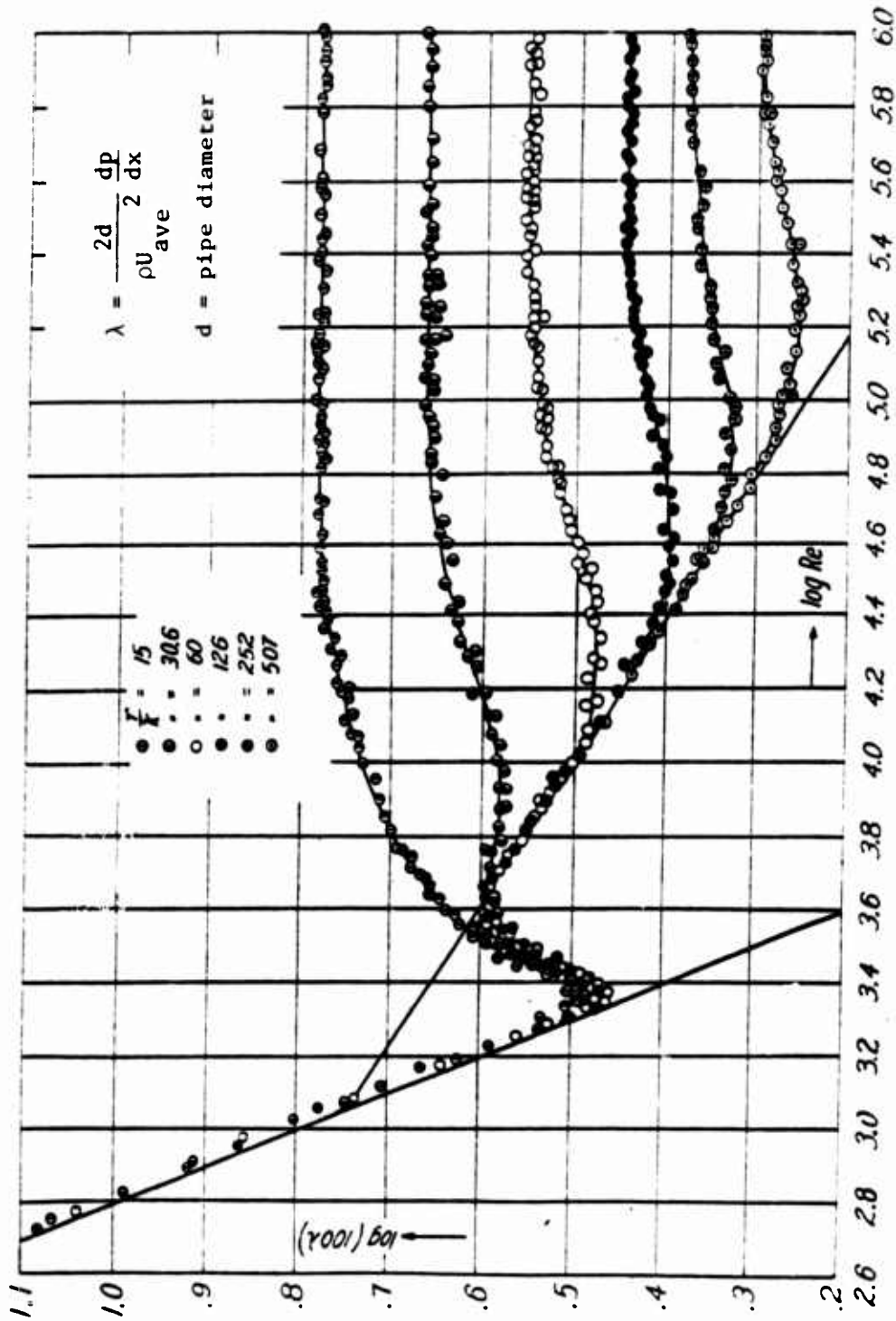


Figure 1. Plot of Nikuradse's [1] Friction Factor Data Versus Pipe Reynolds Number

These three regimes are usually explained in terms of the relationship between the roughness height and the so-called viscous sublayer. It is said that in the hydraulically smooth regime the roughness elements are all within the sublayer; therefore, viscous effects dominate and the surface appears smooth to the flow. In the transitionally rough regime the roughness elements begin to protrude through the sublayer and both viscous and roughness effects are significant. Finally, in the fully rough regime the sublayer is said to be fully destroyed and viscous effects become insignificant; hence, the Reynolds number is no longer a factor.

The sublayer explanation, while enlightening, depends almost completely on the height of the roughness and ignores the important factors of shape and spacing density of the roughness elements. An otherwise smooth surface with very sparsely spaced large (relative to the sublayer) elements may appear smooth to the flow. Morris [2] took a different view that was based more on the spacing of the elements than the height. He classed flow over a rough surface into four regimes: smooth, semismooth, hyperturbulent (wake interference), and quasismooth. The smooth regime is equivalent to the hydraulically smooth regime discussed above. The semismooth regime consists of a mostly smooth surface with very sparsely spaced roughness elements. The flow resistance is viewed as a sum of the viscous resistance on the smooth parts of the surface and the pressure drag on the roughness elements. Hyperturbulent flow consists of a surface where the elements are more closely spaced and the wakes behind the elements reach the adjacent elements. Quasismooth flow consists of elements so closely packed that the crests of the elements and the nearly stagnant fluid in the intermediate pockets form an almost smooth surface.

Following Nikuradse's work, the next major step in the development of the theory of flow over rough surfaces was the definitive paper by Schlichting [3] in 1936. Schlichting conducted experiments in a rectangular channel with the upper surface roughened and the remaining sides smooth. His purpose was to study the effects of roughness shape and density on the flow resistance. He investigated seven different shapes: large spheres, small spheres, spherical segments, cones, short angles, long angles, and a "Hamburg" sand. Each shape was studied over a range

of spacings and a limited range of Reynolds numbers. Schlichting's paper is definitive for two reasons: (1) it remains the most comprehensive set of controlled experiments for flow over a well-defined rough surface, and (2) two methods of viewing the roughness problem were put forward. In this paper Schlichting developed in detail the well-known equivalent sand-grain roughness approach and briefly discussed an alternative approach that has come to be known as the discrete element approach.

1. EQUIVALENT SAND-GRAIN ROUGHNESS

To adequately describe a rough surface at least three measures are required: height, spacing density, and shape. In general, a multiplicity of length scales are required (k_1, k_2, \dots, k_n , where the number n will vary from surface to surface). Simplicity has been a powerful incentive in past attempts to use a single length scale to describe the nature of rough surfaces. The parameter that is most commonly used is the well-known equivalent sand-grain roughness, k_s .

In his paper Schlichting [3] proposed the equivalent sand-grain roughness as a measure of the flow resistance character of a rough surface. This measure was a length scale, k_s , which was the sand-grain size in Nikuradse's experiment that gave the same flow resistance at the same Reynolds number based on hydraulic radius. It was Schlichting's stated purpose to use this measure only as a means of extrapolating a restricted set of experimental resistance data to other Reynolds numbers based on Nikuradse's extensive data set. To quote the NACA translation [3]:

"It is the object of our test to be able to specify for each type of roughness investigated a characteristic number by whose aid it becomes possible to predict the resistance for the same type of roughness at other Reynolds numbers... than those directly measured."

"...it appeared advantageous to us to evaluate our results in such a manner that they could easily be expressible in terms of results obtained by Nikuradse for sand roughness without, however, necessarily taking the latter as a standard type of roughness. One objection to using sand roughness as a standard is that this type is not satisfactorily reproducible...."

Schlichting's admonition about the reproducibility of sand-type roughness was most likely prompted by his experience with the "Hamburg"

sand. One of Schlichting's roughness media was a sand that he designated "Hamburg" as compared to the "Goettingen" sand that was used by Nikuradse. The "Hamburg" sand was sized in the same manner that Nikuradse used and was bonded to the surface in the same manner as Nikuradse. For the "Hamburg" sand Schlichting determined an equivalent sand grain roughness $k_s/k = 1.64$ (where here k is the size of the "Hamburg" sand). That is, the "Hamburg" sand was 64% rougher than the same size "Goettingen" sand. Schlichting also tested a "Goettingen" sand and found that the friction factor differed only 1 to 2% from those found by Nikuradse; therefore, the difference cannot be attributed to differences in the experimental methods. This is a graphic counterexample to the widely held belief that surfaces that are densely roughened with sand or that appear sand-grain-like (e.g., grit blasted) scale on a one-to-one basis with Nikuradse's sand roughness.

The equivalent sand-grain roughness, k_s , is usually determined by measuring the skin friction and velocity profiles for a particular surface and then comparing these results with the results of Nikuradse [1]. For example, Schlichting [3] determined his values for k_s in the following manner. He started with the logarithmic velocity profile given by Nikuradse for fully rough flow

$$\frac{u}{u^*} = 5.75 \log \frac{y}{k_s} + 8.48 \quad (2)$$

where y is the distance from the surface. Then he assumed that his velocity profile over a surface of elements with uniform height, k , could be fit by the formula

$$\frac{u}{u^*} = 5.75 \log \frac{y}{k} + A \quad (3)$$

Schlichting determined the friction velocity independently, basically by using pressure drop measurements. The intercept A was determined by graphically fitting equation (3) to the measured velocity profile. Then by setting the right-hand sides of equations (2) and (3) equal to each other he obtained

$$5.75 \log \frac{k_s}{k} = 8.48 - A \quad (4a)$$

or

$$\frac{k_s}{k} = 10^{(8.48 - A)/5.75} \quad (4b)$$

This method is not as straightforward as it appears. The reader no doubt recognizes the similarity between equations (2) and (3) and the well-known law of the wall for turbulent flow over smooth surfaces

$$\frac{u}{u^*} = 5.75 \log \frac{yu^*}{\nu} + 5.5 \quad (5)$$

This similarity is not coincidental. In their formulations of equations (2) and (3) Nikuradse and Schlichting both assumed that the effects of roughness are confined to a region very near the wall; therefore, the slope of the logarithmic region of the velocity profile is the same for both rough and smooth surfaces (the only difference being in the intercept). This argument is based on skin friction and mean velocity measurements along with a somewhat nebulous definition of the origin for the y-axis. Recent extensive measurements (Pimenta [4], Coleman [5] and Ligrani [6]) have shown that roughness affects both the magnitude and spectral distribution of turbulent kinetic energy across the entire boundary layer, suggesting that the slope of the logarithmic region could be different for smooth and rough surfaces. Furthermore, Uram [7] has determined logarithmic region slopes ranging from 4 to 9 for different rough surfaces.

The appropriate origin for the distance from the wall, y, must be selected if the velocity profile is to have a logarithmic region of the form of equation (3). Schlichting used the melt down location as the origin for the y-axis in his work. That is, he used the surface that would result if all the elements were melted and the melt was allowed to distribute itself evenly. This method yields a hypothetical surface that maintains the same fluid volume. This location, while it appears logical, has no physical basis from a fluid dynamics viewpoint. Figure 2 shows the resulting velocity profile plots with different y-axis origins for a surface that consists of densely packed spheres [5]. Inspection of the figure reveals that different (but apparently valid from visual inspection) logarithmic profiles exist for each of the y-axis origins. Therefore, the mere fact that a logarithmic region seems to exist does

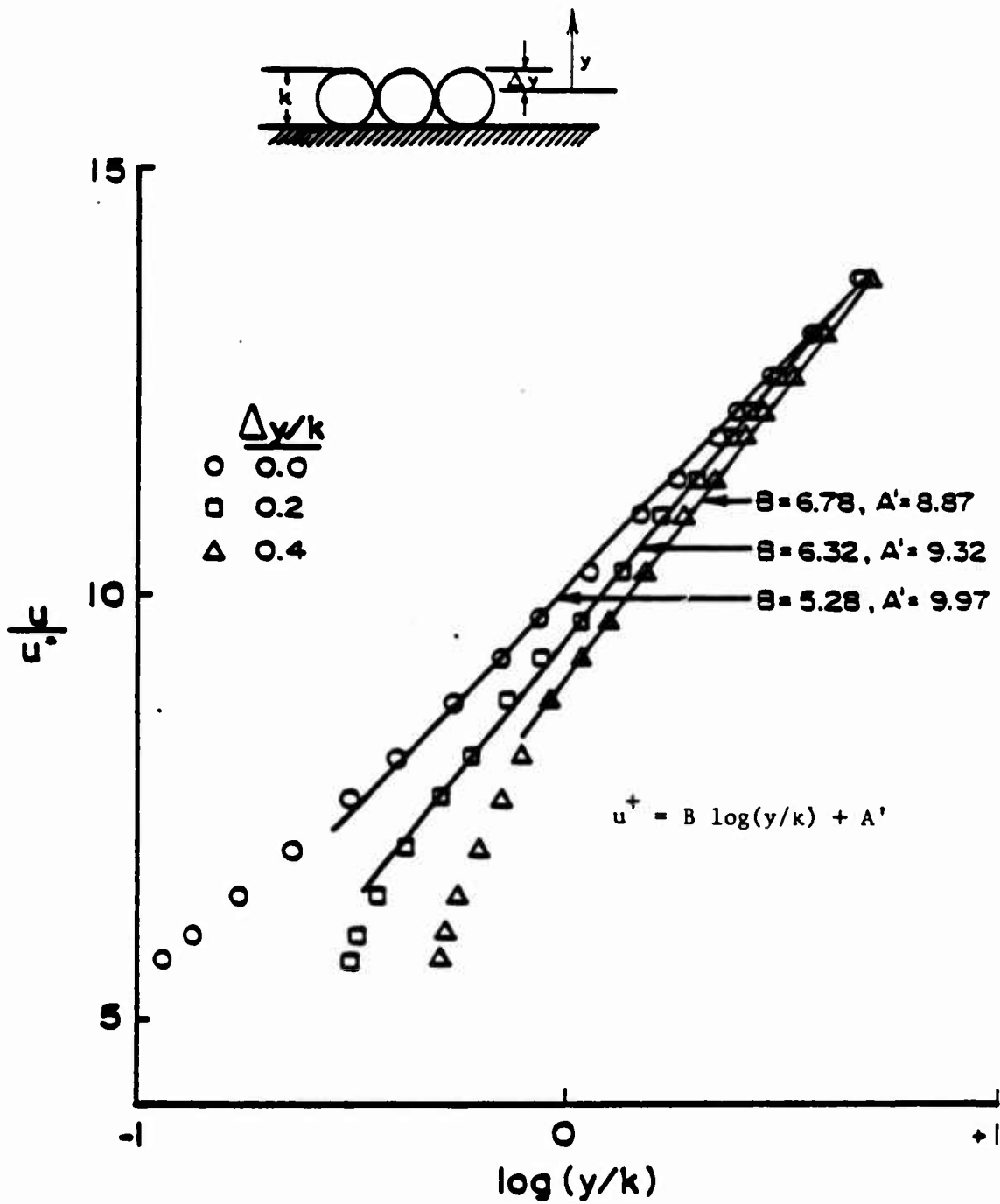


Figure 2. Typical Velocity Profiles for a Fully Rough Turbulent Boundary Layer in Zero Pressure Gradient [5]

not always suggest that the proper origin has been selected. A further complication is the fact that Nikuradse did not state the origin for y in his report [1]. Use of equation (4) requires that the origins for y in equations (2) and (3) be the same.

Determination of the correct origin for y is one of the more difficult tasks in this type of analysis. Perry and Joubert [8] have proposed a graphical method for determining this origin. Also, Monin and Yaglom [9] have proposed a method based on the mathematical nature of the logarithm function. It is generally believed that this origin should lie somewhere between the valleys and crests of the elements. However, Perry, et al [10] have found effective wall locations 1.5 to 2.0 element heights below the crest for transverse bar roughness.

If the equivalent sand-grain roughness approach is to be a useful predictive tool, some method must exist to specify k_s for surfaces for which no skin friction data exist. Dvorak [11], Simpson [12], and Dirling [13] have presented correlations for k_s/k (or the shift in the mean velocity profile, Δu^1) with some parameters that attempt to account for the dependence on roughness height, spacing, and shape. The correlation of Dirling [13] is representative of these efforts and is shown in Figure 3. Dirling plotted k_s/k versus a roughness density $\lambda = (\ell_r/k) (A_s/A_p)^{1.25}$ where k is the mean roughness height, ℓ_r is the average center to center spacing, A_s is the windward surface area of the element, and A_p is the projected windward surface area of the element.

Dirling's correlation seems to collapse the available data better than the others. However, several points warrant discussion. Inspection of Figure 3 reveals that the data for k_s/k spread significantly for a given value of λ . For $\lambda \approx 25$ it is seen that the data vary from $k_s/k \approx 0.2$ to $k_s/k \approx 0.6$ and for $\lambda \approx 11$ from $k_s/k \approx 0.8$ to $k_s/k \approx 2.4$, while the correlation gives, respectively, $k_s/k \approx 0.3$ and $k_s/k \approx 1.2$. Therefore, the reliability of this better correlation is approximately

¹The law of the wall for rough surfaces is often expressed alternatively as

$$\frac{u}{u^*} = 5.75 \log \frac{yu^*}{\nu} + 5.5 - \Delta u \left(\frac{k u^*}{\nu} \right)$$

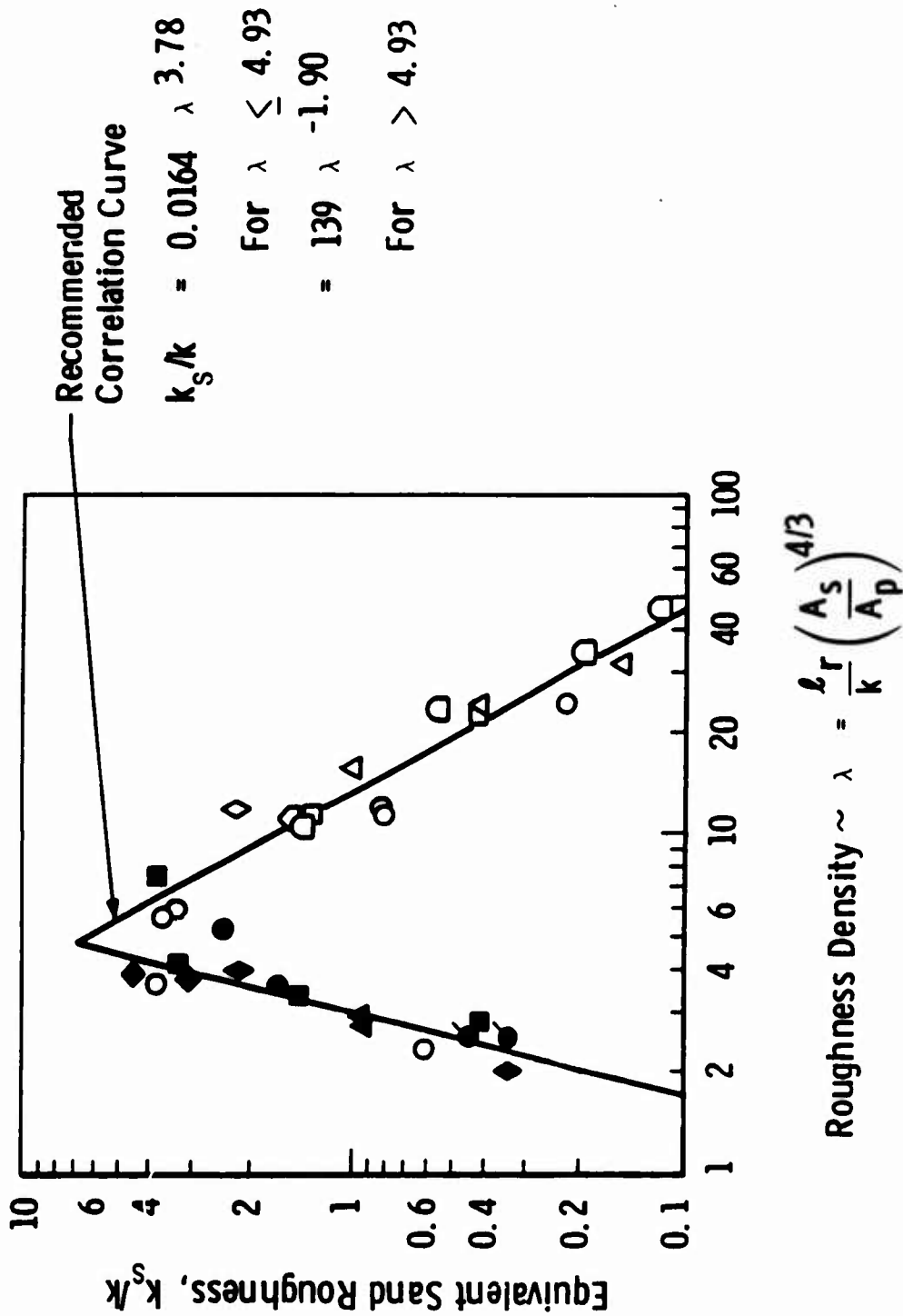


Figure 3. Effective Sand-Grain Roughness Correlation of Dirling [13]

$\pm 100\%$. Berg [14] found that the correlation gave a value of k_s/k three times larger than his experimentally determined values. Secondly, they do not distinguish between two-dimensional and three-dimensional roughness. The nature of the flow around these two different types of roughness is very different. The flow over two-dimensional elements is more strongly dependent on the spacing (distance between strips) than the height while for three-dimensional elements both height and spacing seem to be about equally important. For example, Perry, et al [10] found that for certain ranges of k/ℓ_r the skin friction coefficient, C_f , does not scale with the roughness height, k , for transverse bar roughness. Also, for general roughness (i.e., randomly sized and distributed elements) there is no set correct method for characterizing the roughness (i.e., specifying k , ℓ_r , A_s and A_p). King, et al [15] have discussed this problem without giving a resolution.

All of the above correlations rely heavily on Schlichting's [3] original determinations of k_s/k . As discussed in the following sections and in Appendix A, Schlichting's data reduction method was flawed (mainly by neglecting the effects of the side walls of his 4:1 aspect ratio channel). As shown in Appendix A, corrected or modified values of k_s/k differ from those originally reported by 26% to 55%.

The equivalent sand-grain roughness, k_s , is used in predictive modeling through algebraic correlations, integral methods, and differential (finite difference) methods. Many correlations for skin friction coefficient, C_f , and Stanton number, St , have been presented. Examples are Schlichting [3], Dipprey and Sabersky [16], Nestler [17], and Seidman [18]. Dvorak [11] has presented an integral method to predict skin friction and heat transfer.

In the present state of boundary layer computation, the differential methods are by far the most important. These methods solve the partial differential equations of the boundary layer with finite difference techniques. Cebeci and Chang [19] present a method that relies heavily on the equivalent sand-grain roughness. They solve the usual incompressible boundary layer continuity and momentum equations for the flow field. They account for the roughness via a virtual origin Δy for the Prandtl mixing length, where Δy is defined as a function of k_s . One of the major problems with differential methods that use the equivalent

sand-grain roughness is the ill-defined wall boundary condition. Cebeci and Chang [19] attempt to overcome this by defining wall conditions at some distance y_0 above the crest of the roughness. They determine the velocity boundary conditions (u_0, v_0) at this point from empirical velocity profile correlations.

Lin and Bywater [20] and Adams and Hodge [21] present differential methods that are basically discrete element approaches (discussed below) but which, however, rely on equivalent sand-grain roughness to some degree in their turbulence models.

The reader has probably noticed that the above discussion of equivalent sand-grain roughness is almost totally concerned with momentum transport. In fact, the equivalent sand-grain roughness, k_s , is defined only on the basis of skin friction and velocity profile data. In general, attempts to use equivalent sand-grain roughness to correlate heat transfer data have not been successful. This is most likely because the mechanisms for momentum and energy transport to a roughness element are different. The apparent shear stress at the wall (total tangential force on the wall divided by wall area) is composed of viscous forces plus form drag on the elements. For heat transfer there is no transport mechanism which is analogous to the form drag on the element. In fact, there is no physical reason for two surfaces with the same skin friction coefficient to have the same Stanton number.

In summary, the outstanding problems with the equivalent sand-grain approach are as follows:

1. To accurately predict skin friction, experimental data for the particular rough surface or a similar surface are usually required.
2. In general, sand-like surfaces do not have a value of $k_s/k = 1$.
3. The effective wall location is not readily apparent.
4. Many roughness geometries do not correlate with a single length scale. The present correlations between k_s/k and some density parameter are, in general, unreliable.
5. Attempts to interface equivalent sand-grain models with finite difference boundary layer computations results in an ill-defined boundary condition at the wall.

6. There is no physical reason for heat transfer data to correlate with k_s .

In spite of appearances, it is not our intention here to say that the equivalent sand-grain approach is a complete failure. Its dominance of the subject of flow over rough surfaces for the past half century is testimony to its value in filling some of the gaps in the science of fluid mechanics. However, many gaps remain. In recent years the alternate approach has gained momentum.

2. THE DISCRETE ELEMENT APPROACH

In the same paper [3] in which Schlichting proposed the equivalent sand-grain roughness approach, he proposed (as a means of better understanding the dependence of flow resistance on the roughness density) that the flow resistance of the rough surface be divided into two components: (1) that due to the form drag on the element and (2) that due to the viscous shear on the smooth surface area between the roughness elements. Schlichting defined W as the total resistance, W_r as that part of W due to the drag on the elements, and W_s as that part due to the viscous shear on the smooth parts of the surface, where $W_r = W - W_s$. Then he defined an element resistance coefficient $C_d = 2W_r / (\rho u_k^2 F_r)$, where u_k is the velocity at the crest of the elements and F_r is the projected frontal area of the roughness element. Schlichting went on to calculate C_d for all of his surfaces; however, this information was not put to any practical use at that time. Following these same ideas, a body of literature has arisen that here is referred to as the discrete element approach.

The discrete element approach considers the momentum and energy transport processes on the collection of individual roughness elements and the smooth surface between the elements. The basic idea of the discrete element approach is to formulate a system of partial differential equations that describe the mass, momentum, and energy transport for the flow over, around, and between the roughness elements. In this method the roughness effects are taken as an integral part of the flow problem and not (as with the equivalent sand approach) as some ill-defined boundary condition.

Figure 4 shows the major physical phenomena that distinguish flow over a rough surface. They are blockage of the flow, form drag on the

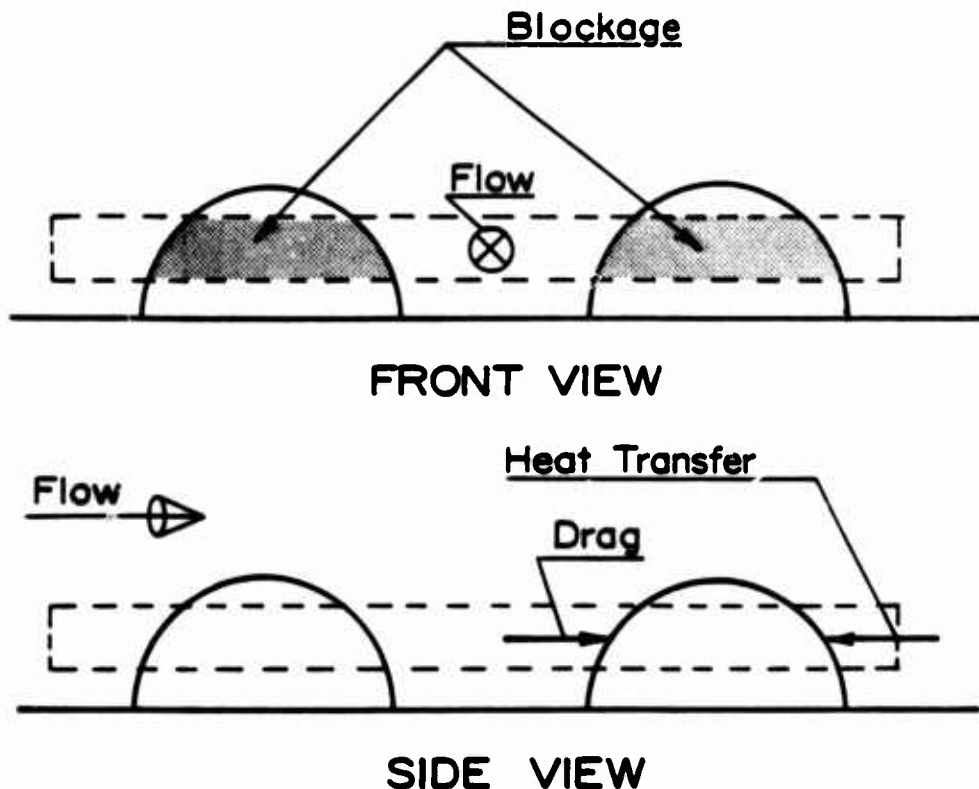


Figure 4. Schematic of a Rough Surface

roughness elements, and local heat transfer between the elements and the fluid. The roughness elements occupy a finite fraction of the space available to fluid flow and thus block the flow. As the fluid flows over and around an element, zones of different pressure develop resulting in form or pressure drag on the elements. Therefore, because of these forces, momentum is extracted volumetrically from the flow. If the fluid and the element are at different temperatures, there will be local heat transfer between the element and the fluid. Therefore, the elements act also as volumetric heat sources or sinks (depending, of course, on the relationship between the fluid and element temperatures).

The above mentioned partial differential equations are formulated in such a way that they account for the roughness geometry and the roughness phenomena (blockage, distributed momentum sink, and distributed

heat sink/source). These equations are then solved (usually by finite difference methods) with the appropriate boundary conditions. The wall boundary conditions are now well defined. The velocities must go to zero at the base smooth wall and the temperature of the fluid at the wall must be equal to the base smooth wall temperature.

The other common wall boundary condition for the energy equation is the adiabatic wall. Care must be taken when specifying an adiabatic rough wall. Merely requiring that the derivative of the temperature be zero at the base wall is not adequate, since the elements would remain as a major route for energy transport.

The discrete element approach fills many of the gaps left by the equivalent sand-grain approach. A brief list is provided below:

1. The roughness geometry is accounted for in the formulation of the equations. All measures are included, namely height, shape, and density or distribution. A single length scale is not relied upon. Also, no nebulous standard roughness is required.
2. The problem of the effective wall location and the ill-defined boundary conditions are not encountered. The discrete element partial differential equations are integrated out from the base smooth wall while the roughness effects are included in the equations.
3. The effect of roughness on energy transport is included in the equations in a physically meaningful manner.

As stated above, many of the basic ideas of the discrete element method were first proposed by Schlichting [3] in 1936. Later, Liepmann and Goddard [22] took this view as did Lewis [23]. In recent years several serious attempts to use the discrete element model as a basis for calculation methods have been presented. Calculation methods for skin friction and/or heat transfer on rough surfaces using the discrete element approach have been reported by Adams and Hodge [21], Lin and Bywater [20], Finson and co-workers [24,25,26], Christoph and co-workers [27,28], and Roberson and co-workers [29,30,31].

The model of Adams and Hodge [21] includes only one aspect of the discrete element approach, namely the form drag of the roughness elements.

They do not address the problem of flow blockage caused by the elements. Also, they do not model the heat transfer between the elements and the fluid. However, they do calculate heat fluxes and by consequence Stanton numbers with apparent success for some cases. In addition, they only use the discrete element approach to calculate the flow field over fully rough surfaces. They calculate the flow field over transitionally rough surfaces by using an equivalent sand-grain approach from Healzer [32].

Lin and Bywater [20] address all three roughness phenomena (blockage, distributed momentum sink, and distributed heat sink/source). However, they do not distinguish between flow blockage in planes that are parallel and those that are perpendicular to the flow direction. In addition, they use turbulence models which are based on the equivalent sand-grain method.

Finson and his co-workers [24,25,26] have presented a discrete element calculation method that does not rely on any sand-grain concepts. The earlier work, Finson and Wu [24], does not include the blockage phenomenon. Their later works, Finson and Clark [25] and Finson [26], include both blockage factors and a distributed momentum sink term. However, they do not account for the distributed heat source/sink term. Their flow blockage factors are applied inconsistently in the equations. Also, their definition for blockage in planes that are perpendicular to the flow direction is incorrect. (This will be discussed in Section III.) In addition, they do not state exactly how values for skin friction coefficient and Stanton number are calculated.

The work of Christoph and his co-workers [27,28] follows the work of Finson very closely. They present two methods--an integral method, Christoph [27], and a finite difference method, Christoph and Pletcher [28]. In both papers they use a mixing-length model for the turbulent shear stress that has been modified to include roughness factors. In the integral method a Stanton number is calculated from the integrated boundary layer equation. Also, in the finite difference method they calculate the enthalpy field over the surface. However, in both papers the Stanton number that is compared with the experimental data is calculated from a correlation with the skin friction coefficient. They

set the heat transfer augmentation due to roughness equal to the square root of the skin friction augmentation due to roughness.

Roberson and his co-workers [29,30,31] have worked continuously for more than twenty years with a model for fully developed flow in rough conduits that is closely related to the discrete element approach. Their model divides the skin friction into viscous and element drag components and calculates a velocity profile below the crest of the roughness elements based on an assumed shear stress distribution. However, their model differs from the discrete element model as defined here in that they do not formulate a differential equation that describes the entire flow field. Therefore, their insightful model is not easily extended to developing flows where boundary layer or Navier-Stokes based calculations are required.

The discrete element models discussed above, while they are usually insightful, seem to varying degrees to be patchwork affairs. Terms are added to the equations and multipliers supplied in an ad hoc manner to satisfy physical reasoning. No attempt appears to have been made to systematically derive the equations from first principles. In the present work a discrete element model is derived for two-dimensional boundary layer flow from first principles. This model accounts for all three of the major roughness phenomena (blockage, form drag, and distributed heat sink/source). The model is calibrated using baseline experimental data and is compared to a wide range of additional experimental data.

SECTION III

DERIVATION OF THE DISCRETE ELEMENT MODEL

In the discrete element approach the rough surface is assumed to be composed of discrete or distinct roughness elements. Such a surface could be one composed of some uniform array of cones, spheres, hemispheres, etc. that are glued or welded to a smooth base surface. A uniform array of elements with circular cross sections is used in this section for all derivations because it is easily visualized. However, the discrete element model that is derived is also applicable to non-uniform arrays so long as some adequate system exists to define the various parameters used to quantify the roughness geometry. For non-uniform, but descriptive, arrays the geometry is easily quantified. For example, consider an array composed of rows of cones where the distance between cones in each row and the distance between rows is halved with each additional row until the most dense packing is obtained. For general roughness (i.e., where the elements are random in size, shape, and spacing), accounting for each individual element is no longer practical and some averaging or statistical process must be used. This is not a severe limitation on the model. Considerable spatial averaging is already necessarily introduced by means of the finite difference process. In a later section that discusses the quantification of the roughness geometry, a system is presented for general roughness.

In this work only three-dimensional or distributed (k-type) roughness is considered. Graphic examples are the above mentioned arrays of cones, spheres, etc. In addition, most naturally occurring rough surfaces are of this type. A rusty pipe, a corroded turbine blade, an ablated heatshield, barnacles on a ship's hull, a dull spray painted surface, and forests are examples of distributed roughness geometries. Two-dimensional or strip (d-type) roughness is not considered. This important type of roughness is generally man-made. Examples are threads in a pipe, fiber-resin composites, and rows of corn. The flow over and among strip-type elements is physically quite different from that over distributed roughness elements and requires a separate treatise.

In this section the two-dimensional time-averaged boundary layer equations for turbulent flow over a rough surface are derived. To obtain the desired equations, a differential control volume is imagined which contains the pertinent roughness effects determined from averaging over several typical elements. Mass, momentum, and energy balances are made for this control volume to derive a system of partial differential equations that describe the flow over a rough surface.

As discussed in Section I, empirical information must be provided on the nature of the turbulence and the roughness if practical solution techniques are to be used. The turbulence model and the roughness model are described, and the calibration of the roughness model is discussed in detail in Section V.

1. DERIVATION OF THE BOUNDARY LAYER EQUATIONS

To derive the boundary layer equations for the conservation of mass, momentum, and energy, a differential control volume is imagined as shown in Figure 5. The control volume is shown with an exaggerated length in the x-direction for easier visualization of the roughness effects. Using this control volume, the appropriate balances are made to derive the partial differential equations that describe the boundary-layer flow of a fluid over a rough surface.

Figure 6 shows the control volume with the rate of mass flow terms. Performing a steady-state mass balance

$$0 = - \left\{ \rho u A_x + \frac{\partial \rho u A_x}{\partial x} \delta x - \rho u A_x \right\} - \left\{ \rho v A_y + \frac{\partial \rho v A_y}{\partial y} \delta y - \rho v A_y \right\} \quad (6)$$

Before proceeding, expressions for the area open for fluid flow in the x-direction, A_x , and for the area open for fluid flow in the y-direction, A_y , must be developed. Inspection of the control volume reveals that, on the average, not all of either surface is open for fluid flow; some fraction of the surface is blocked by the roughness elements. This phenomenon is most conveniently expressed in terms of blockage factors. Let α_x (α_y) be the fraction of the surface that is perpendicular to the x-coordinate (y-coordinate) that is closed or blocked to flow. These α 's are hereafter referred to as the blockage factors. Now A_x and A_y

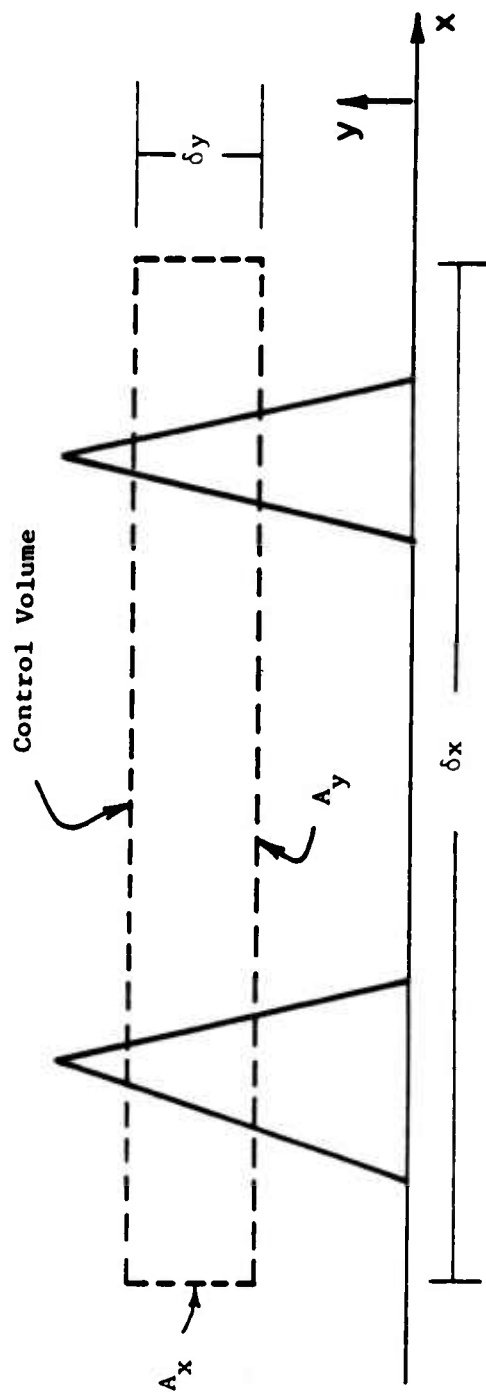
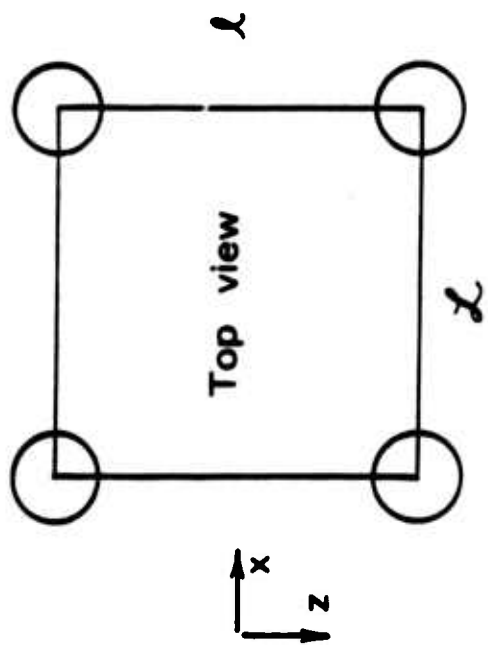


Figure 5. General Layout of Control Volume

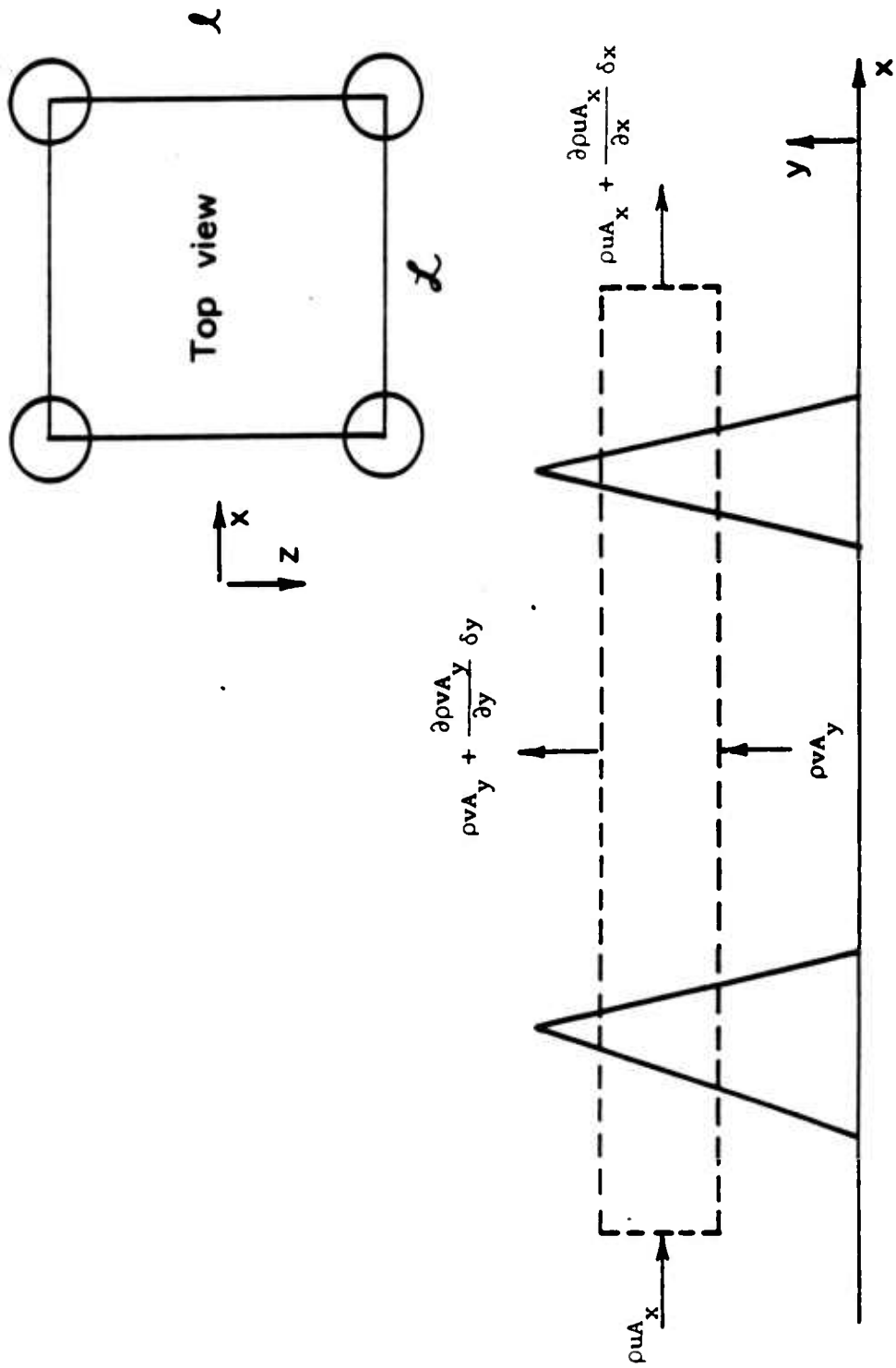


Figure 6. Mass Balance Control Volume

can be expressed as

$$A_x = (1 - \alpha_x) \delta y \cdot 1 \quad (7a)$$

$$A_y = (1 - \alpha_y) \delta x \cdot 1 \quad (7b)$$

where unit depth in the z-direction is assumed.

Substituting equations (7) into equation (6) and simplified yields the desired continuity equation

$$0 = \frac{\partial}{\partial x} [\rho(1 - \alpha_x)u] + \frac{\partial}{\partial y} [\rho(1 - \alpha_y)v] \quad (8)$$

Figure 7 shows the control volume with the rate of momentum flow terms. Performing a steady-state momentum balance

$$\begin{aligned} 0 = & - \left\{ \tau_{A_y} + \frac{\partial \tau_{A_y}}{\partial y} \delta y - \tau_{A_y} \right\} \\ & - \left\{ \rho u u A_x + \frac{\partial \rho u u A_x}{\partial x} \delta x - \rho u u A_x \right\} \\ & - \left\{ \rho v v A_y + \frac{\partial \rho v v A_y}{\partial y} \delta y - \rho v v A_y \right\} \\ & - \left\{ p A_x + \frac{\partial p A_x}{\partial x} \delta x - p A_x \right\} - F_D \end{aligned} \quad (9)$$

Again the blockage is contained in the terms A_x and A_y as above. The most important difference between this balance and one for flow over a smooth surface is the additional term F_D . Physically F_D is the force exerted by the roughness elements on the fluid in the control volume. This force is a result of the shear and pressure distribution around the roughness elements and, vectorally, it is the negative of the drag force on the elements. Also, it is convenient to think of F_D as a distributed momentum sink. That is, below the crest of the elements momentum is extracted volumetrically from the flow.

The term F_D is most conveniently cast in terms of a nondimensional drag coefficient, C_D .

$$F_D = \frac{1}{2} \rho C_D u^2 (\delta A_p) \quad (10)$$

where (δA_p) is the projected frontal area of the elements in the control volume. For elements of circular cross section

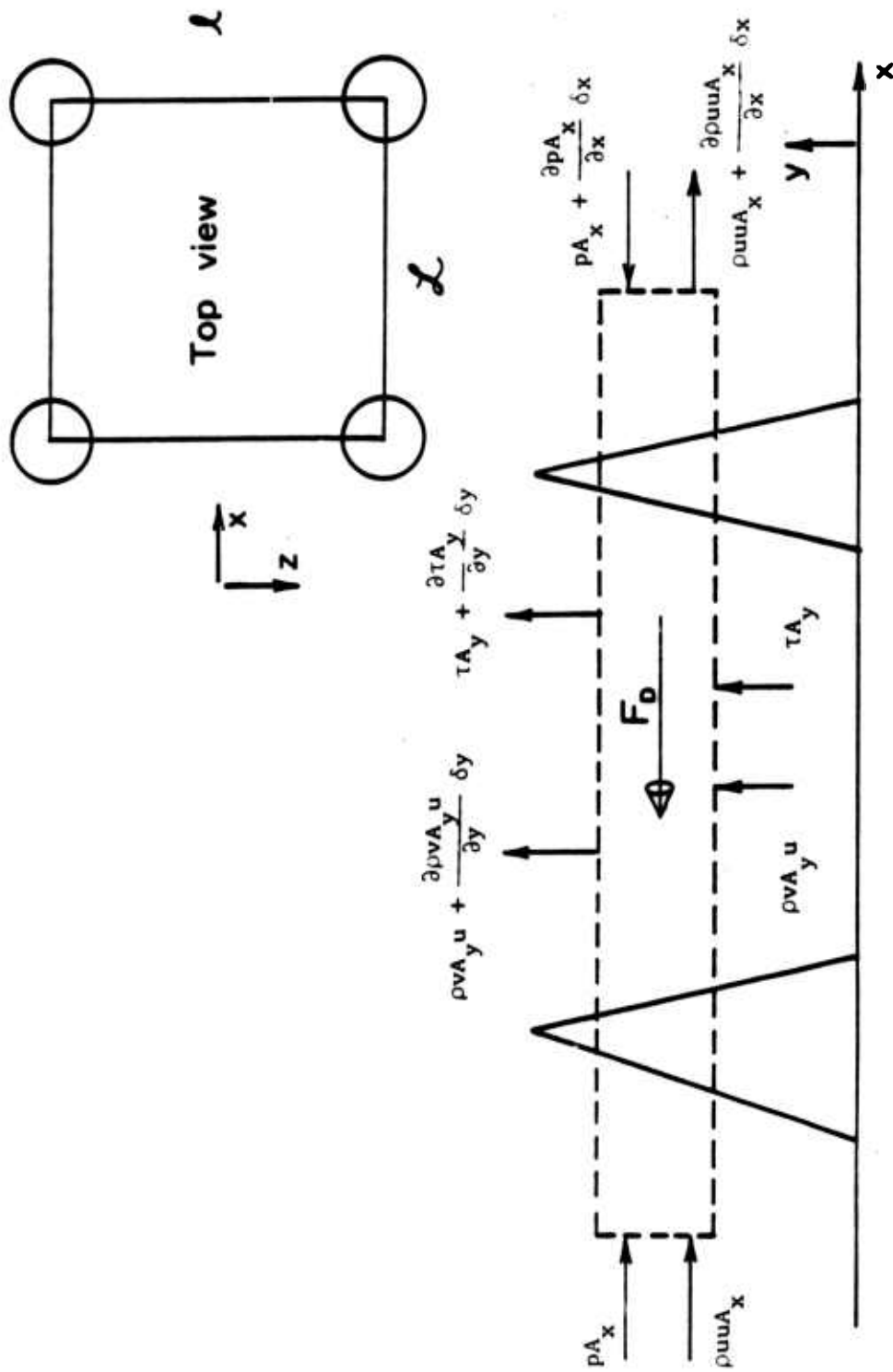


Figure 7. Momentum Balance Control Volume

$$\delta A_p = d(y)\delta y \left(\frac{\delta x \cdot 1}{L\ell} \right) \quad (11)$$

where $(\delta x \cdot 1/(L\ell))$ is the number of elements in the control volume and $d(y)$ is the local cross sectional diameter.

Substituting equations (7), (10), and (11) into equation (9) and simplifying gives the x-momentum equation

$$\begin{aligned} 0 = & \frac{\partial}{\partial y} [(1 - \alpha_y)\tau] + \frac{\partial}{\partial x} [\rho(1 - \alpha_x)uu] \\ & + \frac{\partial}{\partial y} [\rho(1 - \alpha_y)uv] + \frac{\partial}{\partial x} [(1 - \alpha_x)p] \\ & + \frac{1}{2} \rho C_D u^2 \frac{d(y)}{L\ell} \end{aligned} \quad (12a)$$

Equation (12a) can be simplified by expanding the convective terms and recalling equation (8) to give the more usual form

$$\begin{aligned} & \rho(1 - \alpha_x)u \frac{\partial u}{\partial x} + \rho(1 - \alpha_y)v \frac{\partial u}{\partial y} \\ & = - \frac{\partial}{\partial x} [(1 - \alpha_x)p] - \frac{\partial}{\partial y} [(1 - \alpha_y)\tau] \\ & \quad - \frac{1}{2} \rho C_D u^2 \frac{d(y)}{L\ell} \end{aligned} \quad (12b)$$

Figure 8 shows the control volume with the rate of energy flow terms. Performing a steady-state energy balance with the normal boundary layer assumptions, i.e., for shear work on the x-surface $\partial w_{s,x}/\partial x \approx 0$ and for energy conducted through the x-surface $\partial E_{cd,x}/\partial x \approx 0$

$$\begin{aligned} 0 = & \left\{ E_{cv,x} + \frac{\partial E_{cv,x}}{\partial x} \delta x - E_{cv,x} \right\} \\ & + \left\{ E_{cv,y} + \frac{\partial E_{cv,y}}{\partial y} \delta y - E_{cv,y} \right\} \\ & + \left\{ E_{cd,y} + \frac{\partial E_{cd,y}}{\partial y} \delta y - E_{cd,y} \right\} \\ & + \left\{ W_{s,y} + \frac{\partial W_{s,y}}{\partial y} \delta y - W_{s,y} \right\} \\ & - W_{drag} - Q \end{aligned} \quad (13)$$

where

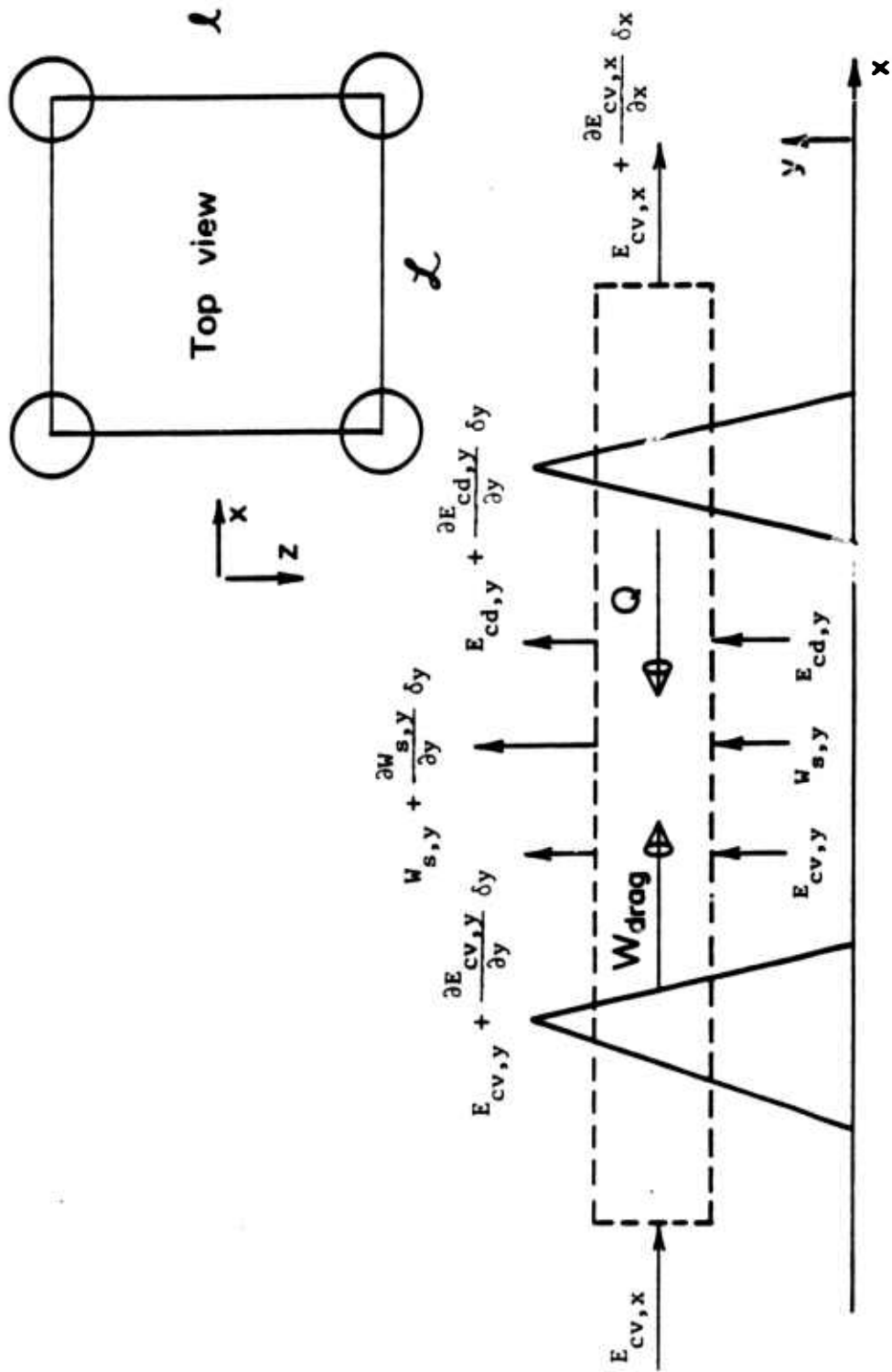


Figure 8. Energy Balance Control Volume

$$\begin{aligned}
E_{cv,x} &= \text{rate of energy convected across x-surface} = \\
&\quad \rho u A_x \left(h + \frac{u^2}{2} \right) \\
E_{cv,y} &= \text{rate of energy convected across y-surface} = \\
&\quad \rho v A_y \left(h + \frac{u^2}{2} \right) \\
E_{cd,y} &= \text{rate of energy conducted across y-surface} = q_y A_y \\
W_{s,y} &= \text{rate of shear work on y-surface} = \tau A_y u \\
W_{\text{drag}} &= \text{rate of work due to drag force} = 0 \\
Q &= \text{local heat transfer rate between element and fluid} = \\
&\quad \frac{K}{d} Nu_d A_e (t_R - t)
\end{aligned}$$

The two additional terms (over the smooth case) merit some discussion. The work caused by the drag forces on the elements is zero since the velocity goes to zero at the surface of an element. The term Q is a distributed heat sink (source) term that accounts for the volumetric depletion (addition) of energy from (to) the flow because of the presence of a cold (hot) roughness element. Here Q is expressed in terms of the local Nusselt number, Nu_d , and the roughness element temperature, t_R . The term A_e is the area of the roughness elements in contact with the fluid in the control volume. For elements of circular cross section

$$A_e = \pi d(y) \delta y \left(\frac{\delta x \cdot 1}{Ll} \right) \quad (14)$$

Substituting the above along with the expressions for A_x and A_y (equations (7a) and (7b)) into the energy balance yields the energy equation

$$\begin{aligned}
\frac{\partial}{\partial x} \left[\rho u (1 - \alpha_x) \left(h + \frac{u^2}{2} \right) \right] + \frac{\partial}{\partial y} \left[\rho v (1 - \alpha_y) \left(h + \frac{u^2}{2} \right) \right] \\
= - \frac{\partial}{\partial y} [(1 - \alpha_y) q_y] - \frac{\partial}{\partial y} [(1 - \alpha_y) \tau u] \\
+ \pi \frac{K Nu_d}{Ll} (t_R - t)
\end{aligned} \quad (15a)$$

Equation (15a) can be expressed in the more familiar form of static enthalpies, h , by combination with the equations for continuity (8) momentum (12)

$$\begin{aligned}
\rho(1 - \alpha_x)u \frac{\partial h}{\partial x} + \rho(1 - \alpha_y)v \frac{\partial h}{\partial y} &= - \frac{\partial}{\partial y} [(1 - \alpha_y)q_y] \\
- (1 - \alpha_y)\tau \frac{\partial u}{\partial y} + u \frac{\partial}{\partial x} [(1 - \alpha_x)p] & \\
+ \frac{1}{2} \rho C_D u^3 \frac{d(y)}{Ll} + \frac{\pi K N u_d}{Ll} (\tau_R - t) & \quad (15b)
\end{aligned}$$

The equations derived so far (continuity, (8); x-momentum, (12); and energy, (15)) model steady laminar boundary layer flow over rough surfaces. Before we can practically apply these equations to turbulent boundary layers we will have to use the Reynolds averaging process to obtain the equations for time mean turbulent flow. First the velocities, enthalpies, etc. are expressed as a mean term plus a fluctuating term

$$u = U + u' \quad (16a)$$

$$v = V + v' \quad (16b)$$

$$h = H + h' \quad (16c)$$

$$p = P + p' \quad (16d)$$

$$t = T + t' \quad (16e)$$

Secondly the shear stress, τ , and heat flux, q_y , are expressed by the usual phenomenological rate equations

$$\tau = - \mu \frac{\partial u}{\partial y} \quad (17)$$

$$q_y = - K \frac{\partial T}{\partial y} = - \frac{K}{C_p} \frac{\partial h}{\partial y} \quad (18)$$

Substituting equations (16), (17), and (18) into the conservation equations (8), (12), and (15) and taking the time average we obtain

Continuity:

$$\frac{\partial}{\partial x} [\rho(1 - \alpha_x)U] + \frac{\partial}{\partial y} [\rho(1 - \alpha_y)V] = 0 \quad (19)$$

x-Momentum:

$$(1 - \alpha_x)\rho U \frac{\partial U}{\partial x} + (1 - \alpha_y)\rho V \frac{\partial U}{\partial y}$$

$$\begin{aligned}
&= -\frac{\partial}{\partial x} [(1 - \alpha_x)P] + \frac{\partial}{\partial y} \left[(1 - \alpha_y) \left(\mu \frac{\partial U}{\partial y} - \rho \overline{u'v'} \right) \right] \\
&\quad - \frac{1}{2} \rho C_D d(y) \frac{U^2}{L\ell} \left(1 + \frac{\overline{u'^2}}{U^2} \right)
\end{aligned} \tag{20}$$

Energy:

$$\begin{aligned}
&(1 - \alpha_x)\rho U \frac{\partial H}{\partial x} + (1 - \alpha_y)\rho V \frac{\partial H}{\partial y} \\
&= \frac{\partial}{\partial y} \left[(1 - \alpha_y) \left(\frac{K}{C_p} \frac{\partial H}{\partial y} - \rho \overline{v'h'} \right) \right] \\
&\quad + U \frac{\partial}{\partial x} [(1 - \alpha_x)P] + (1 - \alpha_y)\overline{\Phi} \\
&\quad + \frac{1}{2} \rho C_D \frac{d(y)}{L\ell} U^3 \left(1 + 3 \frac{\overline{u'^2}}{U^2} \right) \\
&\quad + \pi \frac{KNu_d}{L\ell} (T_R - T)
\end{aligned} \tag{21}$$

where as usual the terms $\partial(\overline{u'^2})/\partial x$ and $\partial(\overline{u'h'})/\partial x$ are neglected. For a boundary layer the mean dissipation term, $\overline{\Phi}$, is approximated by

$$\overline{\Phi} \approx \frac{\partial U}{\partial y} \left(\mu \frac{\partial U}{\partial y} - \rho \overline{u'v'} \right)$$

Inspection of equations (20) and (21) reveals an interesting dependence on the turbulent intensity, $\overline{u'^2}/U^2$, in the terms containing the drag coefficient, C_D . In general, the turbulent intensity is not negligible. However, this dependence is secondary and can be (to a good approximation) incorporated into the model for the drag coefficient, thus avoiding a need for another empirical closure for $\overline{u'^2}/U^2$.

In the above we have derived partial differential equations that describe two-dimensional turbulent boundary-layer flow over a rough surface. At this point some remarks are in order. The equations were derived assuming distributed or three-dimensional elements. By the very nature of this type of surface the flow will be three-dimensional. However, in this model z-direction variations are not considered. In other words, all z-direction variations are averaged out. This averaging out is not a severe limitation as long as the control volume in which the various balances were made contains the appropriate amount of roughness effects determined by averaging over several roughness elements. The

generally good agreement with experimental data shown in later sections reinforces this idea.

The fact that the control volume contains roughness effects determined by averaging over several roughness elements is also important in the flow direction. This averaging dimension, in general, must span several elements if the present model is to make sense. This averaging of the flow parameters over some small but finite x-step, Δx , is only of small consequence, since the most (and probably only) practical way to solve the partial differential equations is in finite difference form.

Before the above equations can be used to predict flow over a rough surface some system must be developed to quantify the roughness geometry.

2. QUANTIFICATION OF THE ROUGHNESS GEOMETRY

Inspection of equations (19), (20), and (21) reveals that the roughness geometry is described by the parameters α_x , α_y , and $d(y)$. The parameters C_D and Nu_d contain empirical information about the drag and heat transfer of the elements but are considered here (as discussed in a later section) to be functions of $d(y)$, or more precisely, the local Reynolds number, $Re_d = U(y)d(y)/\nu$. First, we will consider the case of a uniform array and then we will consider a system for general roughness. Here all roughness elements are assumed to have cross-sections that are approximately circular.

a. Uniform Arrays

For uniform arrays the cross-sectional diameter, $d(y)$, is the same for all of the elements at a given y-location. Determination of $d(y)$ is simply a matter of considering the geometry of a single element. Figure 9 shows functional relationships for several common roughness shapes. Referring to Figure 5 we see by inspection that α_y is

$$\alpha_y = \frac{\pi d^2}{4L\ell} \quad (22)$$

At first glance α_x appears to be $\alpha_x = d/\ell$. In fact, this is the conclusion of most other workers [26,28]. However, this is the maximum blockage. At most x-locations the blockage is less, and at some locations the blockage may be zero. Here the solution is to take an average x-direction blockage. This averaging should be natural in light of the

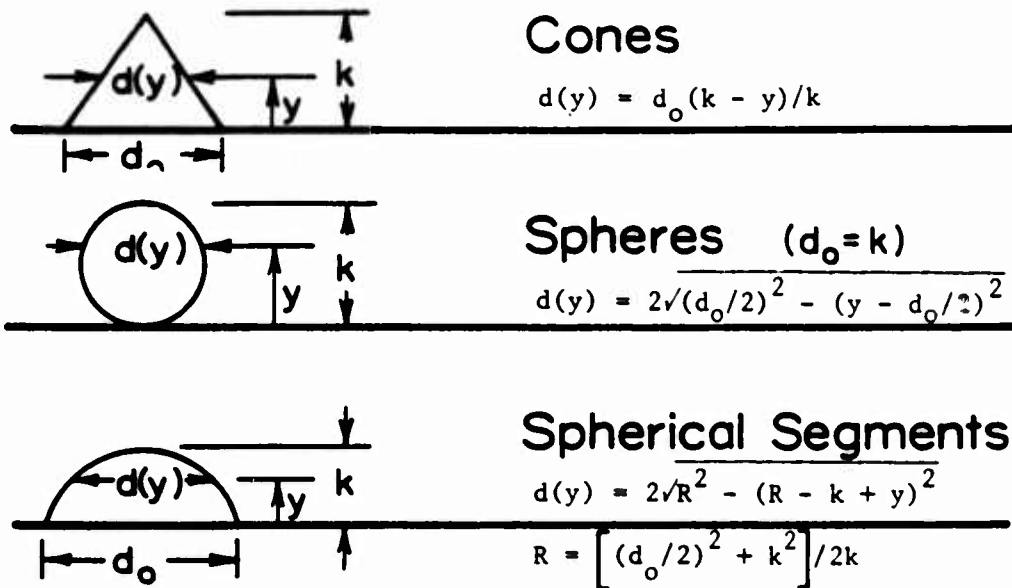


Figure 9. Local Element Diameters for Cones, Spheres and Spherical Segments

averaging already involved in the finite difference nature of the equations discussed above. For a uniform array this averaging removes all x-dependence of α_x , and the averaging length is unimportant as long as this length spans several elements. For a nonuniform array some x-dependence must be preserved. Therefore, some averaging length must be chosen. This length should contain several elements. The natural choice is a length approximately equal to the x-step length, Δx , used in the finite difference form of the equations.

The averaging process for a uniform array of elements of circular cross-section follows. Since α_x always appears as $(1 - \alpha_x)$, the averaging process will be carried out on $(1 - \alpha_x)$. Referring to Figure 10

$$(1 - \alpha_x)_{ave} = \frac{1}{L} \int_0^L (1 - \alpha_x) dx \quad (23)$$

where

$$\alpha_x = 0; \text{ all } X \text{ not encountering an element}$$

$$\alpha_x = \frac{2\sqrt{xd} - x^2}{l}; \text{ all } X \text{ encountering an element}$$

Substituting into equation (23)

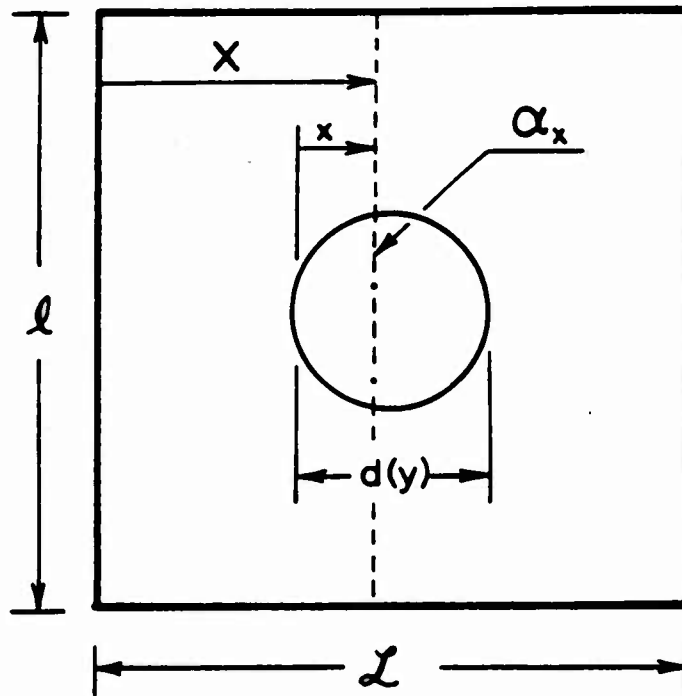


Figure 10. Layout for Averaging α_x

$$(1 - \alpha_x)_{\text{ave}} = \frac{1}{L} \left[(L - d) + \int_0^d \left(1 - \frac{2\sqrt{xd - x^2}}{l} \right) dx \right] \quad (24)$$

Completing the integration

$$(1 - \alpha_x)_{\text{ave}} = \frac{1}{L} \left(L - \frac{\pi d^2}{4l} \right) = 1 - \frac{\pi d^2}{4Ll} \quad (25)$$

It is seen that $(1 - \alpha_x)_{\text{ave}} = (1 - \alpha_y)$ for any uniform array of elements of circular cross-sections. This relationship also holds for any array of circular cross-section so long as l and $d(y)$ are not functions of x over the averaging distance, Δx .

The reader may wonder why so much time is spent discussing the simplest geometry. There are two strong reasons for considering uniform arrays: (1) insights can be developed by considering the simpler case that would be difficult to ascertain from more complicated treatments, and (2) most of the controlled, well-defined experiments for flow over rough surfaces use uniform array surfaces.

b. General Roughness

Before we can quantify the geometry of a general rough surface, we must have some way of collecting data on that roughness. The usual way that roughness is measured is by taking a profilometer trace. Since the general roughness varies in both the x and z directions, at least two traces are required (one in the x and one in the z). Figure 11 shows typical traces and the nomenclature used below. Again we assume that the elements have circular cross-sections.

In order to develop expressions for the blockage factors, we must determine the area blocked by the elements and the associated plane areas. For the xz plane the blockage factor is α_y . Here and in the following developments we will use the z-trace to establish the element diameters, $d(y)$, while the x-trace is used to establish element density. Therefore,

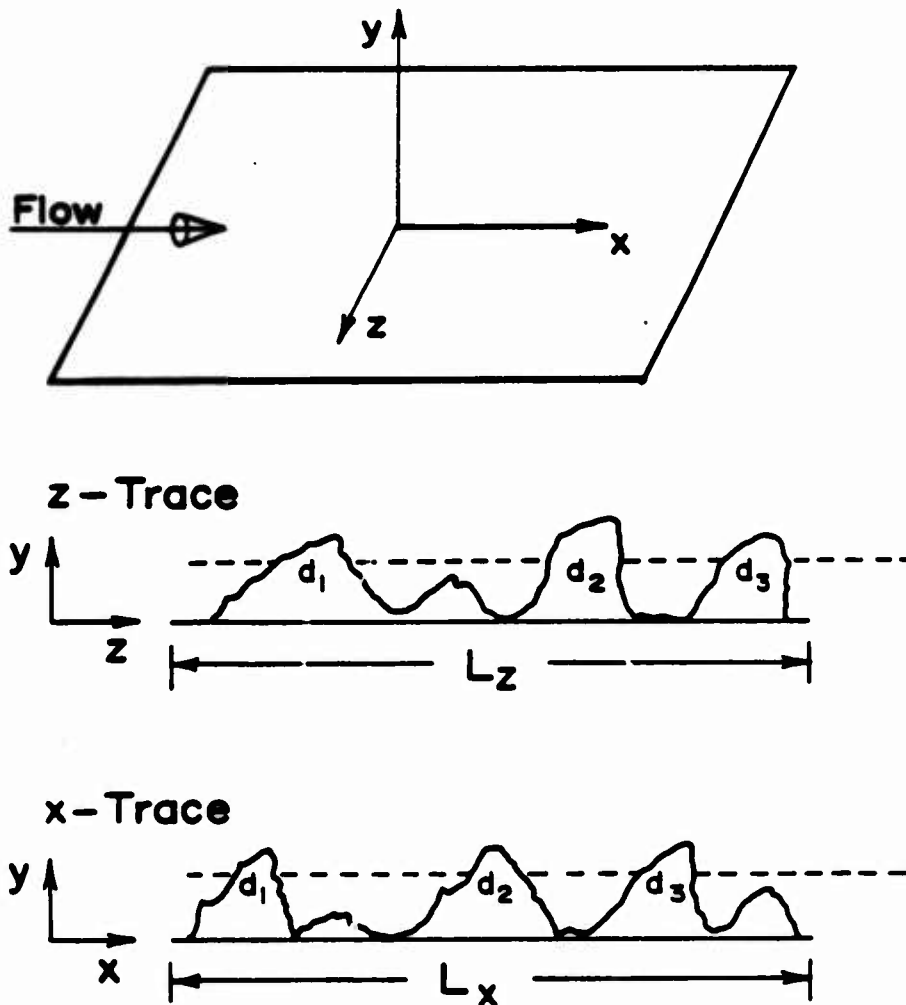


Figure 11. Typical Profilometer Traces

the total xz area occupied by the elements in the neighborhood of the z-trace is

$$A_{\text{tot}} = \frac{\pi}{4} \sum_{i=1}^{N_z(y)} d_i^2(y) \quad (26)$$

where $N_z(y)$ is the number of elements in the z-trace at a y-level. To obtain α_y we need the plane area associated with this z-trace. The z-dimension of this plane area is obviously L_z . The x-dimension for this plane area is the average x spacing of the elements, $L_x/N_x(0)$, where $N_x(0)$ is the number of elements at the level $y = 0$. The xz blockage is then

$$\alpha_y = \frac{\pi N_x(0)}{4L_x L_z} \sum_{i=1}^{N_z(y)} d_i^2(y) \quad (27)$$

For the yz plane the area occupied by an element is $d_{\text{ave}} \delta y$ where d_{ave} is the average diameter over some x dimension, ℓ_x . With a development similar to that which produced equation (25) d_{ave} is

$$d_{\text{ave},i} = \frac{\pi}{4} \frac{d_i^2(y)}{\ell_x} \quad (28)$$

Here $\ell_x = L_x/N_x(0)$ and the associated plane area is $L_z \delta y$ giving the yz blockage

$$\alpha_x = \frac{\pi N_x(0)}{4L_x L_z} \sum_{i=1}^{N_z(y)} d_i^2(y) \quad (29)$$

The form drag term for general roughness is evaluated in a manner similar to that for uniform arrays with L replaced by $L_x/N_x(0)$ and ℓ replaced by L_z to give

$$F_D = \frac{\rho u^2 N_x(0) \sum_{i=1}^{N_z(y)} C_{Di} d_i(y)}{2L_x L_z} \delta x \delta y \cdot 1 \quad (30)$$

Likewise, for the local heat transfer between the element and the fluid is

$$Q = \frac{\pi K N_x(0) (T_R - T) \sum_{i=1}^{N_z(y)} Nu_{di}}{L_x L_z} \delta x \delta y \cdot 1 \quad (31)$$

For the general roughness case, the boundary layer equations become

Continuity:

$$\frac{\partial}{\partial x} [\rho(1 - \alpha_x)U] + \frac{\partial}{\partial y} [\rho(1 - \alpha_y)V] = 0 \quad (19)$$

x-Momentum:

$$\begin{aligned} & (1 - \alpha_x)\rho U \frac{\partial U}{\partial x} + (1 - \alpha_y)\rho V \frac{\partial U}{\partial y} \\ & = \frac{\partial}{\partial x} [(1 - \alpha_x)P] + \frac{\partial}{\partial y} \left[(1 - \alpha_y) \left(\mu \frac{\partial U}{\partial y} - \rho \overline{u'v'} \right) \right] \\ & \quad - \frac{\rho U^2 N_x(0)}{2L_x L_z} \sum_{i=1}^{N_z(y)} C_{Di} d_i(y) \end{aligned} \quad (32)$$

Energy:

$$\begin{aligned} & (1 - \alpha_x)\rho U \frac{\partial H}{\partial x} + (1 - \alpha_y)\rho V \frac{\partial H}{\partial y} \\ & = \frac{\partial}{\partial y} \left[(1 - \alpha_y) \left(\frac{K}{C_p} \frac{\partial H}{\partial y} - \rho \overline{v'h'} \right) \right] \\ & \quad + U \frac{\partial}{\partial x} [(1 - \alpha_x)P] + (1 - \alpha_y)\overline{\Phi} \\ & \quad - \frac{\rho U^3 N_x(0)}{2L_x L_z} \sum_{i=1}^{N_z(y)} C_{Di} d_i(y) \\ & \quad + \frac{\pi K N_x(0) (T_R - T) N_z(y)}{L_x L_z} \sum_{i=1}^{N_z(y)} Nu_{di} \end{aligned} \quad (33)$$

Some remarks are appropriate here. The z trace is used to establish roughness size, shape, and z spacing. The x trace is used to establish the x spacing in the neighborhood of the z trace. If significant x variation of the roughness exists, several z traces and associated x traces would be necessary. Furthermore, equations (32) and (33) reduce to equations (20) and (21) for uniform arrays of identical elements since $L = L_x/N_x(0)$, $l = L_z/N_z(0)$ and $N_z(y) = N_z(0)$ for such arrays.

It should be noted that no effort has been made to correct for the bias in profilometer traces. This bias arises because the trace has a vanishing probability of passing through the peaks of the roughness elements. Thus, the indicated heights and diameters are always on the low side of the true values. No satisfactory analysis of this problem is known to the authors.

3. EMPIRICAL CLOSURE

As discussed previously, empirical information must be provided to model the terms, $\overline{u'v'}$ and $\overline{v'h'}$, that occur in the Reynolds averaged equations for mean turbulent flow. Also, empirical information on the nature of the roughness effects must be provided for a rough surface.

a. Turbulence Model

In this work a simple mixing length model with VanDriest damping is chosen to model the Reynolds stress term, $\overline{u'v'}$. That is,

$$-\overline{u'v'} = \ell_m^2 \left| \frac{\partial U}{\partial y} \right| \frac{\partial U}{\partial y} = \mu_T \frac{\partial U}{\partial y} \frac{1}{\rho} \quad (34)$$

where

$$\ell_m = 0.4y[1 - \exp(-y^+/A^+)] ; \ell_m < 0.09\delta$$

$$\ell_m = 0.09\delta ; \ell_m > 0.09\delta$$

$$A^+ = 26$$

This is exactly the same model that is so often used for smooth surfaces. Many workers [19,21,32] attempt to model rough surfaces by adopting a roughness turbulence model. Usually some correlation for the damping factor, A^+ , as a function of equivalent sand-grain roughness is presented. Often some other augmentation of ℓ_m is adopted, for example, Christoph [27]. The smooth wall turbulence model is adopted here for two reasons: (1) roughness effects are already accounted for in the rough wall boundary layer equations ((19) - (21)) and (2) as shown by Pimenta [4] and Coleman [5] the $\overline{u'v'}$ and $\overline{v't'}$ terms are the same nondimensionally for smooth and rough surfaces.

To model the term $\overline{v'h'}$ a constant turbulent Prandtl number, $Pr_T = 0.9$, is assumed. Then $\overline{v'h'}$ is given by

$$-\overline{v'h'} = \frac{\mu_T}{Pr_T} \frac{\partial H}{\partial y} \frac{1}{\rho} = \frac{K_T}{\rho C_p} \frac{\partial H}{\partial y} \quad (35)$$

b. Roughness Model

The necessary empirical information for rough surfaces is contained in the models for the drag coefficient, C_D , and the Nusselt number, Nu_d . In this work the correlations of Zukauskas [33] for banks of staggered cylinders are used as a starting point, since at a given y -location a slice through an array of elements with circular cross-sections appears similar to a thin slice through a bank of cylinders. Therefore, the behavior of the elements at a given y -location could be expected to exhibit the same general trends as a bank of tubes. These correlations were then modified by calibration with C_f and St data on rough surfaces. This procedure is discussed in detail in Section V of this report.

The drag coefficient model developed is given by

$$\begin{aligned} \log C_D &= -0.125 \log(Re_d) + 0.375, & Re_d < 60,000 \\ C_D &= 0.6, & Re_d > 60,000 \end{aligned} \quad (36)$$

and the Nusselt number model by

$$\begin{aligned} Nu_d &= 2.475 Re_d^{0.4} Pr^{0.36}, & Re_d < 100 \\ Nu_d &= 1.043 Re_d^{0.5} Pr^{0.37}, & 100 < Re_d < 1000 \\ Nu_d &= 0.963 Re_d^{0.6} Pr^{0.36}, & 1000 < Re_d < 200,000 \\ Nu_d &= 0.060 Re_d^{0.84} Pr^{0.36}, & Re_d > 200,000 \end{aligned} \quad (37)$$

It should be noted that both C_D and Nu_d are functions of y through their dependence on the local Reynolds number, $Re_d = Ud(y)/\nu$, where both U and $d(y)$ are functions of y . Furthermore, they contain information on the element shape by means of the local diameter, $d(y)$.

4. REMARKS ON THE DISCRETE ELEMENT MODEL

At this point some remarks are in order. The reader will recall that in the preceding sections the three regimes of flow over a rough surface were discussed. No mention of these regimes has been made in the development of this model. All models that use the sand-grain roughness

approach must take care to distinguish between these regimes since different models are required for transitionally rough and fully rough flow. This brings forth the added burden of predetermination of the state of the flow.

The present model does not need to make these distinctions, since by its nature such information is implicitly included. Therefore, the one model applies to both transitionally rough and fully rough flows. In Sections VI and VII, the present model is compared with experimental data for both transitionally rough and fully rough flows with good results.

The delimitation of these three regimes is usually made using the magnitude of the roughness Reynolds number, Re_{k_s} . In the present model the concept of sand-grain roughness, k_s , has been abandoned. Even though the concepts of fully rough and transitionally rough flow may be artificial to some degree (witness Morris' [2] discussion of an alternate classification), they are a part of our fluid mechanics tradition that (unlike k_s) we do not yet wish to abandon. Therefore, some new delimiter is required. One candidate for this job is the ratio of apparent shear stress due to the elements to total apparent shear stress, τ_r/τ_T . At present, no limits are offered using the new delimiter due to a lack of data in the transitionally rough regime.

The present discrete element model development is for boundary layer flow. This form was chosen for two reasons: (1) almost all of the experimental data with which the model is compared are for boundary layer flows, and (2) the relatively efficient solution of the boundary layer flow saved much effort in the numerical experimentation that was necessary for the calibration of the model. However, the present discrete element model should be readily (albeit tediously) extendable to the full Navier-Stokes equations.

5. DEFINITION OF SKIN FRICTION, STANTON NUMBER, INTEGRAL LENGTH SCALES, AND THE ELEMENT TEMPERATURE

At this point formulae for the skin friction coefficient and Stanton number are given in terms of the discrete element model nomenclature. They are

Skin Friction Coefficient:

$$C_f = \frac{(1 - \alpha_y)_w \tau_w + \frac{1}{2} \frac{1}{Ll} \int_0^\infty \rho C_D dU^2 (dy)}{\frac{1}{2} \rho U_e^2} \quad (38)$$

Stanton Number:

$$St = \frac{(1 - \alpha_y)_w q_w + \int_0^\infty \frac{K\pi Nu_d (H_R - H)}{C_p L l} (dy)}{\rho_e U_e (H_w - H_{oe})} \quad (39)$$

The subscript w indicates values evaluated at the wall, and e indicates boundary layer edge conditions. The smooth wall shear stress τ_w is given by $\tau_w = -\mu(\partial u/\partial y)|_{y=0}$ and the heat flux q_w is $-k(\partial T/\partial y)|_{y=0}$.

These definitions can be formulated from physical reasoning; however, they also arise naturally in the formulation of the integral boundary layer equations for the discrete element model. These integral equations are derived in detail in Appendix B by integrating equations (19) - (21) across the boundary layer. During this process, definitions for the usual integral length scales (e.g., momentum thickness, enthalpy thickness, etc.) evolve. The formulae for these are given in Appendix B.

In the development of the energy equation, an element temperature was introduced. This temperature in the most general case will have a different value than the base wall temperature, T_w . The specification of this element temperature is rather involved and is discussed in detail in Appendix C. In the present work, all of the elements considered are firmly bonded and are constructed of highly conductive material. Therefore, here the element temperature is taken to be identical to the wall temperature.

SECTION IV

METHOD OF SOLUTION

The discrete element equations derived in Section III are first transformed using a modified Illingsworth transformation and then the transformed equations are solved using an iterative, marching, implicit finite difference technique.

1. THE EQUATIONS AND BOUNDARY CONDITIONS

The discrete element boundary layer equations and boundary conditions as solved are:

Continuity:

$$\frac{\partial}{\partial x} (\rho \beta_x U) + \frac{\partial}{\partial y} (\rho \beta_y V) = 0 \quad (40)$$

Momentum:

$$\begin{aligned} \rho \beta_x U \frac{\partial U}{\partial x} + \rho \beta_y V \frac{\partial U}{\partial y} &= \rho_e \beta_x U_e \frac{dU_e}{dx} \\ &+ \frac{\partial}{\partial y} \left[\beta_y (\mu + \mu_T) \frac{\partial U}{\partial y} \right] \\ &- \frac{1}{2} \rho C_D \frac{d}{Ll} U^2 \end{aligned} \quad (41)$$

Energy:

$$\begin{aligned} \rho \beta_x U \frac{\partial H}{\partial x} + \rho \beta_y V \frac{\partial H}{\partial y} &= \frac{\partial}{\partial y} \left[\beta_y \frac{K + K_T}{C_p} \frac{\partial H}{\partial y} \right] \\ &+ \beta_y (\mu + \mu_T) \left(\frac{\partial U}{\partial y} \right)^2 - \rho_e \beta_x U U_e \frac{dU_e}{dx} \\ &+ \frac{1}{2} \rho C_D \frac{d}{Ll} U^3 + \frac{\pi \mu Nu_d (H_R - H)}{Ll Pr} \end{aligned} \quad (42)$$

The associated boundary conditions are

$$y = 0 : U = V = 0, H = H_w \quad (43)$$

$$y \rightarrow \infty : U \rightarrow U_e, H \rightarrow H_e \quad (44)$$

Here the nomenclature has been abbreviated for compactness. The parameter β is the fraction of the control volume surfaces open to flow, that is, $\beta_x = (1 - \alpha_x)$ and $\beta_y = (1 - \alpha_y)$. Though not explicitly indicated, the parameters β , C_D , Nu_o , and d are all function of y . In addition, β is assumed not to be a function of x . For a uniform array β is indeed only a function of y , and for most nonuniform arrays β is to a good approximation only a quasi-function of x , i.e., $\partial\beta/\partial x \approx 0$. This assumption is not necessary; however, it considerably simplifies the following coordinate transformation. Also, all of the data sets with which we compare in subsequent sections satisfy this assumption.

In addition to the y -boundary conditions stated above the velocity, U , and the enthalpy, H , profiles must be stated at some initial x position. This is discussed in detail in Section IV.

2. THE MODIFIED ILLINGSWORTH TRANSFORMATION

Similar velocity and enthalpy profiles exist for turbulent flows only in isolated cases. However, considerable computational advantages occur if the solution variables and coordinate system are chosen such that similarity is approached. Here the Illingsworth variables that result in similarity for the classical smooth wall laminar cases are chosen (for a discussion of these cases, see White [34]).

The following coordinate transformation is used:

$$\xi = \xi(x) = \int_0^x \rho_e \mu_e U_e dx \quad (45)$$

$$\eta = \eta(x,y) = \frac{U_e \int_0^y \rho dy}{\sqrt{2\xi}} \quad (46)$$

A stream function, ψ , is defined such that

$$\frac{\partial\psi}{\partial y} = \rho\beta_x U \quad (47a)$$

and

$$\frac{\partial\psi}{\partial x} = -\rho\beta_y V \quad (47b)$$

where

$$\psi = \sqrt{2\xi} f(\xi, \eta) \quad (48)$$

Furthermore, let

$$g = H/H_e \quad (49)$$

From the definition of the stream function, ψ , continuity, (40), is satisfied exactly and the equations for conservation of momentum and energy become (in the new variables) after considerable manipulation

Momentum:

$$f''' + \gamma_{11} f'' + \gamma_{12} f' + \gamma_{13} + \gamma_{14} \frac{f'}{\partial \xi} = 0 \quad (50)$$

Energy:

$$g'' + \gamma_{21} g' + \gamma_{22} g + \gamma_{23} + \gamma_{24} \frac{\partial g}{\partial \xi} = 0 \quad (51)$$

where

$$\begin{aligned} \gamma_{11} &= \frac{\ell^*'}{\ell^*} + \frac{f}{\beta_y \ell^*} - \frac{\alpha_y'}{\beta_y} + \frac{2\alpha_x'}{\beta_x} + \frac{2\xi}{\beta_y \ell^*} \frac{\partial f}{\partial \xi} \\ \gamma_{12} &= \frac{-2\xi}{\beta_y U_e} \frac{\partial U_e}{\partial \xi} f' - \frac{\alpha_x' \alpha_y'}{\beta_x \beta_y} + \frac{2(\alpha_x')^2}{\beta_x^2} + \frac{\alpha_x''}{\beta_x} \\ &\quad + \frac{\alpha_x' \ell^*'}{\ell^* \beta_x} + \frac{\alpha_x' f}{\beta_x \beta_y \ell^*} + \frac{2\xi \alpha_x'}{\beta_x \beta_y \ell^*} \frac{\partial f}{\partial \xi} \\ &\quad - \frac{\xi C_D df'}{\beta_x \beta_y \rho_e \mu_e \ell^* L U_e} \\ \gamma_{13} &= \frac{\beta_x^2}{\beta_y \ell^*} \theta \frac{2\xi}{U_e} \frac{\partial U_e}{\partial \xi} \\ \gamma_{14} &= \frac{-2\xi f'}{\beta_y \ell^*} \end{aligned}$$

and

$$\begin{aligned} \gamma_{21} &= \frac{f}{\beta_y (\ell^{**}/Pr)} + \frac{2\xi}{\beta_y (\ell^{**}/Pr)} \frac{\partial f}{\partial \xi} - \frac{\alpha_y'}{\beta_y} + \frac{(\ell^{**}/Pr)'}{(\ell^{**}/Pr)} \\ \gamma_{22} &= \frac{-2\xi \pi \mu (Nu_d)}{\rho U_e^2 \rho_e \mu_e \beta_y (\ell^{**}/Pr) L Pr} - \frac{f' U_e}{\beta_y (\ell^{**}/Pr) H_e} \frac{2\xi}{\partial \xi} \frac{\partial U_e}{\partial \xi} - \frac{f' 2\xi}{\beta_y (\ell^{**}/Pr) H_e} \frac{\partial H_e}{\partial \xi} \end{aligned}$$

$$\begin{aligned} \gamma_{23} = & \frac{\ell^*}{(\ell^{**}/Pr)} \frac{U_e^2}{H_e} \left(\frac{f''}{\beta_x} + \frac{\alpha_x f'}{\beta_x^2} \right)^2 \\ & + \frac{\xi C_D dU_e (f')^3}{H_e \beta_y \beta_x^3 \rho_e \mu_e (\ell^{**}/Pr) L \ell} \\ & + \frac{2\xi \pi \mu (Nu_d) H_R}{\beta_y H_e \rho_e \mu_e (\ell^{**}/Pr) L \ell Pr} \end{aligned}$$

$$\gamma_{24} = \frac{-2\xi f'}{\beta_y (\ell^{**}/Pr)}$$

and

$$\ell^* = \frac{\rho \mu}{\rho_e \mu_e} \left(1 + \frac{\mu_T}{\mu} \right)$$

$$\ell^{**} = \frac{\rho \mu}{\rho_e \mu_e} \left(1 + \frac{K_T}{K} \right) = \frac{\rho \mu}{\rho_e \mu_e} \left(1 + \frac{Pr}{Pr_T} \frac{\mu_T}{\mu} \right)$$

$$\theta = \frac{\rho_e}{\rho} \quad (= g \text{ for ideal gases; } = 1 \text{ for incompressible flow})$$

The boundary conditions become in the new variables

$$\eta = 0 : f' = 0, f = 0, g = g_w \quad (52)$$

$$\eta \rightarrow \infty : f' = 1, g = 1 \quad (53)$$

The velocity components are obtained from the expressions

$$U = \frac{U_e f'}{\beta_x} \quad (54)$$

$$V = \frac{-1}{\rho \beta_y} \left(\rho_e \mu_e U_e \frac{f}{\sqrt{2\xi}} + \rho_e \mu_e U_e \sqrt{2\xi} \frac{\partial f}{\partial \xi} + \frac{\partial \eta}{\partial x} \sqrt{2\xi} f' \right) \quad (55)$$

In the above the prime (') indicates the partial derivative with respect to η , $\partial(\)/\partial\eta$.

At first glance equations (50), (51), and their modifiers appear to be much more intractable than their parents (equations (40) - (42)). However, we have gained computational advantages. We have eliminated one variable, V , and we have reduced the system of partial differential

equations to a system of quasi-ordinary differential equations with quasi-similar solutions, f' and g . In other words, we have sacrificed algebraic compactness for computational considerations.

3. THE IMPLICIT FINITE DIFFERENCE METHOD

The development below follows closely that for smooth surfaces referenced by Adams and Martindale [35]. Equations (50) and (51) are written in the general form

$$w'' + \gamma_1 w' + \gamma_2 w + \gamma_3 + \gamma_4 \frac{\partial w}{\partial \xi} = 0 \quad (56)$$

where $w = f'$ for the momentum equation and $w = g$ for the energy equation with a one to one correspondence for the γ 's. That is, $\gamma_1 = \gamma_{11}$ for the momentum equation and $\gamma_1 = \gamma_{21}$ for the energy equation. Again the prime indicates differentiation with respect to η .

The derivatives in equation (56) are approximated by finite difference formulas in the grid network shown in Figure 12. The grid

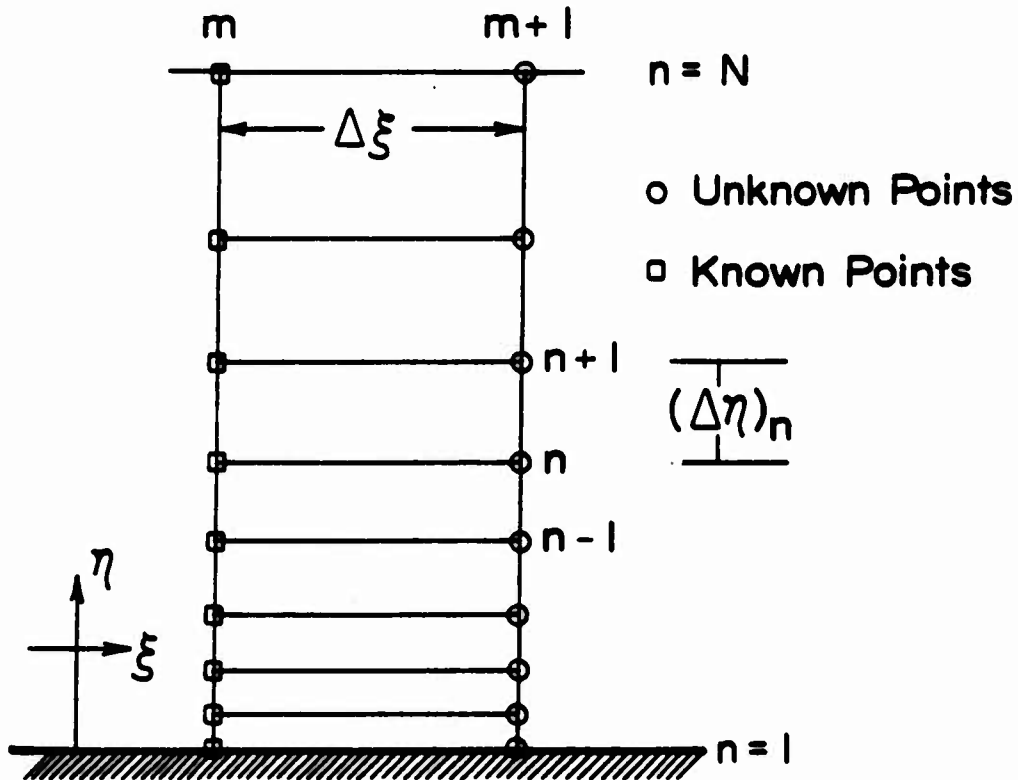


Figure 12. Layout of the Expanding Finite Difference Grid

spacing in the ξ -direction is a constant $\Delta\xi$. A geometrically expanding grid is used in the η -direction. This is given by the recursion formula

$$\Delta\eta|_n = R(\Delta\eta)_{n-1} \quad (57)$$

where R is a constant (taken here as $R = 1.063$). The first η -step, $\Delta\eta|_1$, must be specified and is taken here as $\Delta\eta|_1 = 0.005$. The expanding η -grid is chosen because it concentrates the points near the surface where the gradients are the steepest. With $R = 1.063$, $\Delta\eta|_1 = 0.005$ and $N = 120$, 43 η values are obtained with values less than 1 while the largest η value is 114. With this scheme on a typical run about half of the η -points are in the lower 5-10% of the boundary layer.

The derivatives with respect to the marching coordinate, ξ , are approximated by a two-point backward difference

$$\frac{\partial w}{\partial \xi}|_{m+1,n} = \frac{w_{m+1,n} - w_{m,n}}{\Delta\xi} \quad (58)$$

where all values at ξ -station m are known.

The derivatives with respect to the normal coordinate, η , are approximated by using a three-point Lagrangian interpolation formula. The dependent variable w is approximated in the range $\eta_{n-1} \leq \eta \leq \eta_{n+1}$ by a Lagrangian polynomial

$$w(\eta) = \sum_{i=n-1}^{n+1} L_i w_{m+1,i} + E \quad (59)$$

where

$$L_i = \frac{\prod_{\substack{j=n-1 \\ j \neq i}}^{n+1} (\eta - \eta_j)}{\prod_{\substack{j=n-1 \\ j \neq i}}^{n+1} (\eta_i - \eta_j)}$$

Taking the first and second derivatives of equation (59) and evaluating at $\eta = \eta_n$ yields the finite difference formulae

$$\frac{\partial^2 w}{\partial \eta^2}|_{m+1,n} = \frac{2[w_{n+1} + R w_{n-1} - (1+R)w_n]_{m+1}}{(\Delta\eta)_n^2 + R(\Delta\eta)_{n-1}^2} + E'' \quad (60)$$

$$\left. \frac{\partial w}{\partial \eta} \right|_{m+1, n} = \frac{[w_{n+1} - R^2 w_{n-1} - (1+R)w_n]_{m+1}}{(\Delta\eta)_n + R^2(\Delta\eta)_{n-1}} + E' \quad (61)$$

where

$$\Delta\eta|_n = \eta_{n+1} - \eta_n.$$

The errors can be shown to be [35] $E' = -(1/6)w'''(\Delta\eta)_n(\Delta\eta)_{n-1}$ and $E'' = -(1/12)w''''(\Delta\eta)_n(\Delta\eta)_{n+1}$. From this we see the usefulness of the expanding grid. Near the wall where the derivatives are large we need small values of $\Delta\eta$ to give small errors. Far from the wall the derivatives are small and larger $\Delta\eta$'s are acceptable.

Substituting equations (58), (60), and (61) into equation (56) and rearranging yields a system of $N-2$ algebraic equations

$$A_n w_{m+1, n-1} + B_n w_{m+1, n} + C_n w_{m+1, n+1} = D_n \quad (62)$$

where

$$n = 2, N-1$$

The coefficients A, B, C and D are given by

$$A_n = \frac{2R}{S_1} - \frac{R^2 \gamma_1}{S_2} \quad (63a)$$

$$B_n = -\frac{2(1+R)}{S_1} - \frac{\gamma_1(1-R^2)}{S_2} + \gamma_2 + \frac{\gamma_4}{\Delta\xi} \quad (63b)$$

$$C_n = \frac{2}{S_1} + \frac{\gamma_1}{S_2} \quad (63c)$$

$$D_n = -\gamma_3 + \frac{\gamma_4 w_{m, n}}{\Delta\xi} \quad (63d)$$

where

$$S_1 = (\Delta\eta)_n^2 + R(\Delta\eta)_{n-1}^2 \quad \text{and} \quad S_2 = (\Delta\eta)_n + R^2(\Delta\eta)_{n-1}.$$

The $N-2$ equations are linear if the terms A_n , B_n , C_n , D_n are taken to be constants at a station n . Inspection of equations (50) - (63) reveals that these parameters are not constant. To overcome this problem, the following linearization procedure is adopted. Initial

guesses for the velocity and enthalpy profiles (f' and g) are assumed (usually the known values from the previous ξ -station, m , are taken). The γ 's of equations (50) and (51) are evaluated on the basis of these profiles, and the now linear algebraic equations (62) are solved for the second approximation of the profiles. These approximations are used to obtain new approximations in an iterative manner until the difference between two successive approximations is less than a preset percentage.

This solution yields values for f' , not f . Inspection of equations (50) and (51) reveals that values for f must be obtained during the iterative process. These values are obtained by means of numerical integration of the f' profile. In addition, values for α_x' , α_y' , l^* , l^{**} , etc. are obtained by way of the three-point Lagrangian finite difference formulae discussed above.

One advantage of this formulation from a computational standpoint is the special tridiagonal nature of the linearized equations (62). These equations are shown in matrix form in Figure 13(a). The matrix of coefficients is readily transformed into the Jordan canonical form, Figure 13(b), by the relations

$$\lambda_2 = \frac{B_2}{C_2} \quad (64a)$$

$$E_2 = \frac{D_2 - A_2 w_1}{C_2} \quad (64b)$$

$$\lambda_n = \frac{B_n}{C_n} - \frac{A_n}{C_n \lambda_{n-1}}, \quad n = 3, N-3 \quad (64c)$$

$$E_n = \frac{D_n}{C_n} - \frac{E_{n-1} A_n}{C_n \lambda_{n-1}}, \quad n = 3, N-3 \quad (64d)$$

$$\lambda_{N-1} = B_{N-1} - \frac{A_{N-1}}{\lambda_{N-2}} \quad (64e)$$

$$E_{N-1} = (D_{N-1} - C_{N-1} w_N) - \frac{A_{N-1} E_{N-2}}{\lambda_{N-2}} \quad (64f)$$

$$\begin{bmatrix} B_2 & C_2 & 0 & 0 & 0 & \cdot & \cdot & \cdot & 0 \\ A_3 & B_3 & 0 & 0 & 0 & \cdot & \cdot & \cdot & 0 \\ 0 & A_4 & B_4 & C_4 & 0 & \cdot & \cdot & \cdot & 0 \\ \cdot & \cdot \\ \cdot & \cdot \\ 0 & \cdot & \cdot & \cdot & \cdot & 0 & A_{N-1} & B_{N-1} & \cdot \end{bmatrix}
 \begin{bmatrix} w_2 \\ w_3 \\ \cdot \\ \cdot \\ \cdot \\ w_{N-2} \\ w_{N-1} \end{bmatrix}
 =
 \begin{bmatrix} D_2 - A_2 w_1 \\ D_3 \\ \cdot \\ \cdot \\ \cdot \\ D_{N-2} \\ D_{N-1} - C_{N-1} w_N \end{bmatrix}$$

(a)

$$\begin{bmatrix} \lambda_2 & 1 & 0 & 0 & 0 & \cdot & \cdot & \cdot & 0 \\ 0 & \lambda_3 & 1 & 0 & 0 & \cdot & \cdot & \cdot & 0 \\ \cdot & \cdot \\ \cdot & \cdot \\ 0 & 0 & \cdot & \cdot & \cdot & 0 & \lambda_{N-2} & 1 & \cdot \\ 0 & 0 & \cdot & \cdot & \cdot & 0 & 0 & \lambda_{N-1} & \cdot \end{bmatrix}
 \begin{bmatrix} w_2 \\ w_3 \\ \cdot \\ \cdot \\ \cdot \\ w_{N-2} \\ w_{N-1} \end{bmatrix}
 =
 \begin{bmatrix} E_2 \\ E_3 \\ \cdot \\ \cdot \\ \cdot \\ E_{N-2} \\ E_{N-1} \end{bmatrix}$$

(b)

Figure 13. Matrix Form of Linearized Equations: (a) Tridiagonal Form; (b) Canonical Form

where w_1 and w_N are known from the boundary conditions, equations (52) and (53). The canonical form is easily solved for the w_n 's by starting at station $N-1$

$$w_{N-1} = E_{N-1} / \lambda_{N-1} \quad (65)$$

and back substituting

$$w_n = \frac{E_n}{\lambda_n} - \frac{w_{n+1}}{\lambda_n} \quad n = N-2, N-3, \dots, 2 \quad (66)$$

Here the ξ -station subscript, $m+1$, has been omitted for compactness.

As stated previously, the velocity and enthalpy profiles must be specified at some initial ξ -station. One method is to use experimentally determined profiles at some location on the particular body under consideration and to then calculate the flow field downstream of this station. This scheme has the obvious disadvantage of requiring experimental data on every surface that is to be considered. Here the following scheme is followed to obtain initial profiles.

For bodies with sharp leading edges, such as plates, wedges, cones, etc., the boundary layer equations are singular at the leading edge and meaningful velocity and enthalpy profiles cannot be obtained. However, starting profiles of the transformed variables, f' and g , can be obtained. The scheme is to set the coefficients, γ 's, in equations (50) and (51) so that the well-known Blasius equations are obtained. These equations are solved using the implicit method discussed above with some arbitrary initial profile guess. For the case of incompressible, constant property, laminar flow without pressure gradients, this scheme yields the correct profiles at every ξ -station. For other cases this scheme may introduce slight errors in the solutions at the first few ξ -stations; however, these errors wash out after only a few ξ -steps.

For bodies with stagnation points,

$$U_e \approx \left. \frac{dU_e}{dx} \right|_{x=0} x \quad (67)$$

near $x = 0$. Equations (50) and (51) reduce to the classical Faulkner-Skan stagnation flow equations at $x = 0$ (hence $\xi = 0$). These equations are then solved using the implicit method with arbitrary initial

profile guesses. The initial guesses used here are $f'(\eta) = 1 - \exp(-\eta)$ and $g(\eta) = g_w - (1 - g_w)f'(\eta)$.

4. FULLY DEVELOPED FLOWS

The above discussion is concerned with the more interesting case of the developing boundary layer. However, many important applications and much of the experimental data that is used for verification of the present model are fully developed flows. The discrete element model is readily applied to such flows. For fully developed flow $V \equiv 0$, and U and H are functions of y only (i.e., $U = U(y)$ and $H = H(y)$); therefore, the boundary layer equations (41) and (42) (and, also, the full Navier-Stokes equations) become the ordinary differential equations

$$0 = -\beta_x \frac{dP}{dx} + \frac{d}{dy} \left[\beta_y (\mu + \mu_T) \frac{dU}{dy} \right] - \frac{1}{2} \rho C_D \frac{d(y)}{Ll} U^2 \quad (68)$$

$$0 = \frac{d}{dy} \left[\beta_y \left(\frac{K + K_T}{C_p} \right) \frac{dH}{dy} \right] + \beta_y (\mu + \mu_T) \left(\frac{dU}{dy} \right)^2 + \beta_x U \frac{dP}{dx} + \frac{1}{2} \rho C_D \frac{d(y)}{Ll} U^3 + \frac{\pi \mu (Nu_d) (H_R - H)}{Ll Pr} \quad (69)$$

In this form the modified Illingsworth transformations (equations (45) - (49)) are awkward, since there is no previously known reference velocity and enthalpy (such as U_e and H_e). However, no computational advantage is gained by transforming the above equations, since they are already ordinary differential equations. These equations are readily solved using the implicit finite difference method discussed above with $w = U$ and/or H , $\eta = y$, and the appropriate boundary conditions.

5. COMPUTER PROGRAM

The implicit finite difference method described above has been programmed for incompressible, constant property boundary layer flow in the Fortran IV Plus language on the Digital Equipment Corporation PDP-11/34 minicomputer. Typical runs take 5-10 seconds per ξ -step.

The assumption of incompressible, constant property flow was used here because all of the experimental data with which the model is compared in this work meets this assumption. It should be pointed out that the model is by no means limited to incompressible, constant property flows. In fact, the discrete element model has been coded and run in the compressible variable property form in a code similar to the one described by Hodge and Adams [21].

SECTION V

CALIBRATION OF THE MODEL

As with any procedure that requires some empirical input, the discrete element model must be calibrated. The calibration procedure here has three parts: (1) comparison of the model/computer program with smooth wall results, (2) calibration of the momentum transport model, and (3) calibration of the energy transport model.

1. SMOOTH SURFACE RUNS

The discrete element roughness model and computer program must correctly predict the flow over a smooth surface in the limit of vanishing roughness if the model/program is to be considered correct. The roughness program was run for conditions corresponding to Kearney's [36] zero pressure gradient smooth wall data for $U_e = 7$ m/s. To model the smooth surface, the roughness model was simply turned off, i.e., the α 's, d , etc. were set to zero.

Figure 14 shows the comparison between the predictions and data for Stanton number, St , and skin friction coefficient, C_f . The symbols are the data points, and the curves are the predictions. The bars shown on selected data points show the reported experimental uncertainty ($\pm 10\%$ for C_f and ± 0.0001 for St). Inspection of the figure reveals that the agreement is excellent. The predictions are everywhere within the data uncertainty.

From the above it can then be concluded that the model/program (exclusive of those parts dealing with the roughness) is correct. The reader should note that the present turbulence model has been tested by others for other boundary conditions, e.g., $dP/dx \neq 0$.

2. MOMENTUM TRANSPORT MODEL

The discrete element model contains a term to account for drag on the roughness elements. This drag is cast in terms of a nondimensional drag coefficient parameter, C_D . It is this drag coefficient that contains the necessary empirical information on the relationship between the roughness elements and surrounding flow. Our calibration of the roughness model for momentum transport consists of the specification of such a relationship.

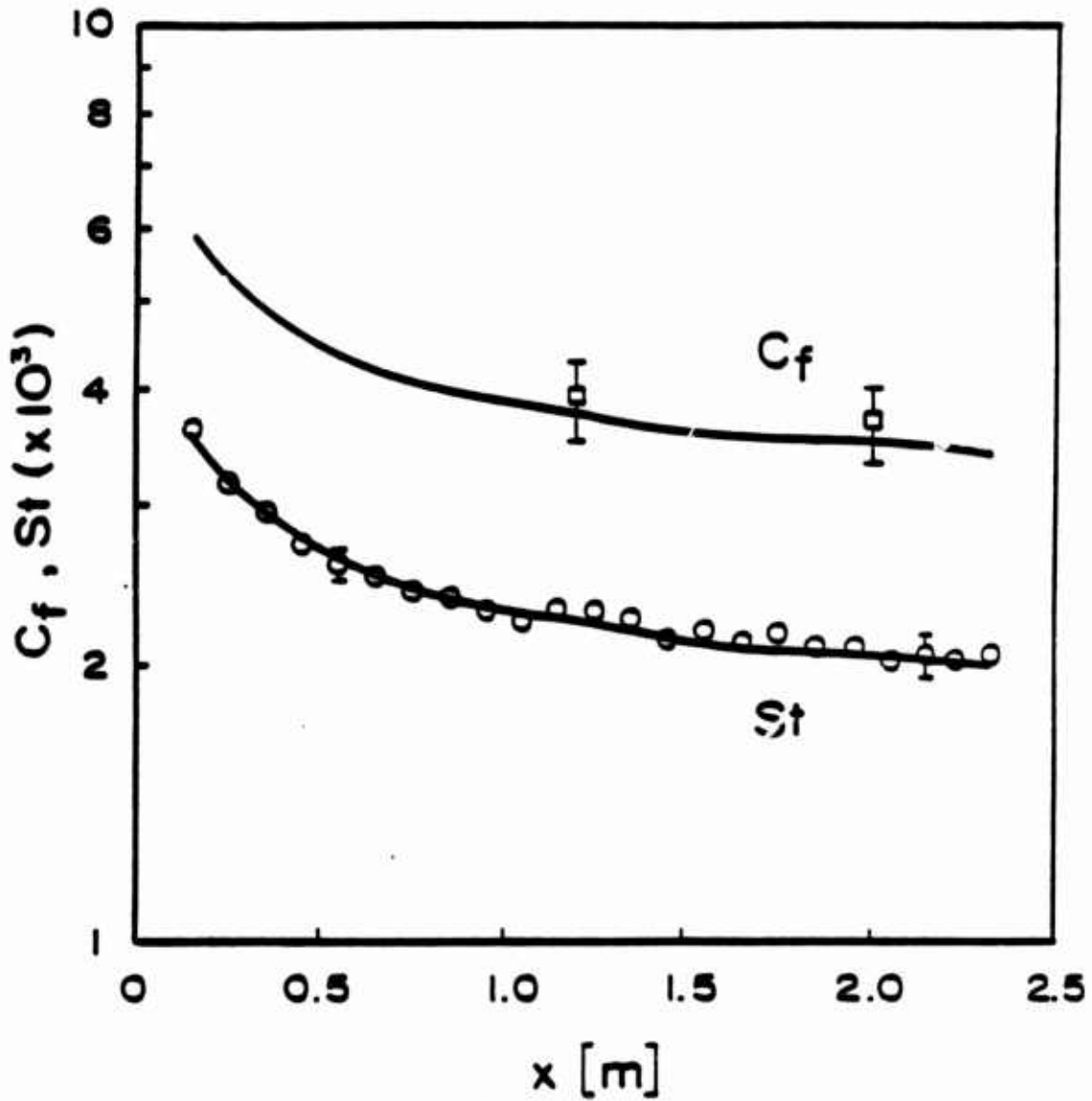


Figure 14. Comparison of Calculations with the Smooth Wall Data of Kearney [36]; $U_e = 7$ m/s

Some previous workers, namely Finson [26] and Christoph and Pletcher [28], have used a constant value of C_D . They selected that value which seemed to give the best overall agreement with their base data sets (i.e., Schlichting [3]). This scheme has a disadvantage in that C_D must be selected for each roughness shape. Finson and Clark [25] had good agreement for surfaces roughened with spheres and spherical segments using a constant $C_D = 0.6$, but they had poorer results for the surface roughened with cones when the same value of C_D was used.

Lin and Bywater [20] used the correlations for banks of cylinders given by Zukauskas [33]. These correlations take C_D to be a function of the local element Reynolds number that is calculated based on the local velocity, U , and the local element diameter, $d(y)$. However, they evidently failed to realize that Zukauskas' curves were expressed in terms of a pressure drop parameter and not a drag coefficient, i.e., they took the vertical coordinate of Zukauskas' Figure 64 on page 155 of reference [33] to be C_D , not the correct $[(d(y)/\ell)C_D]$.

Here, also, the curves from Zukauskas [33] are used, but only as a starting point in the specification of a formula for $C_D(Re_d)$. It was decided that to simplify the model, the explicit spacing (ℓ/d) dependence of C_D should be dropped. The basis for this decision was the fact that a constant value of C_D gives good agreement for a particular roughness shape, e.g., spheres, over a wide range of roughness spacings. Furthermore, spacing effects are already included as an integral part of the present discrete element model. Here and in the section on calibration of the energy transport model that follows the tube bank correlations are used as a starting point because in a differential control volume, e.g., Figure 5, the element slices appear to be similar to a slice through a bank of cylinders when the elements have circular (or almost circular) cross-sections.

To calibrate the model, various functions, $C_D(Re_d)$, were tested and the results of the calculations were then compared with a base data set. The function that seemed to give the best overall agreement with the base data set was then selected. Here the data set of Schlichting [3] was chosen as the base. This data set was chosen because it is the most comprehensive data set for flow over rough surfaces where the roughness geometry is well defined.

As discussed previously, Schlichting investigated seven roughness shapes over a wide range of spacings and over a range of Reynolds numbers for a total of 124 runs. In fact, this data set has been the base for almost all rough wall flow analyses, including both computational ones and empirical ones. Since in this work we concern ourselves only with three-dimensional roughness elements, only the data for spheres, spherical segments, and cones are used in the present calibration.

In the course of this procedure a careful study of Schlichting's report [3] revealed that his data reduction method was flawed. His data reduction method and the necessary corrections are discussed in detail in Appendix A. In the present calibration of the $C_D(Re_d)$ model, the corrected skin friction coefficient values given in Appendix A are used as the data base.

Starting with functions (C_D vs. Re_d) that had the general shape of the curves given by Zukauskas [33], several different formulae were tested. After some numerical experimentation the following function was adopted:

$$\begin{aligned} \log C_D &= -0.125 \log(Re_d) + 0.375, & Re_d < 60,000 \\ C_D &= 0.6, & Re_d > 60,000 \end{aligned} \quad (70)$$

Figure 15 shows a plot of this function.

While equation (70) and Figure 15 indicate a relationship for Reynolds numbers as large as 10^6 , the present model has been verified only for roughness element Reynolds numbers up to $Re_d \approx 25,000$. The selection of equation (70) was subjective. That is, a rigorous optimization procedure was not used. The function that seemed to give the most satisfactory overall results for all of Schlichting's cases was selected.

3. WALL LOCATION FOR MOST DENSELY PACKED SPHERES

Recalling the discussion in Section III, it is seen that the discrete element model divides the net tangential force on the surface into two components: (1) the viscous shear on the smooth base wall and (2) the drag on the roughness element. Most rough surfaces have fairly well-defined base walls. However, for spheres packed in the most dense array a well-defined base wall does not exist. Schlichting [3] recognized this problem in his original article: he arbitrarily took the base wall to be

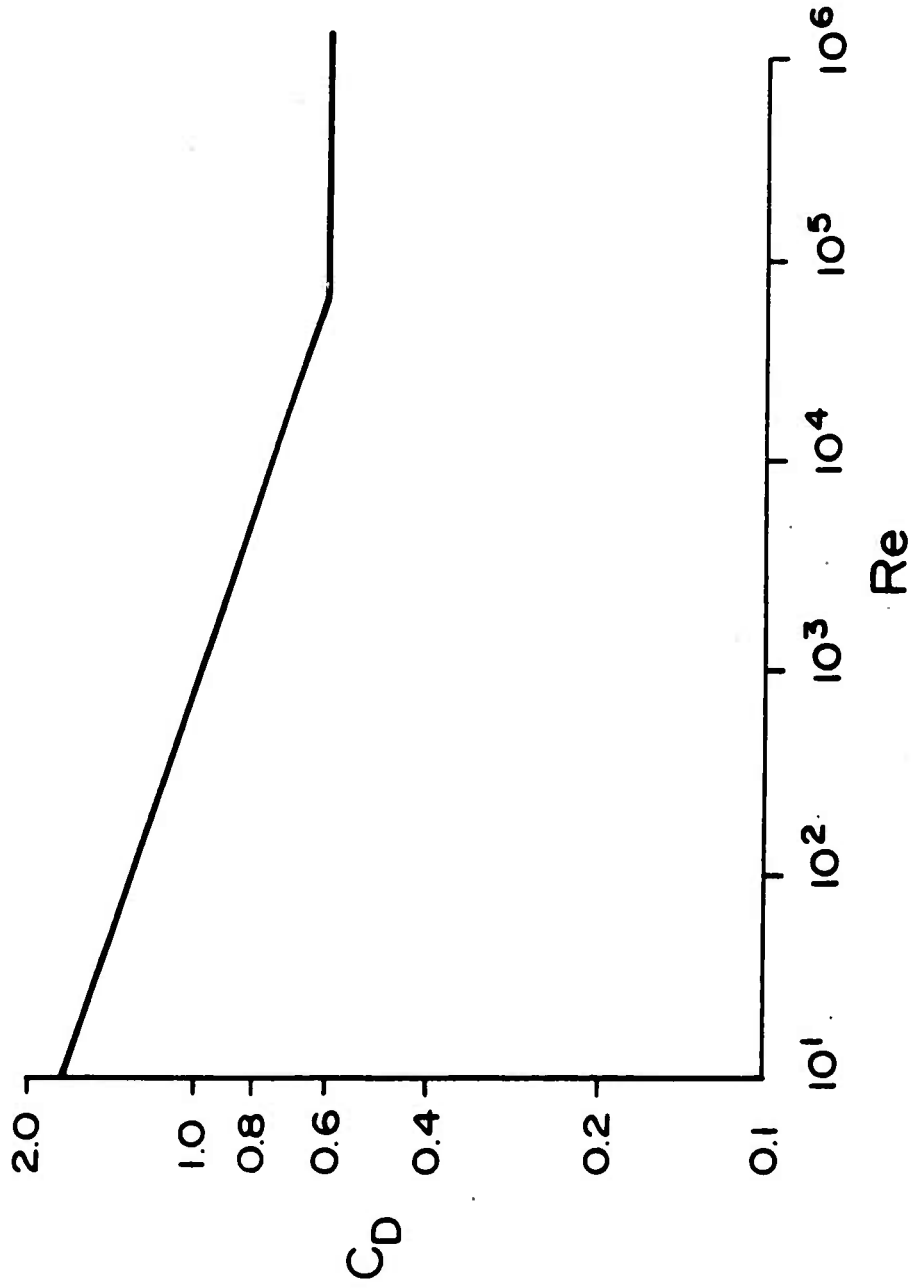


Figure 15. Roughness Element Drag Coefficient Model

at the plane of the equators. The more recent workers [25,26] have adopted the same approach. The general wisdom is that the region below the equators offers such a high flow resistance that the flow rate below this plane is negligible. However, it is more likely that for densely packed spheres there is a region of recirculating flow below the plane of the equators as shown in Figure 16. Close examination of the geometry of the most densely packed spheres shown in the figure reveals that there are most likely two regions of recirculating flow (one above the equators and one below).

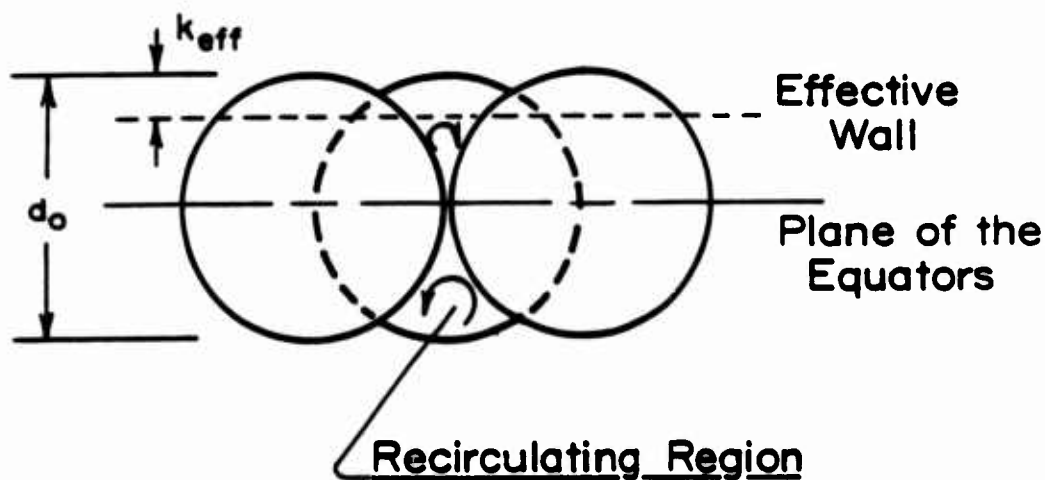


Figure 16. Schematic of Most Densely Packed Spheres

In the absence of data on this phenomenon, the following procedure was adopted to find the correct (or at least a good approximation thereof) effective wall location for spheres packed in the most dense array. Using the model as calibrated for the preponderance of Schlichting's data, several locations for the effective wall location were tested and the one that gave the best overall results for Schlichting's [3] skin friction data for most densely packed spheres was chosen. The value chosen was $k_{eff} = d_o/5$. It is coincidental (but interesting nonetheless) that this effective wall location is almost identical to Schlichting's "melt down" effective wall location discussed in Section II.

4. ENERGY TRANSPORT MODEL

The discrete element energy transport model requires empirical input in the form of a Nusselt number, Nu_d . As with the momentum transport model, the starting point was the correlation reported by Zukauskas [33] for banks of tubes. Lin and Bywater [20] used the same correlations in their work; however, they used the correlations directly rather than as a starting point in a calibration procedure.

Here a model was formulated using the correlations of Zukauskas [33] as a starting point, conducting numerical experiments using modified correlations, and then comparing the results of these experiments with a base data set. The data set chosen as the base was the 27 m/sec experimental run by Pimenta [4] at Stanford University. This data set was chosen because it is representative of the very comprehensive rough surface heat transfer work carried out at Stanford [4,5,6,32].

The Stanford data were all taken on a rough surface consisting of spheres packed in the densest array. Therefore, the effective wall location determined for Schlichting's most densely packed spheres was used.

After the numerical experiments, the following Nusselt number model was chosen:

$$Nu_d = 2.475 Re_d^{0.4} Pr^{0.36}, \quad Re_d < 100 \quad (71a)$$

$$Nu_d = 1.043 Re_d^{0.5} Pr^{0.37}, \quad 100 < Re_d < 1000 \quad (71b)$$

$$Nu_d = 0.963 Re_d^{0.6} Pr^{0.36}, \quad 1000 < Re_d < 200,000 \quad (71c)$$

$$Nu_d = 0.060 Re_d^{0.84} Pr^{0.36}, \quad Re_d > 200,000 \quad (71d)$$

Figure 17 shows a plot of equations (71). It should be pointed out that the model presented in equations (71) and the figure have only been verified for Reynolds numbers up to $Re_d = 1000$. Extrapolations of the verified model using the trends of Zukauskas' data are presented here for completeness.

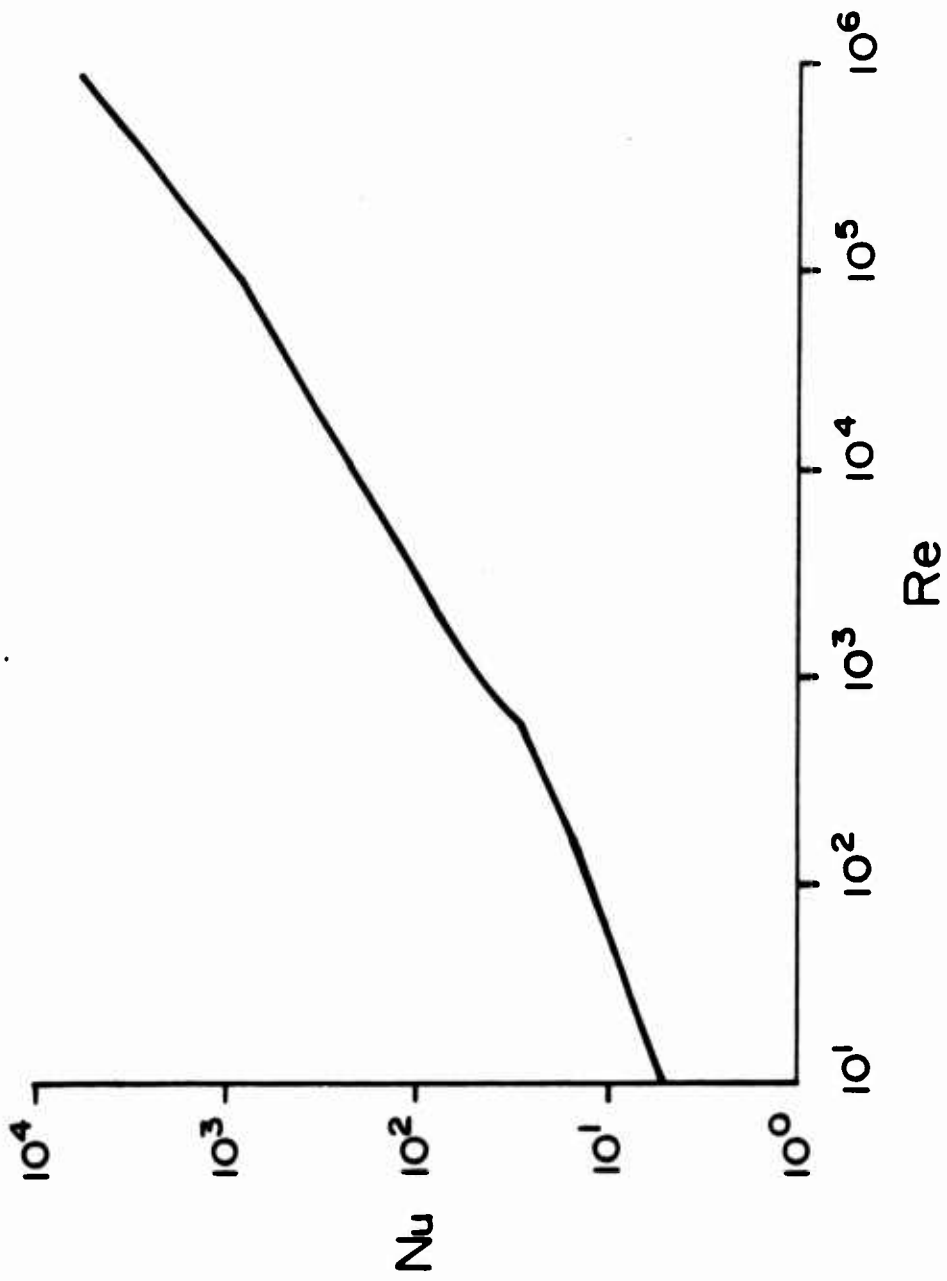


Figure 17. Roughness Element Nusselt Number Model

SECTION VI

FULLY DEVELOPED FLOW RESULTS

The discrete element model developed and calibrated in the preceding sections has been applied to two fully developed flow experiments, and the results of the calculations are compared below to the results of the experiments.

1. SCHLICHTING'S EXPERIMENT

As discussed previously, Schlichting investigated several different roughness shapes over a range of spacings and Reynolds numbers. In this section the results of the present model are compared with the results of his experiments. Since this work is concerned with three-dimensional roughness elements, only the spheres, spherical segments, and cones are considered here.

As discussed in Section V and in Appendix A, Schlichting's [3] data reduction method for skin friction coefficient was flawed, and it was necessary to correct this data. In the following, all comparisons are made with the corrected data. It should be noted that these data sets were used to calibrate the roughness model. The calculated results cannot, therefore, be considered as predictions.

Table 1 shows a comparison of the calculated skin friction coefficients, C_f , with measured (corrected) values. Figures 18 - 20 present these results in graphical form. The uncertainty bands shown in the figures represent $\pm 10\%$ about the (corrected) measured data. While Schlichting did not report data uncertainties, it is felt that $\pm 10\%$ is the smallest uncertainty which can be claimed for these data considering the corrections which were necessary to the originally reported values.

For the calculations, the discrete element model was solved in the proper channel coordinates. The calculated values of τ_w were normalized using the measured value of the maximum velocity, U_{\max} , (i.e., $C_f = 2\tau_w / \rho U_{\max}^2$). The maximum velocity was chosen here because Schlichting did not report average velocities. Inspection of the table (and figures) reveals good overall agreement. The calculations are, for the most part, within 10% of the measured results for 11 of the 14 plates. However, substantial disagreement is observed for three of the plates: plates XIII

TABLE 1. COMPARISON WITH SCHLICHTING'S RESULTS

PLATE NO. (l/k)	Re $\times 10^{-3}$	U_{\max} (cm/sec)	MEASURED $C_{fc} \times 10^3$	CALCULATED $C_f \times 10^3$	% DIFF
SPHERES					
XII (9.75)	100	321	6.29	6.61	5.1
	124	385	6.24	6.33	1.4
	162	476	6.46	6.09	-5.7
	190	547	6.29	6.00	-4.2
	224	650	5.69	5.90	3.7
III (4.88)	107	316	8.66	9.61	10.9
	138	391	9.18	9.20	0.2
	174	500	8.70	9.22	6.0
	204	568	9.01	9.19	2.0
	251	704	8.95	9.09	1.6
	290	816	8.99	8.94	-0.4
I (2.44)	107	310	18.13	16.22	-10.5
	132	384	17.87	15.75	-11.8
	166	508	16.42	15.54	-5.5
	195	566	16.11	15.43	-4.2
	224	658	16.42	15.34	-6.8
	263	778	16.37	15.32	-6.4
II (1.46)	104	313	15.46	15.17	-1.9
	129	384	16.73	15.60	-6.7
	166	500	17.23	15.94	-7.4
	186	586	17.17	16.17	-5.8
	224	646	17.57	16.37	-6.8
	257	746	18.00	16.49	-8.4
V (0.87)	98	311	8.08	8.93	10.5
	123	385	8.44	9.02	6.8
	162	498	8.37	9.07	8.4
	190	585	8.52	9.06	6.3
	214	662	8.56	9.13	6.7
	263	809	8.86	9.10	2.7
VI (4.86)	110	316	7.12	7.85	10.2
	135	390	6.82	7.80	14.4
	170	491	7.55	7.71	2.1
	200	566	7.61	7.65	0.5
	234	664	7.21	7.62	5.7
	275	806	7.32	7.63	4.1
IV (2.43)	107	325	13.50	12.55	-7.0
	129	391	12.02	12.21	1.6
	186	572	12.90	11.97	-7.2
	204	646	12.59	11.84	-6.0
	245	751	12.53	11.85	-5.4

TABLE 1. COMPARISON WITH SCHLICHTING'S RESULTS (CONCLUDED)

PLATE NO. (l/k)	Re $\times 10^{-3}$	U_{\max} (cm/sec)	MEASURED $C_{fc} \times 10^3$	CALCULATED $C_f \times 10^3$	% DIFF
SPHERICAL SEGMENTS					
XIII (15.4)	115	314	4.32	5.64	30.5
	141	389	3.72	5.23	40.6
	178	495	4.37	5.08	16.2
	204	574	4.40	4.99	13.4
	229	658	3.70	4.92	33.0
	302	830	3.33	4.86	46.0
XIV (11.5)	135	380	4.12	5.89	43.0
	174	497	4.57	5.68	24.3
	195	572	4.87	5.61	15.2
	245	700	3.68	5.49	49.2
	295	834	3.50	5.43	55.1
XV (7.69)	135	382	7.16	7.70	7.5
	170	502	7.42	7.56	1.9
	190	564	7.04	7.46	6.0
	234	687	6.51	7.43	14.1
	288	817	6.79	7.40	9.0
XIX (2.65)	107	316	9.93	10.59	6.6
	132	386	9.75	10.60	8.7
	158	480	10.27	10.51	2.3
	186	563	9.08	10.51	15.7
	224	671	10.21	10.56	3.4
	282	818	10.25	10.60	3.4
CONES					
XXIII (10.7)	117	321	4.67	5.80	24.0
	141	386	4.89	5.70	16.3
	178	488	4.69	5.66	26.7
	214	574	4.84	5.58	15.2
	251	668	5.12	5.54	8.2
XXIV (8.00)	112	307	7.81	7.53	3.0
	141	384	6.88	7.18	4.4
	186	495	6.77	6.87	1.5
	209	567	6.39	6.77	5.9
	251	662	6.19	6.65	7.4
	324	890	6.38	6.54	2.5
XXV (5.33)	115	310	10.32	9.42	-8.7
	145	388	8.93	9.16	2.6
	178	476	8.91	9.18	3.0
	209	564	9.38	9.18	-2.8
	251	668	9.34	9.20	-1.5
	295	787	9.42	9.18	-2.5

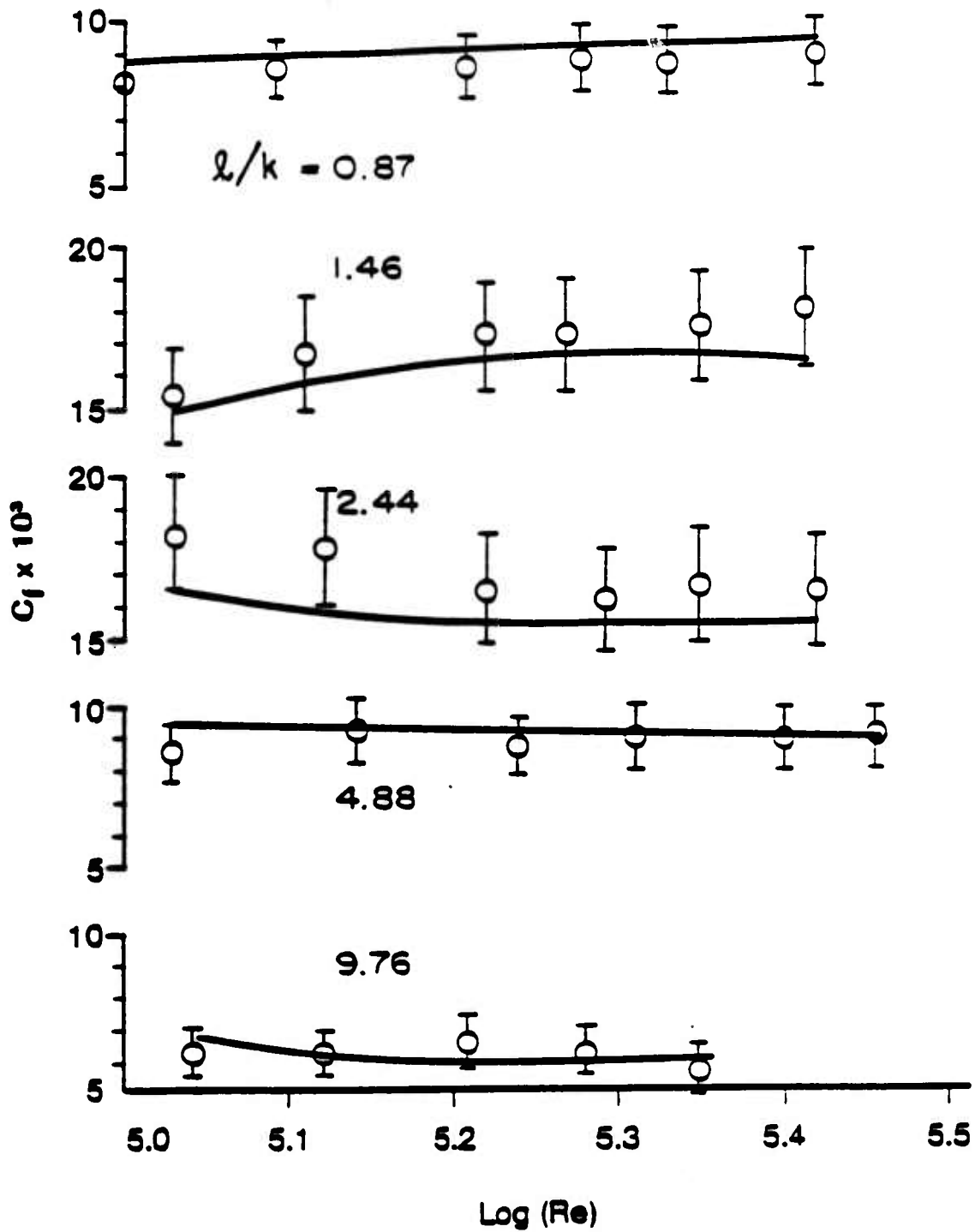


Figure 18. Comparison of Calculations with the Corrected Skin Friction Data of Schlichting for Spheres

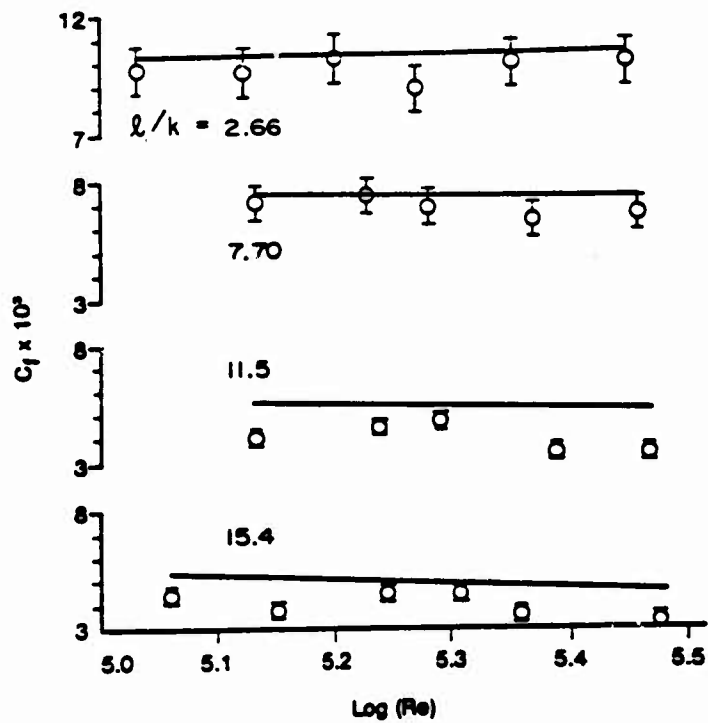


Figure 19. Comparison of Calculations with the Corrected Skin Friction Data of Schlichting for Spherical Segments

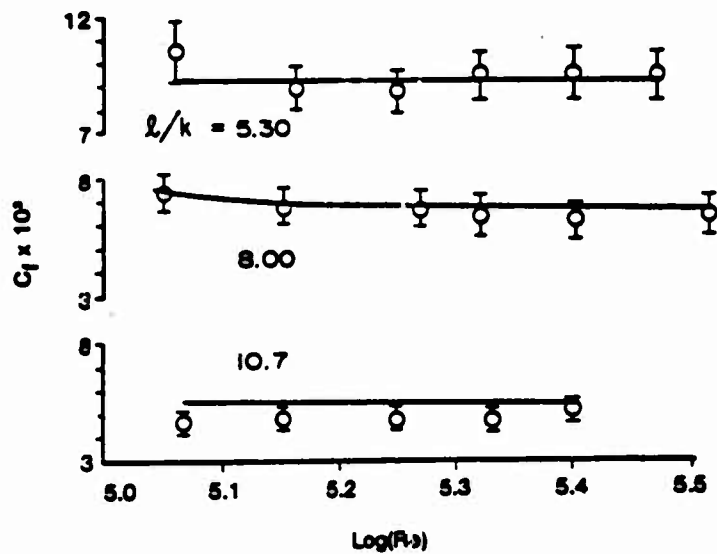


Figure 20. Comparison of Calculations with the Corrected Skin Friction Data of Schlichting for Cones

and XIV with spherical segments and plate XXIII with cones. For these three plates the calculated values of C_f are from 8% to 55% larger than the corrected data. No satisfactory explanation for this disagreement has been found. As discussed in the appendix, these three plates are probably in the transitionally rough regime and not the fully rough regime, as originally reported by Schlichting. However, as shown below in this section and in Section VII, the present discrete element model successfully predicts other transitionally rough flows. This disagreement is not viewed with undue concern, since the model (as will be shown) extrapolates well to other experimental data which were not used in the calibration of the model.

Figure 21 shows a comparison of the calculations and data as a function of roughness density for the spherical roughness elements. Inspection of the figure reveals that the discrete element model correctly predicts the relative maximum in the C_f --roughness density relationship, the maximum value of C_f occurring at a density which is somewhat less than the maximum density.

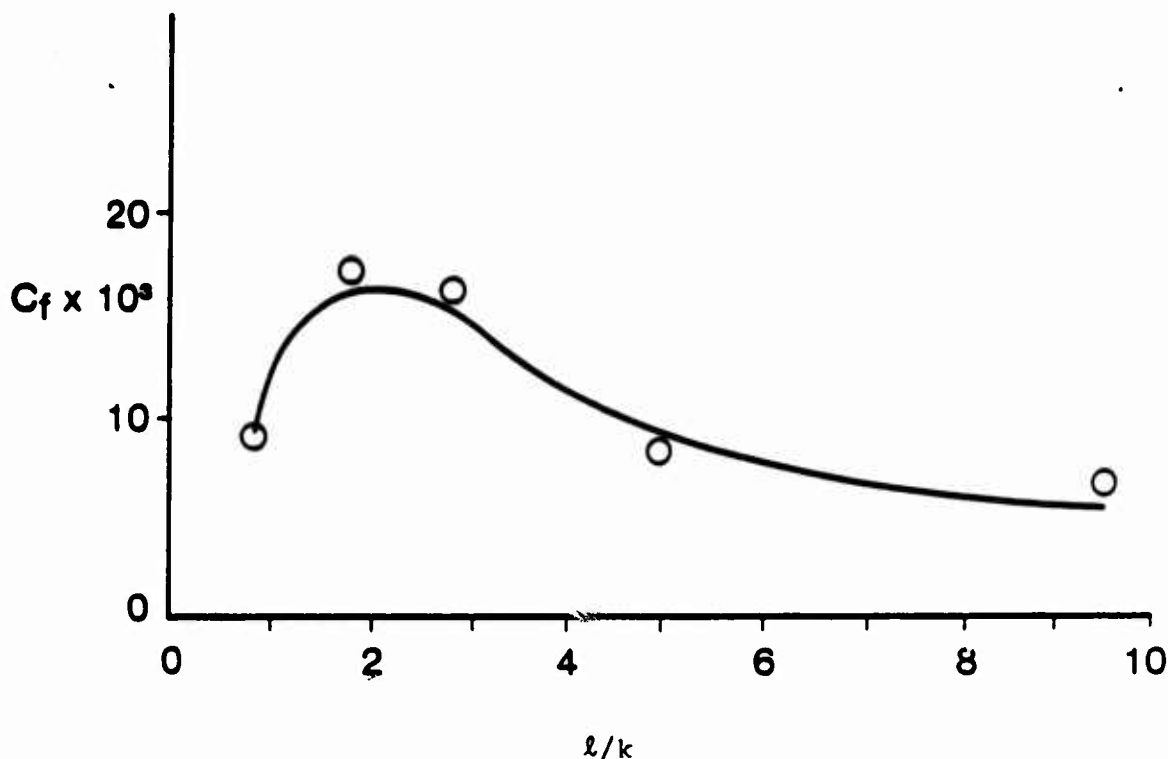


Figure 21. The Effect of Roughness Element Spacing on Skin Friction for Schlichting's Spheres; $Re \approx 200,000$

The generally good agreement with Schlichting's data is not surprising since this very same data set was used to calibrate the discrete element momentum transport model. The model (with only changes that account for geometric differences, e.g., from channel to pipe flow) has been compared to independent data sets. The pipe flow data of Chen [37] are discussed below, and the extensive boundary layer data of the Stanford experiments are discussed in Section VII.

2. CHEN'S EXPERIMENT

Chen [37] reported detailed turbulence and skin friction measurements for air flow through a 0.19-meter-diameter pipe roughened with hemispheres. He investigated three roughness densities-- $\ell/k = 18.5, 10.7,$ and 6.4 . Chen stated that the first two cases ($\ell/k = 18.5$ and 10.7) were in the transitionally rough regime, and the third ($\ell/k = 6.4$) was nearly in the fully rough regime. The most interesting part of Chen's work (from the point of view of the present work) is the segregation of the two components of the apparent wall shear stress: (1) that due to the viscous shear on the smooth surface between the roughness elements and (2) that due to the form drag on the roughness elements. Chen obtained the form drag term by measuring the force on a single element using a force balance. The portion due to the smooth surface was determined by subtracting the roughness element drag component from the total wall shear stress which was determined from pressure drop measurements.

The discrete element model was solved in the appropriate internal circular coordinates, and the resulting predictions were compared with Chen's data. Figures 22 - 24 show the comparisons for the skin friction coefficient and the ratio of the smooth wall component to the total shear stress. Here the average velocity was used to normalize the skin friction coefficient ($C_f = 2\tau_w / \rho U_{ave}^2$). The average velocity was chosen since Chen reported the maximum velocity only for a limited number of cases while the average velocity was reported for all cases.

Inspection of the figures reveals very good agreement for C_f for the first two cases ($\ell/k = 18.5$ and 10.7). From Figures 22 and 23 it is seen that the maximum disagreement is 9%. From Figure 24, it is seen that fair agreement is obtained for the third case ($\ell/k = 6.4$); the maximum disagreement is 15%. The greatest part of this 15% disagreement

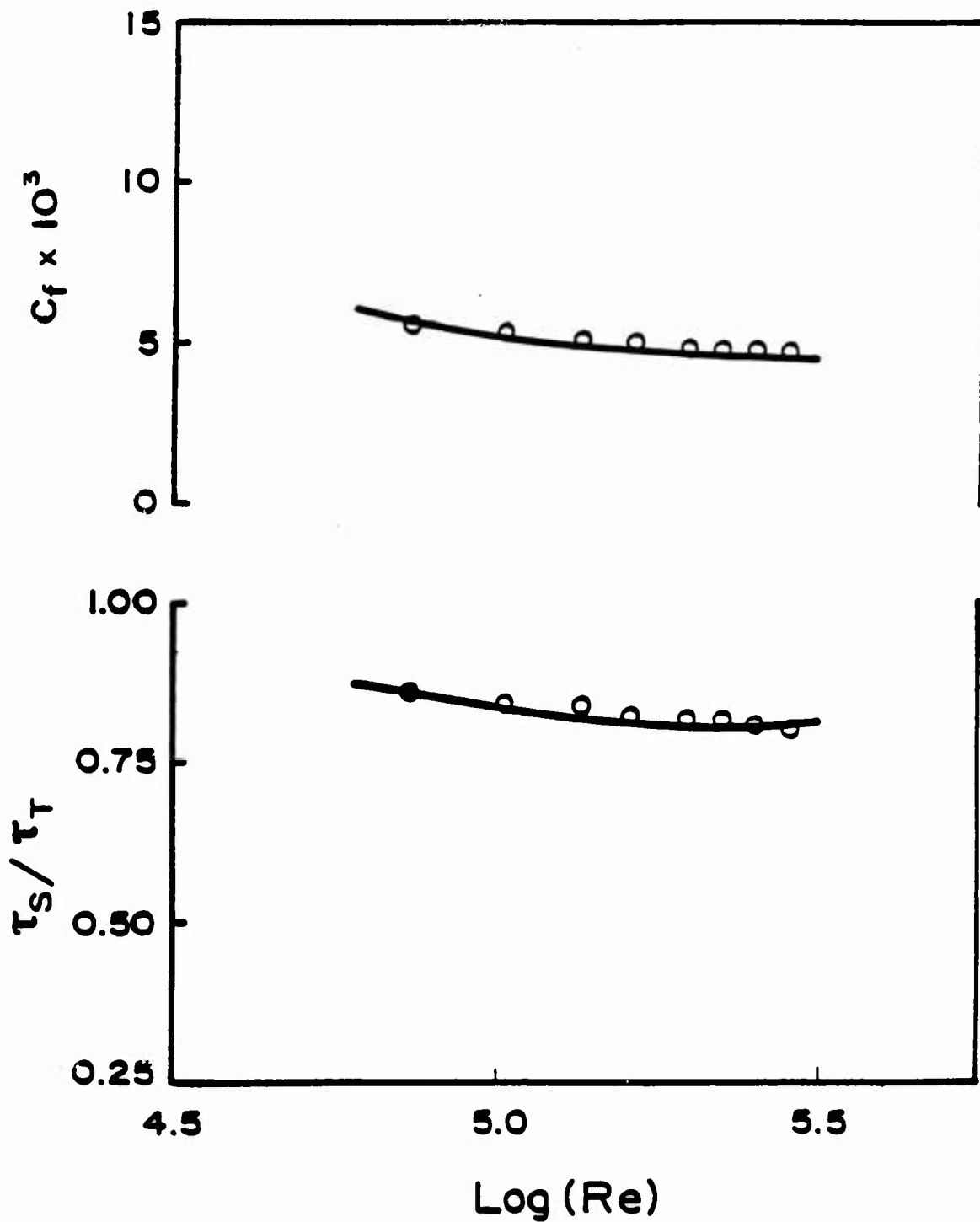


Figure 22. Comparison of Calculations with the Data of Chen;
 $\ell/k = 18.5$

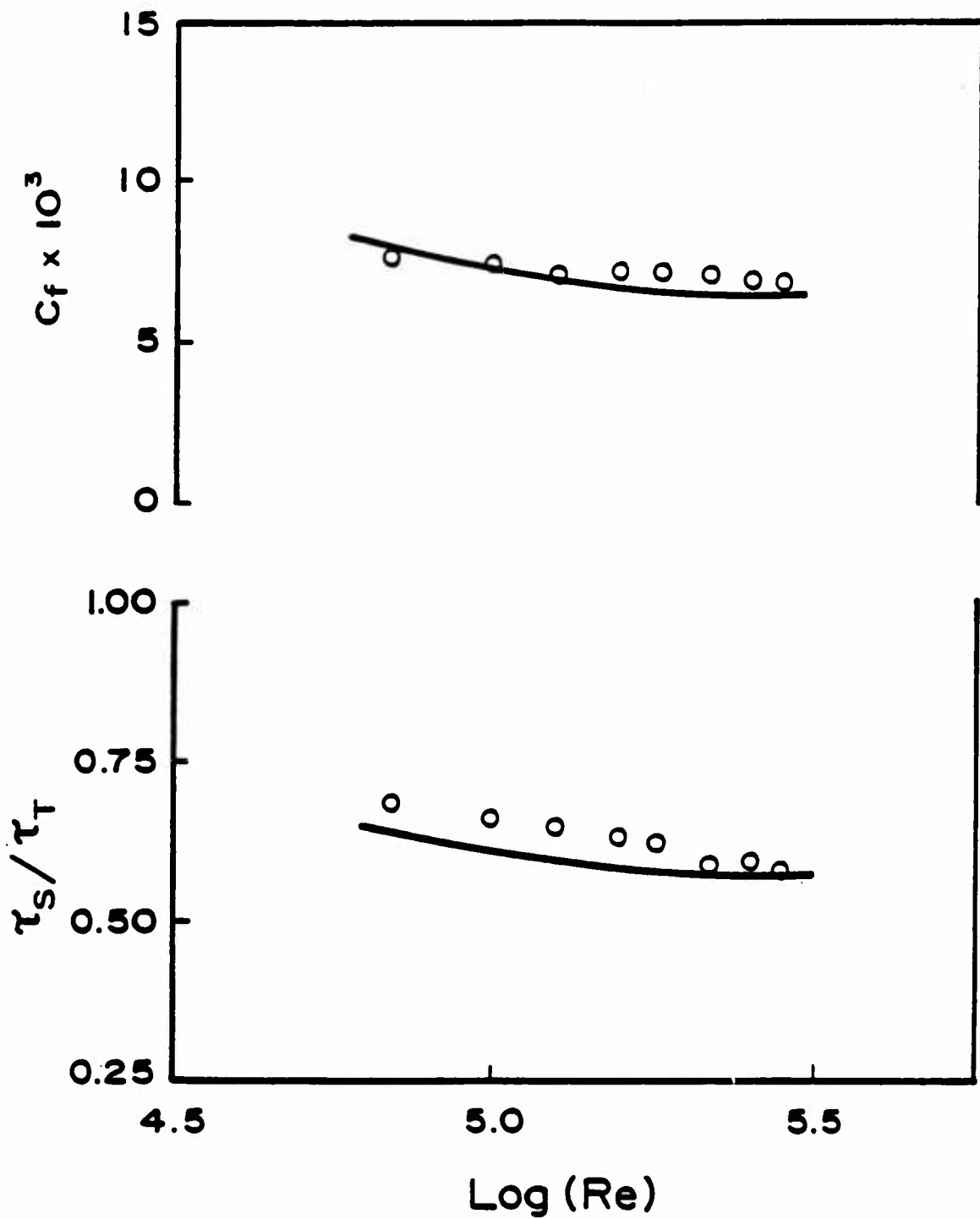


Figure 23. Comparison of Calculations with the Data of Chen; $l/k = 10.7$

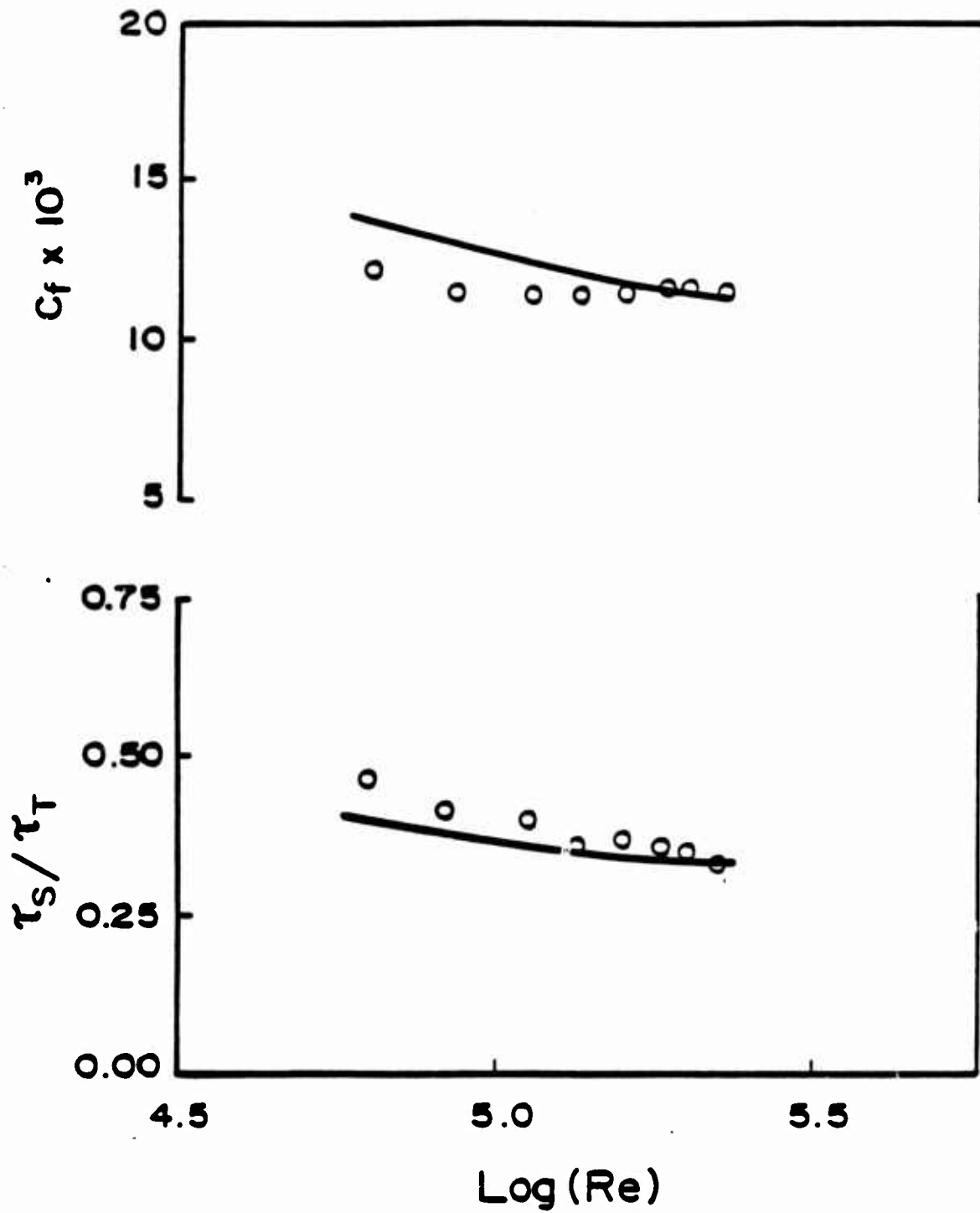


Figure 24. Comparison of Calculations with the Data of Chen; $l/k = 6.4$

comes from a disagreement in average velocity and not from the calculated shear stress, τ_w . In Figure 24, it is seen that the greatest disagreement occurs at the first two points. Chen did report the maximum velocity for the first point ($Re = 60,000$). If the maximum velocity is used to normalize both the calculated and measured τ_w , the predicted value is $C_f = 7.31 \times 10^{-3}$ and the measured value is 7.28×10^{-3} .

The comparisons of the relative contribution of viscous shear forces between the elements and the drag on the elements are of particular interest. One of the major advantages of the discrete element model is that these two forces and their interactions are accounted for in the model. Inspection of Figures 22 - 24 reveals good agreement between the predictions and data for τ_s/τ_T . The maximum disagreement is about 12% and the preponderance of the points agree within 5%. This agreement indicates that the present discrete element model correctly incorporates much of the physics of the interaction between the roughness elements and the flow.

Chen reported uncertainty values of approximately $\pm 1\%$ for the data presented in Figures 22 - 24. This small reported uncertainty is approximately represented by the size of the data point symbols in the figures.

SECTION VII

BOUNDARY-LAYER FLOW RESULTS

The discrete element model has been applied to three of the boundary layer experiments performed at Stanford University. Two of the experiments (Healzer [32] and Pimenta [4]) reported skin friction coefficients and Stanton numbers for both transitionally and fully rough zero pressure gradient flow over a constant temperature rough surface. The third (Coleman [5]) included free stream pressure gradients and variable wall temperature.

1. DESCRIPTION OF THE STANFORD EXPERIMENTS

The Stanford "Roughness Rig" consists of a closed loop wind tunnel with air at ambient conditions as the working fluid. Free stream velocities from 9.8 m/sec to 73.8 m/sec were obtained. This experimental set up is discussed in detail by Healzer [32]. The test surface consists of 24 0.10-meter (in the flow direction) plates constructed with 1.27-mm-diameter spheres. The surface was built up of eleven tiers of spheres packed in the most dense array. Each plate was maintained at a constant temperature by individually controlled heating elements.

Stanton numbers were obtained from an energy balance on each of the plates. The uncertainty of the Stanton number measurements was stated to be $\pm 0.1 \times 10^{-3}$ Stanton number units by all three workers. One worker, Healzer [32], determined the skin friction coefficient, C_f , by differentiating the measured momentum thickness distribution; he did not report uncertainty values. The other workers, Pimenta [4] and Coleman [5], determined C_f from measured Reynolds stresses and mean velocity profiles with a reported uncertainty of $\pm 10\%$.

One of the concerns of the Stanford series of experiments was the study of the effects of surface transpiration; therefore, both blown and unblown runs were reported. Since transpiration is not considered in the present work, only the unblown cases are considered here.

2. APPLICATION OF THE DISCRETE ELEMENT MODEL

The present calculations were made using an incompressible, constant property, discrete element boundary layer code. This more economical code was selected over the compressible, variable property code because

the relatively low velocity and small temperature difference conditions of the Stanford experiments satisfy the incompressible and constant property assumptions. Furthermore, the Stanford data reduction was made based on these assumptions.

The roughness element drag coefficient model and Nusselt number model used are those as calibrated in Section V. It should be noted in review that the C_D model was calibrated based on Schlichting's [3] channel flow data and the Nusselt number model was calibrated based on one of the Stanford runs (Pimenta [4], $U_e = 27$ m/sec). Therefore, the skin friction calculations presented here are true predictions. While the Nusselt number model was calibrated based on one run on the Stanford surface, its extrapolation to independent measurements under widely varying conditions is considered to be a significant test.

The turbulence model used is the mixing length and constant turbulent Prandtl number model discussed in Section III. Some of the Stanford runs were allowed to transition naturally from laminar to turbulent flow. For these cases the transition point was specified in the code, with that point selected based on inspection of the Stanton number data. For these cases a transition zone with a length equal to the laminar zone was assumed and an intermittency factor was employed in the eddy viscosity calculation. Some of the Stanford runs were tripped turbulent by use of a boundary layer trip. In these cases turbulent flow was assumed from the leading edge. Virtual origins were not employed.

As stated previously, the Stanford surface consisted of spheres arranged in the most densely packed array. Therefore, the effective base wall location, as determined in Section V using Schlichting's data for most densely packed spheres, was used.

In the present calculations, the roughness elements and the surrounding smooth regions were taken to be at the same temperature, i.e., $T_R = T_w$.

3. COMPARISONS WITH THE DATA OF HEALZER AND PIMENTA

From the point of view of the present work, Healzer's [32] and Pimenta's [4] experiments are very similar. Both workers had a constant free stream velocity and a constant wall temperature. Therefore, they are considered together. The discrete element model has been applied to these experiments, and the skin friction, C_f , and Stanton number, St ,

comparisons are discussed below. Also, mean velocity, mean temperature, turbulent shear stress, and turbulent heat flux profile comparisons are made for one case (Pimenta's 27 m/sec).

Figures 25 and 26 show comparisons between the calculated and measured values of C_f and St for the two transitionally rough cases (Healzer's $U_e = 9.9$ m/sec and Pimenta's $U_e = 15.8$ m/sec). The bars on the data points show a $\pm 10\%$ span for C_f and the stated uncertainty range for the Stanton numbers (± 0.001 St units). Inspection of the figures reveals that the agreement is very good; the predictions are almost everywhere within the data uncertainty.

Figures 27 - 30 show comparisons for the fully rough cases (Pimenta's $U_e = 27$ m/sec and 39.6 m/sec and Healzer's $U_e = 57.9$ m/sec and 73.8 m/sec). Inspection of the figures reveals that the agreement is excellent. Again the predictions are almost everywhere within the experimental uncertainty.

Figures 31 and 32 show comparisons between predicted and measured velocity and temperature profiles. Inspection of the figures reveals that the agreement is very good. This agreement is not unexpected since such good agreement has been demonstrated for the surface measurables, C_f and St . However, it should be pointed out that erroneously calibrated discrete element models can yield apparently good surface measurable agreement while at the same time giving poor boundary layer profile agreement.

Figures 33 and 34 show comparisons of measured and predicted nondimensional Reynolds shear stress and turbulent heat flux for Pimenta's $U_e = 27$ m/sec run. Inspection of the figures reveals that the agreement is excellent. Such agreement bolsters confidence in the modeling used in making the predictions.

4. COMPARISONS WITH THE DATA OF COLEMAN

Coleman [5] ran experiments on the same apparatus as Pimenta and Healzer with an accelerated free stream (favorable pressure gradient) and/or variable wall temperatures. His accelerated flows consisted of three equilibrium runs (characterized by constant values of C_f within the equilibrium zone) and one nonequilibrium run. His variable wall temperature cases consisted of step functions, linear variations, and one

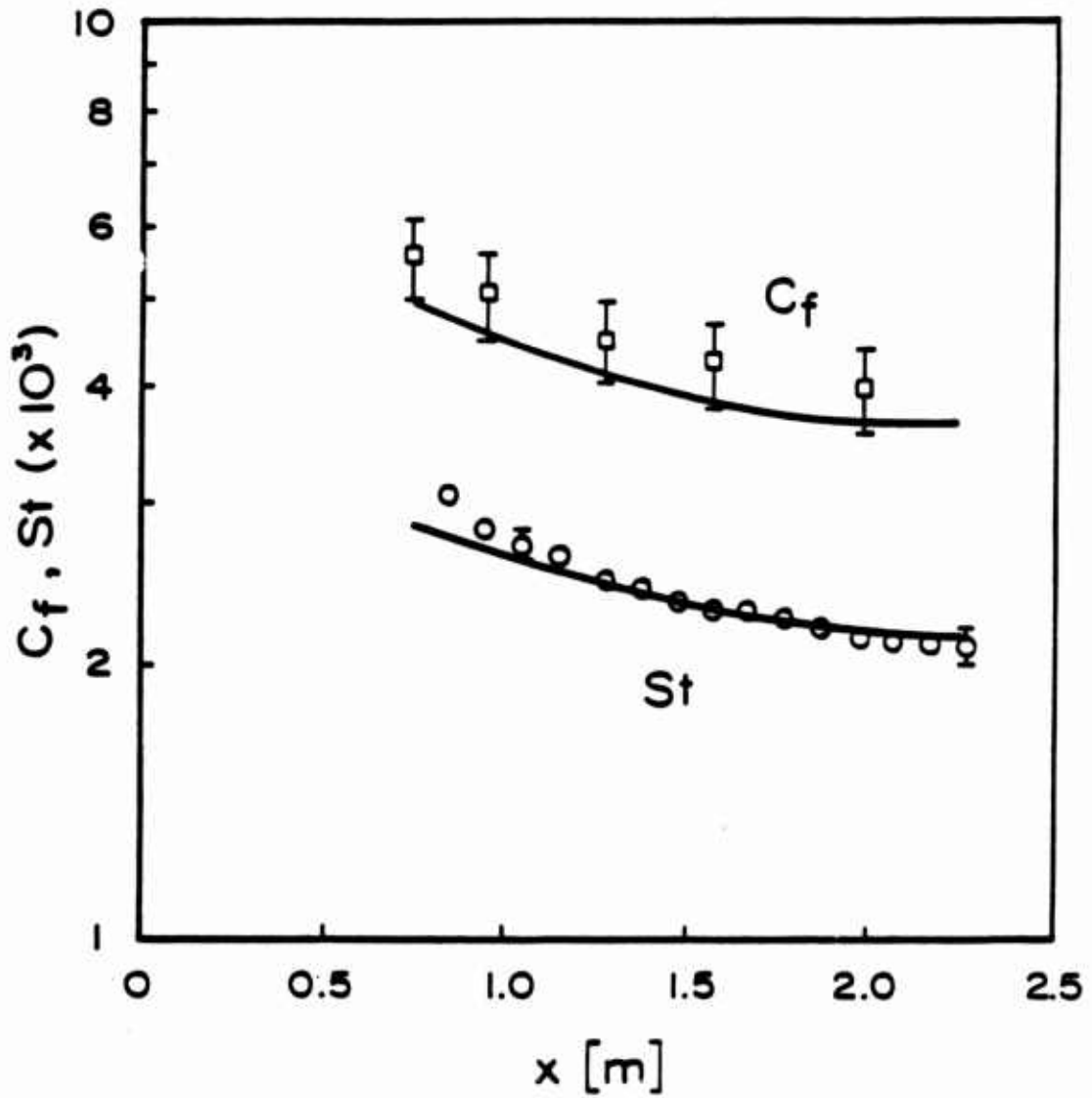


Figure 25. Comparison of Calculations with the Data of Healy; $U_e = 9.75$ m/s

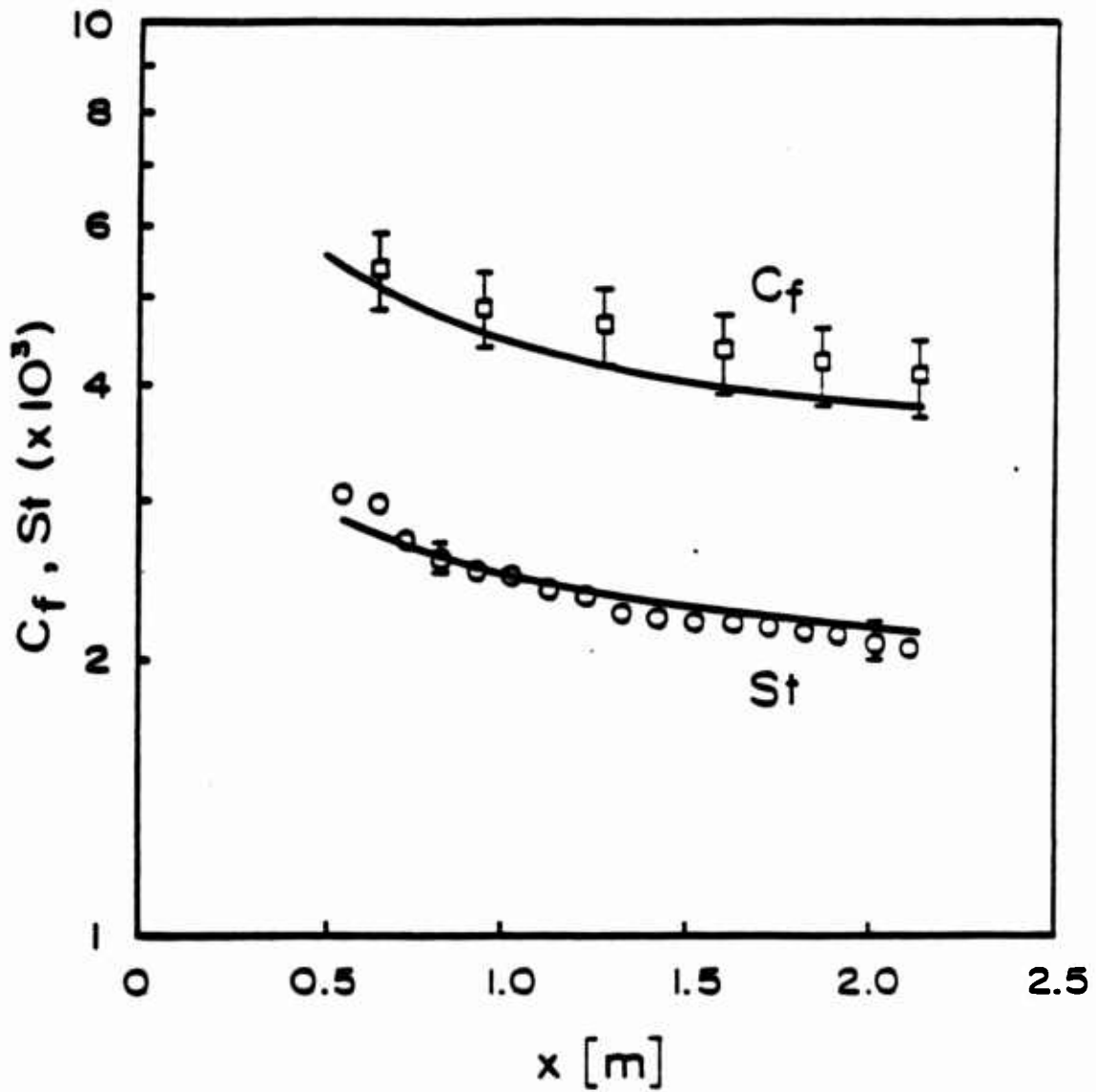


Figure 26. Comparison of Calculations with the Data of Pimenta; $U_e = 15.8$ m/s

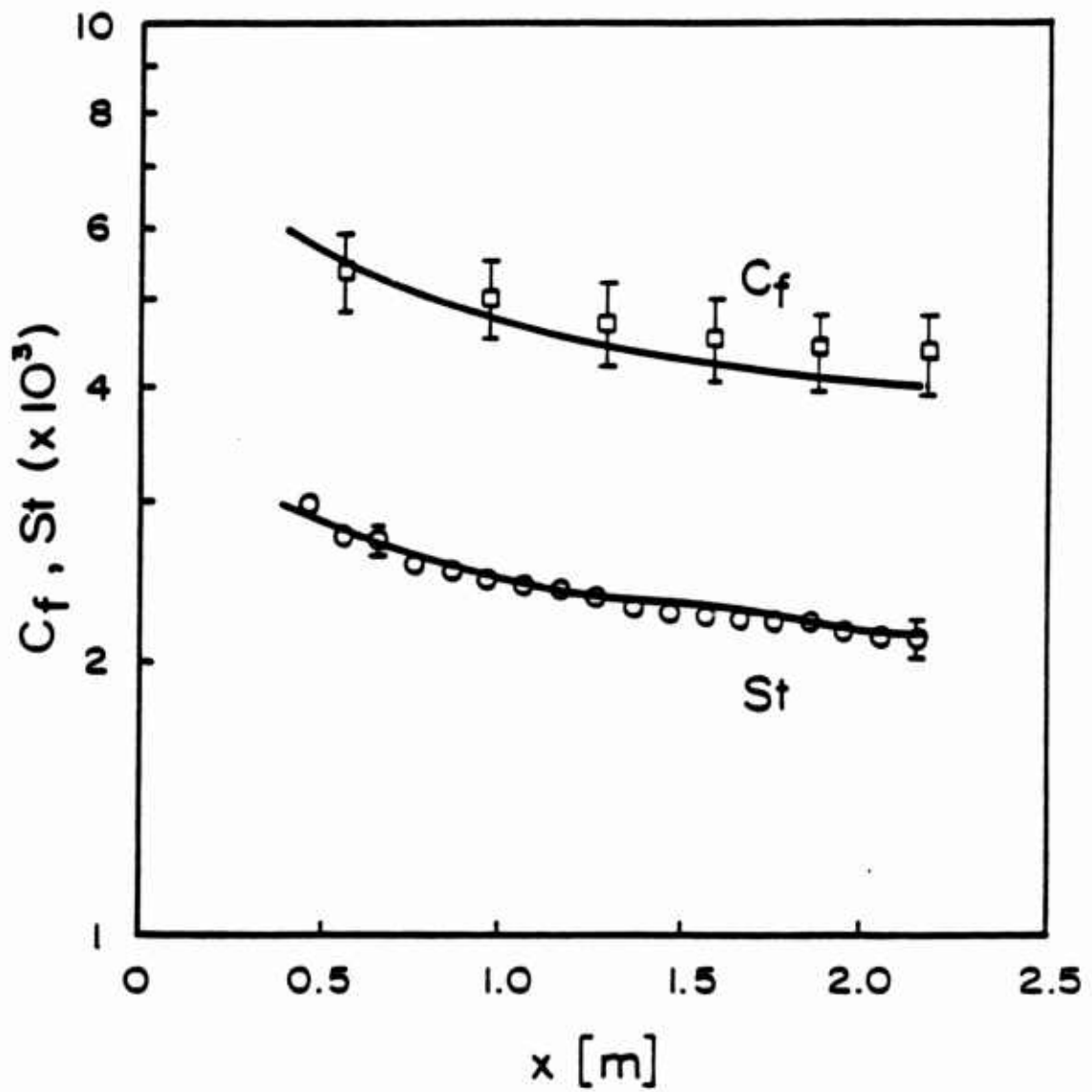


Figure 27. Comparison of Calculations with the Data of Pimenta; $U_e = 27$ m/s

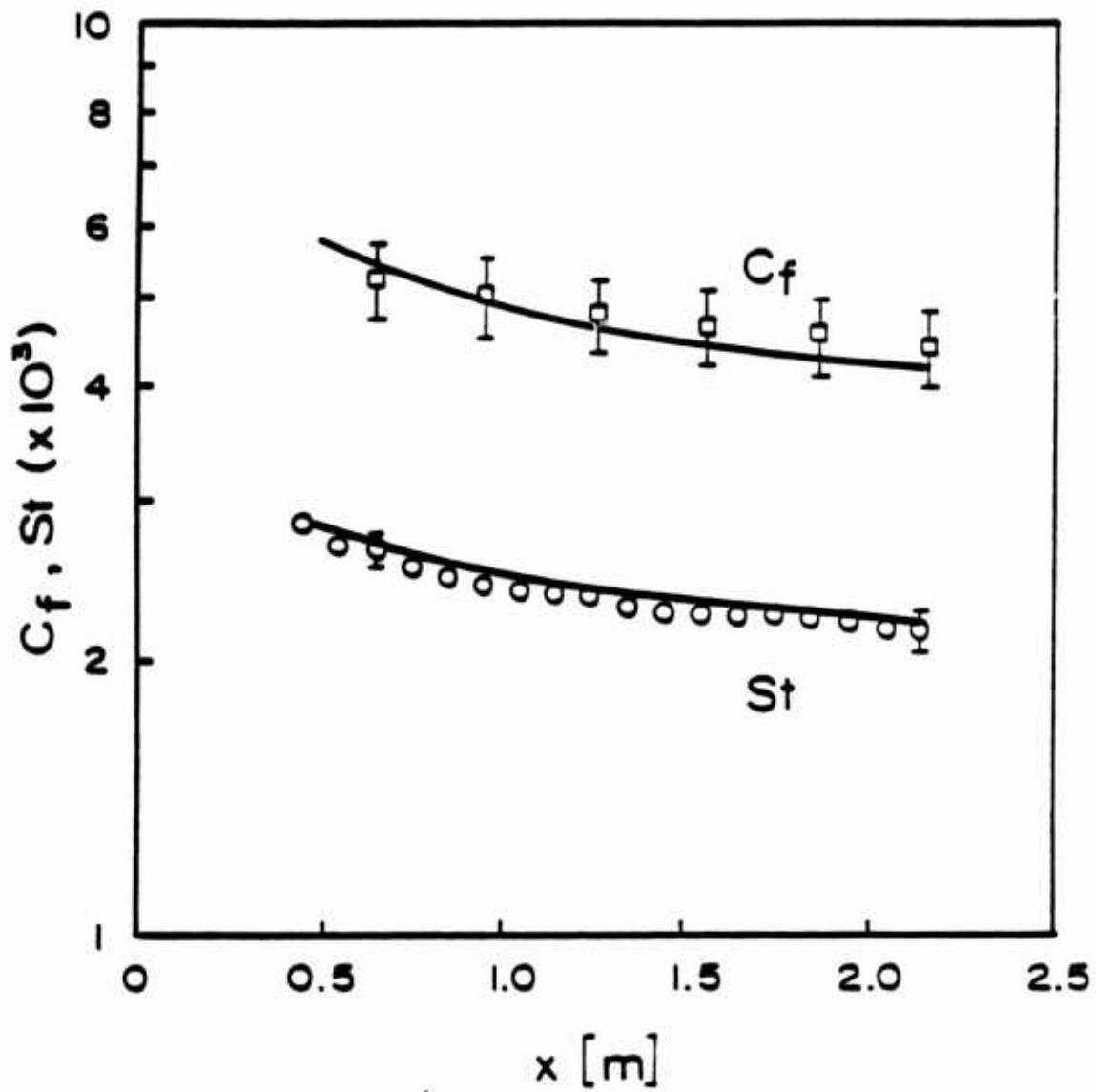


Figure 28. Comparison of Calculations with the Data of Pimenta; $U_e = 39.6$ m/s

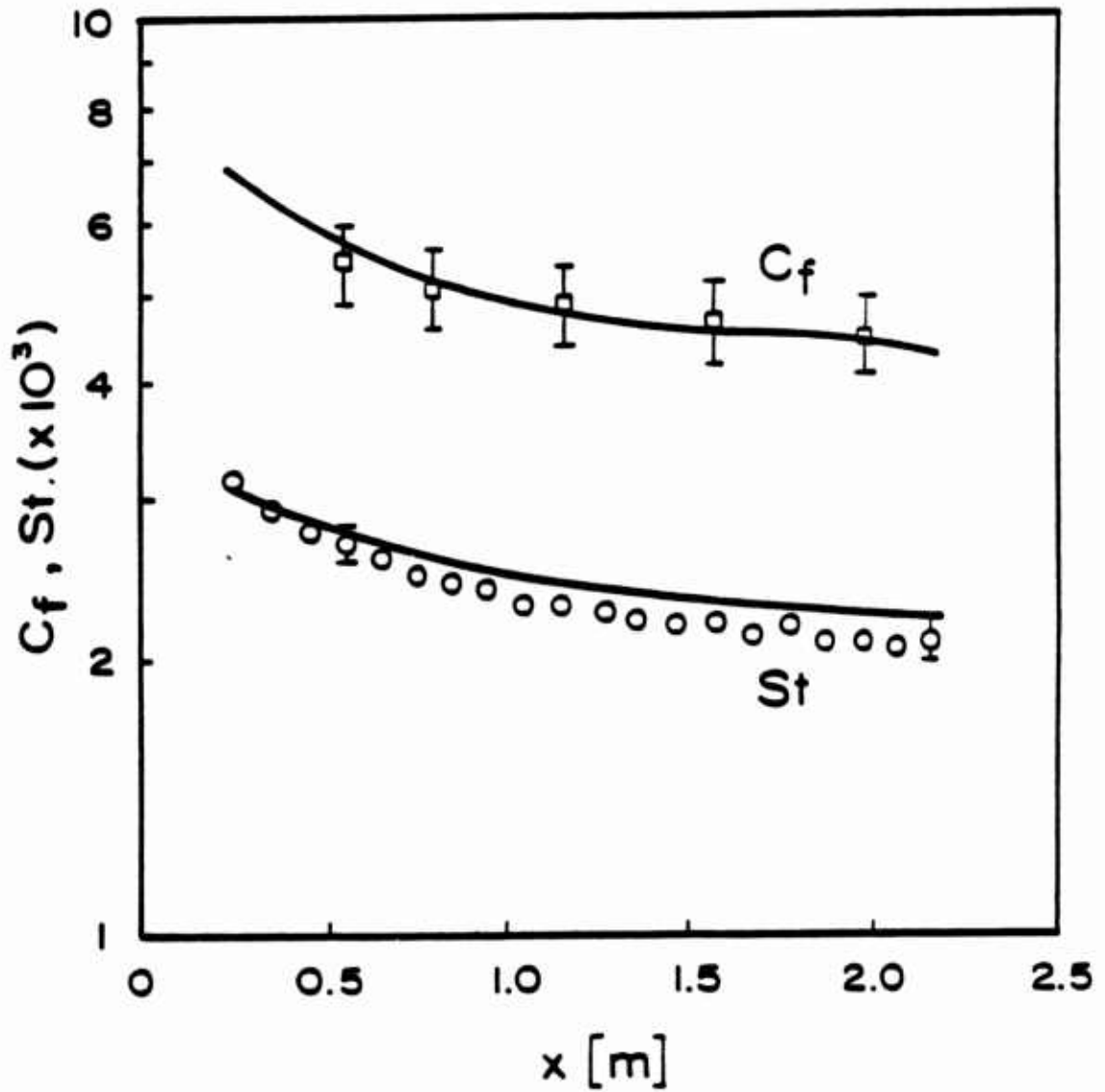


Figure 29. Comparison of Calculations with the Data of Healzer; $U_e = 58$ m/s

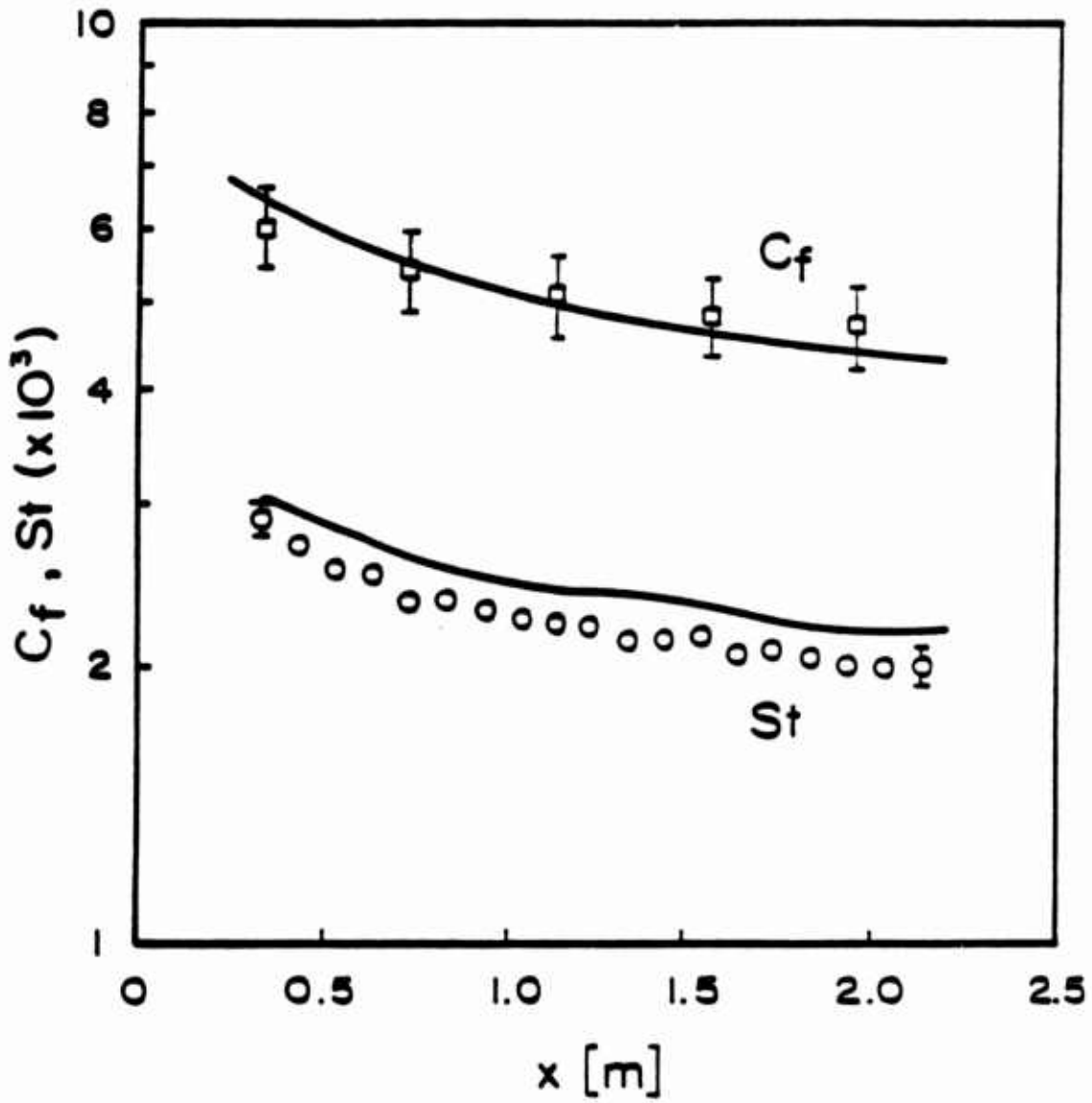


Figure 30. Comparison of Calculations with the Data of Healzer; $U_e = 74$ m/s

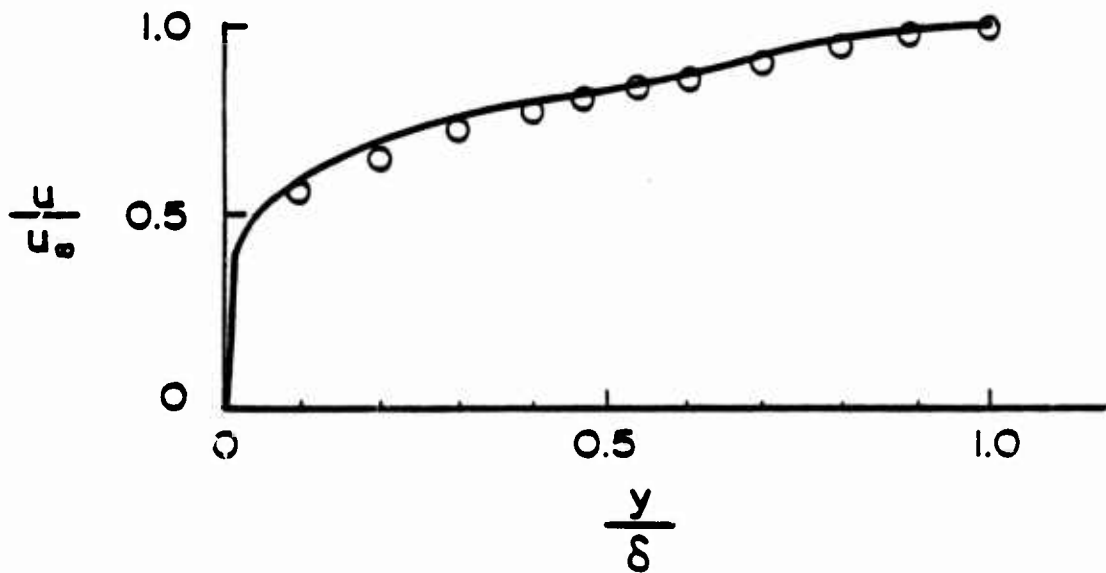


Figure 31. Typical Comparison of Calculated and Measured Velocity Profiles; Pimenta $U_e = 27$ m/s

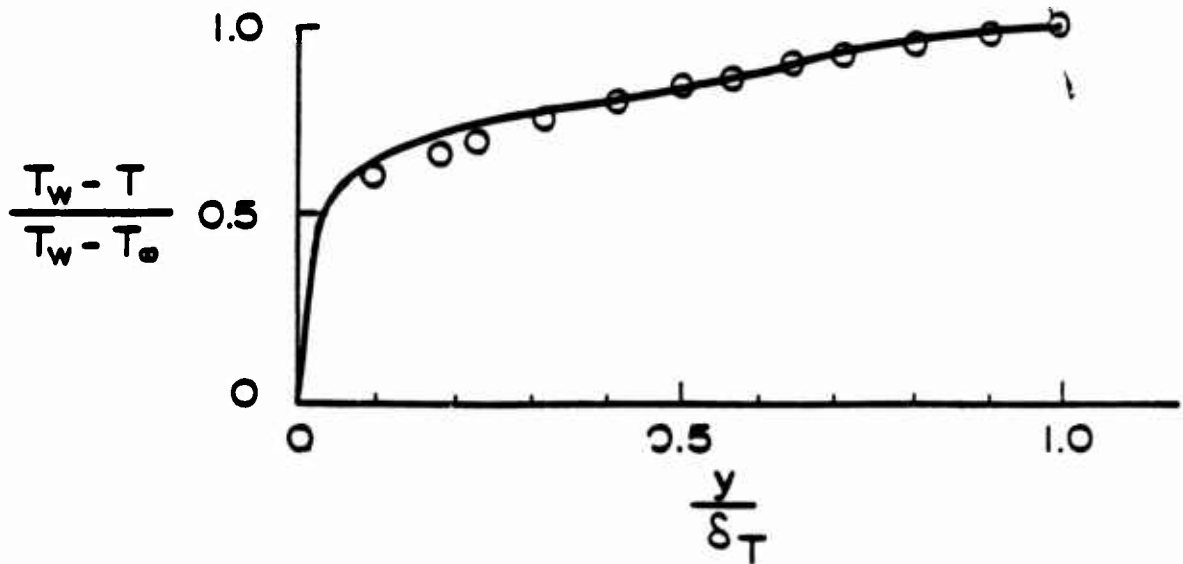


Figure 32. Typical Comparison of Calculated and Measured Temperature Profiles; Pimenta $U_e = 27$ m/s

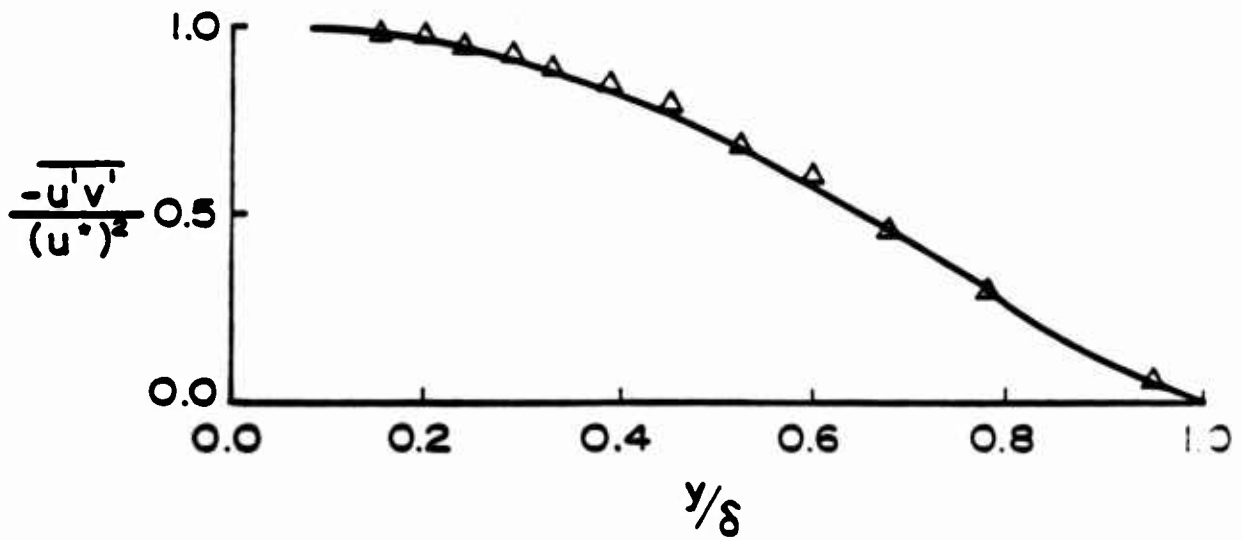


Figure 33. Typical Comparison of Calculated and Measured Reynolds Stress; Pimenta $U_e = 27$ m/s

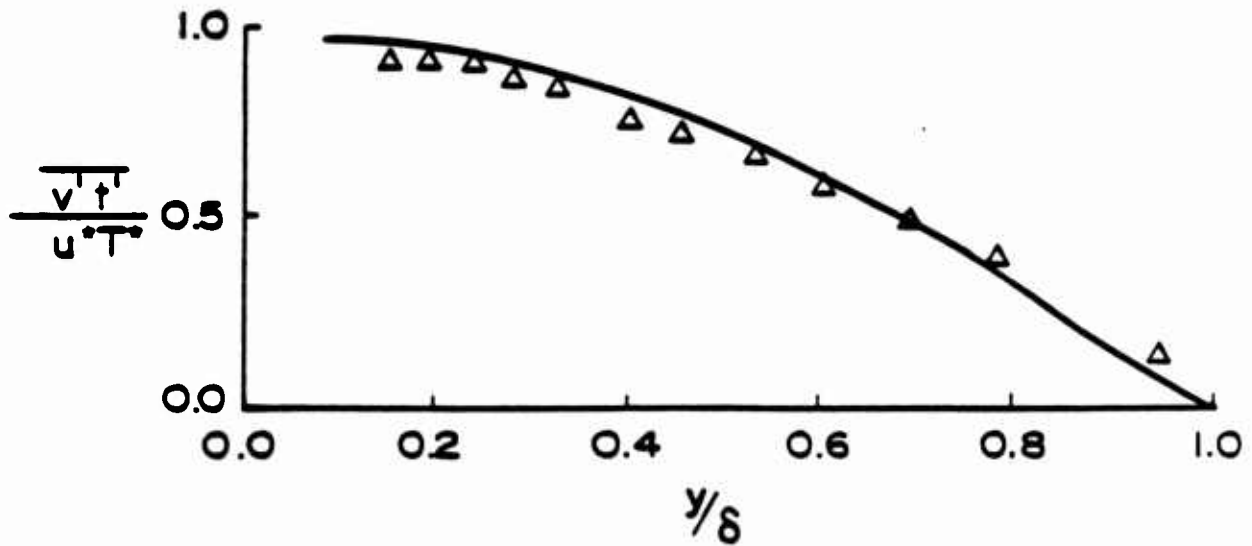


Figure 34. Typical Comparison of Calculated and Measured Turbulent Heat Flux; Pimenta $U_e = 27$ m/s

bi-linear variation. Comparisons with these data are presented below.

Figure 35 shows the edge velocity variation for the three equilibrium runs. To obtain the pressure variation, dU_e/dx , term required to solve the boundary layer equations, these data were fit with piecewise linear functions using the least squares method. Figures 36 - 38 show the comparisons of the skin friction and Stanton number predictions for these flows with the data for the constant wall temperature cases. Inspection of the figures reveals excellent agreement. The predictions are almost everywhere within the data uncertainty. Figure 39 shows the Stanton number comparison for the same case as Figure 35(a) and 36 with step change in wall temperature where the first six plates (0.61 m) were unheated. Inspection of the figure reveals very good agreement.

Figure 40 shows the edge velocity variation for the nonequilibrium run. Again a least-square curve fit was used to determine dU_e/dx in the accelerated region. Figure 41 shows the comparison of predictions and data for this case with a constant wall temperature. Inspection of the figure reveals that the agreement is again excellent. Figure 42 shows the Stanton number comparison for this case with the first six plates unheated. From this figure it is seen that the agreement is good.

The last two cases used for comparison are the one with a linear wall temperature variation and the one with a bi-linear wall temperature variation. Figures 43(a) and 43(b) show the x-variation of the wall temperature for these two cases. Both of these cases had a constant free stream velocity (zero pressure gradient). Figures 44 and 45, respectively, show the Stanton number comparisons for these two cases. Inspection of the figures reveals that the agreement is excellent.

Figure 46 shows a comparison of the nondimensional shear stress, $-\overline{u'v'}$, for one of Coleman's equilibrium runs ($K_T = 0.29 \times 10^{-3}$). Inspection of the figure reveals that the agreement is reasonable, with the trend predicted correctly but with the predicted magnitudes being slightly high.

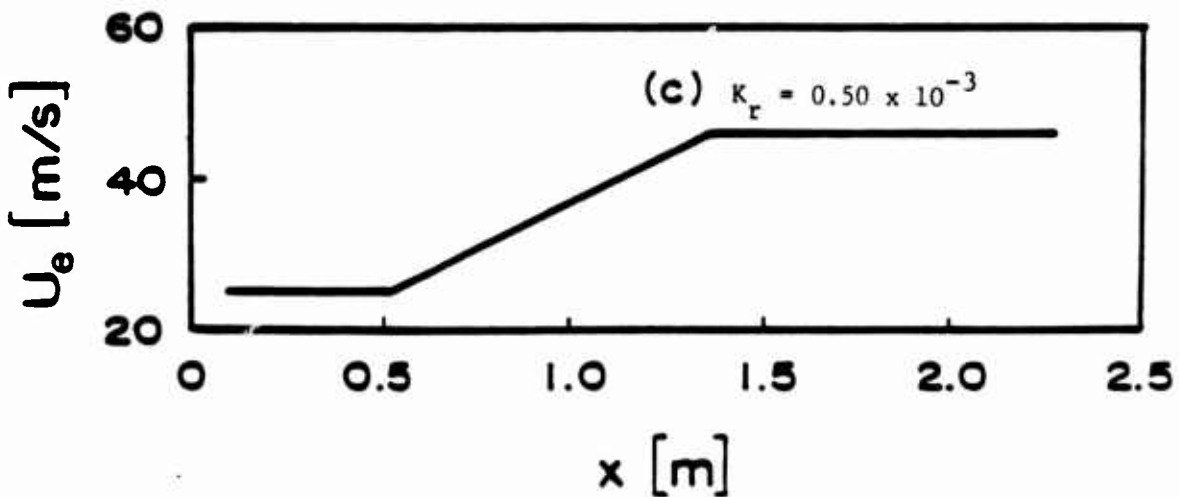
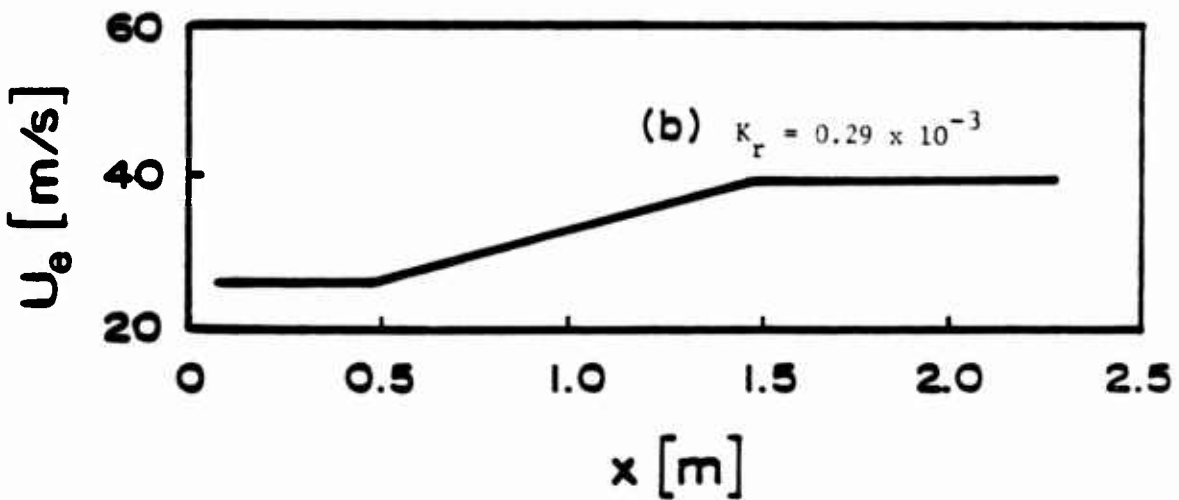
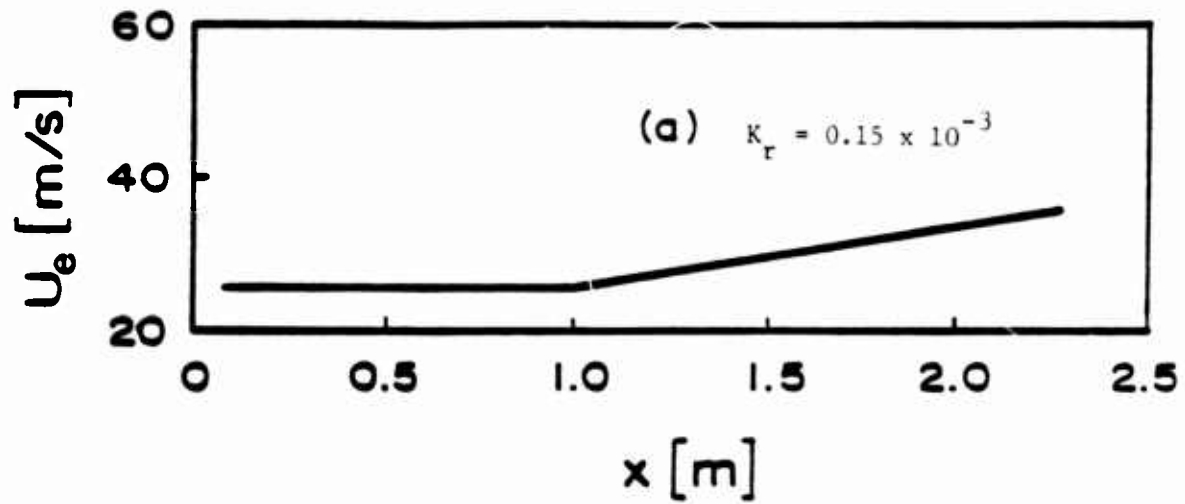


Figure 35. Edge Velocity Distributions for Coleman's Equilibrium Pressure Gradient Runs

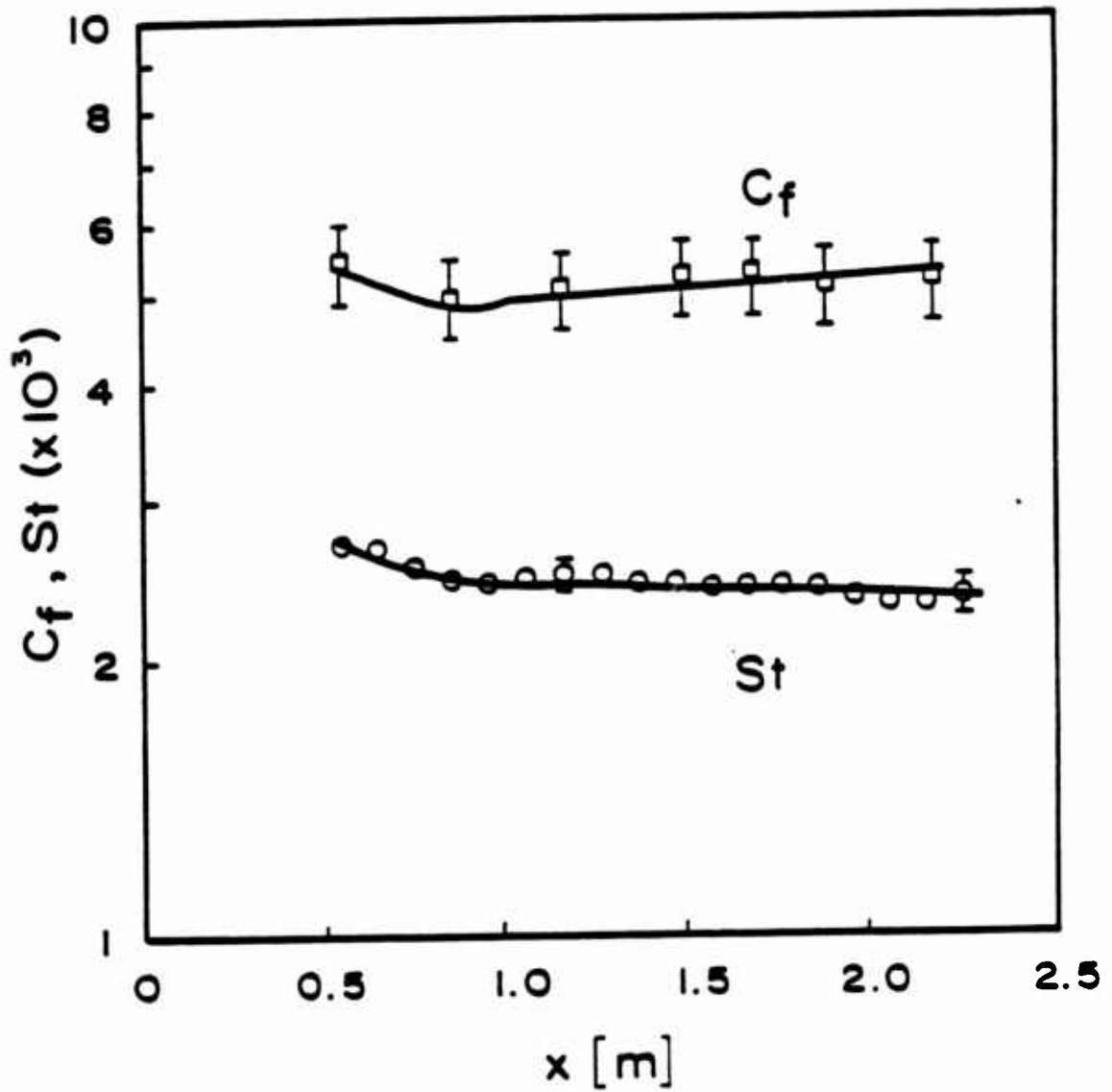


Figure 36. Comparison of Calculations with the Data of Coleman; $K_T = 0.15 \times 10^{-3}$; Constant Wall Temperature

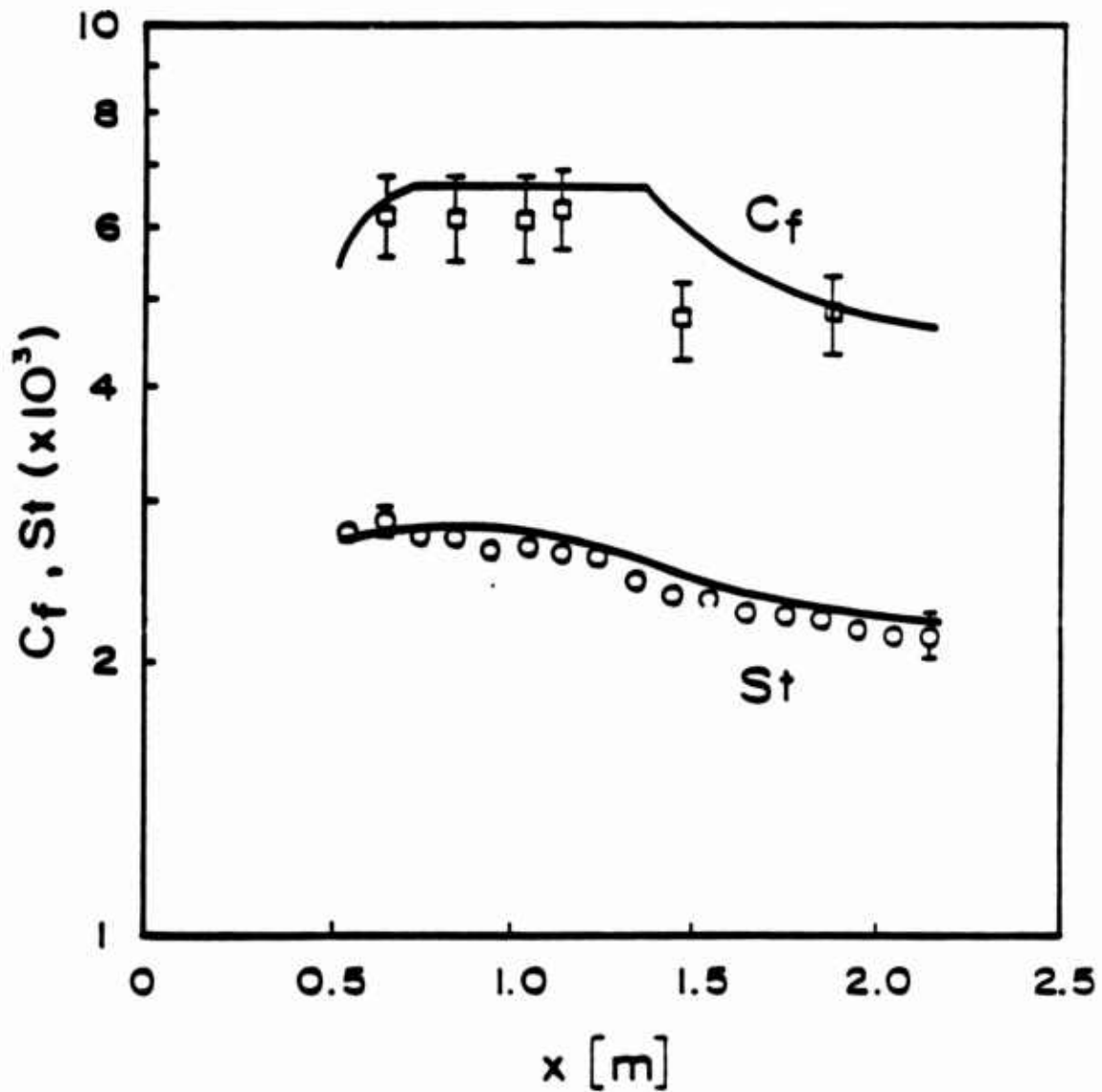


Figure 37. Comparison of Calculations with the Data of Coleman; $K_r = 0.29 \times 10^{-3}$; Constant Wall Temperature

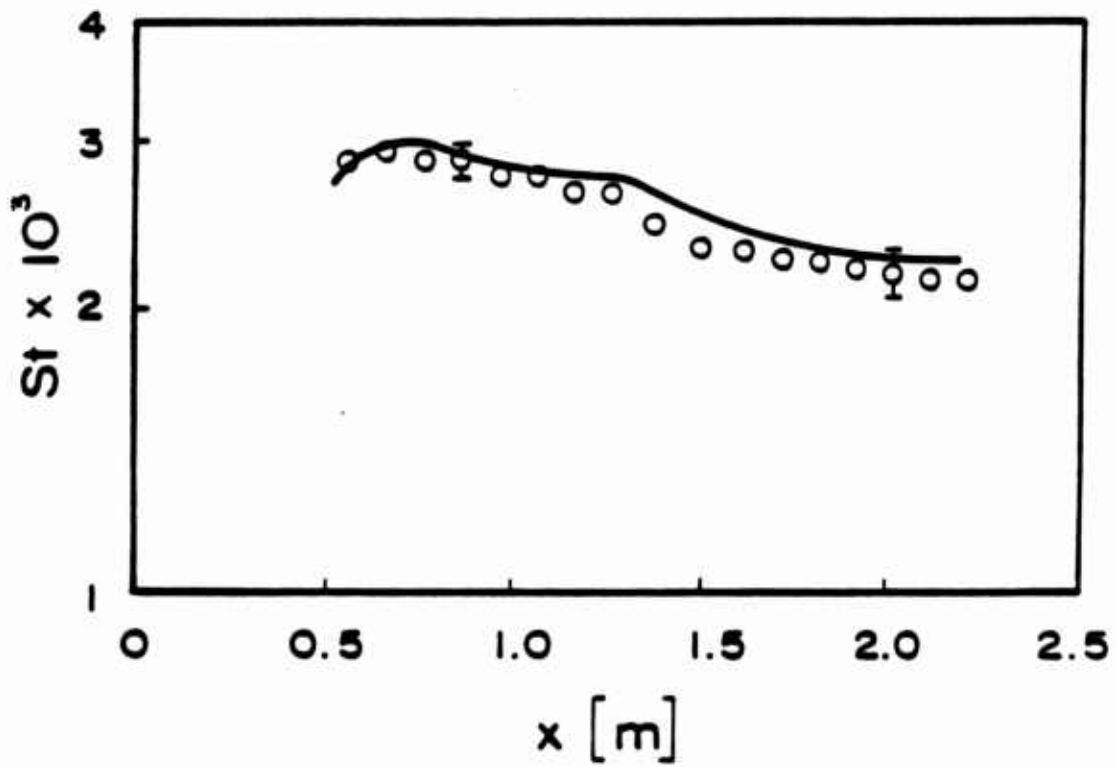


Figure 38. Comparison of Calculations with the Data of Coleman; $K_T = 0.5 \times 10^{-3}$; Constant Wall Temperature

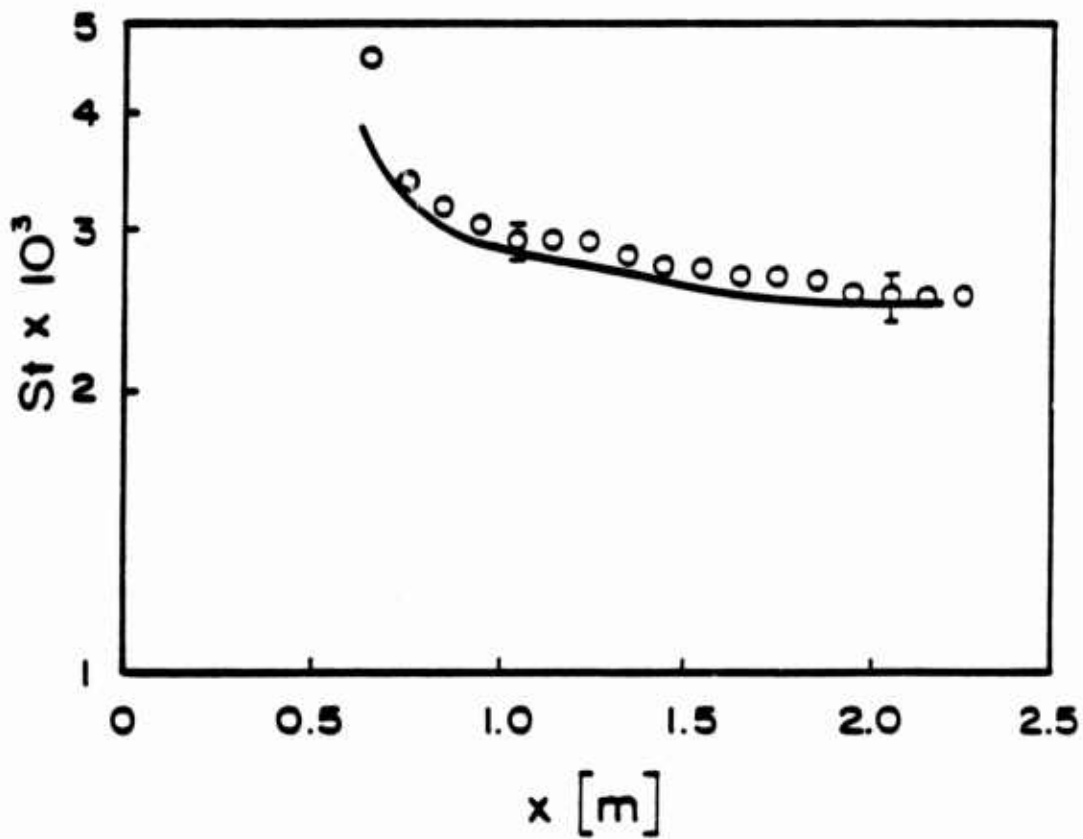


Figure 39. Comparison of Calculations with the Data of Coleman; $k_r = 0.15 \times 10^{-3}$; First Six Plates Unheated

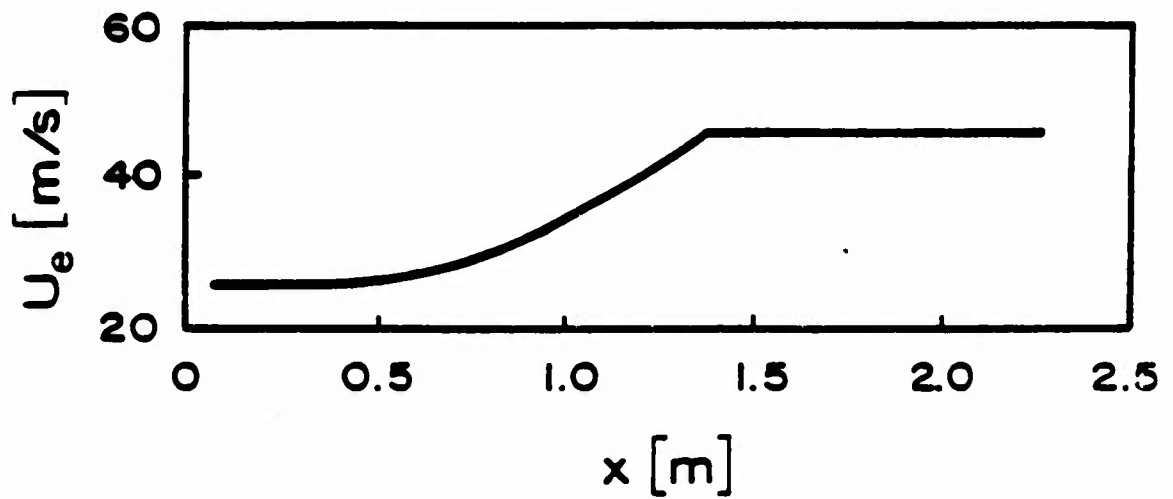


Figure 40. Edge Velocity Distribution for Coleman's Non-equilibrium Pressure Gradient Run; $K = 0.28 \times 10^{-6}$

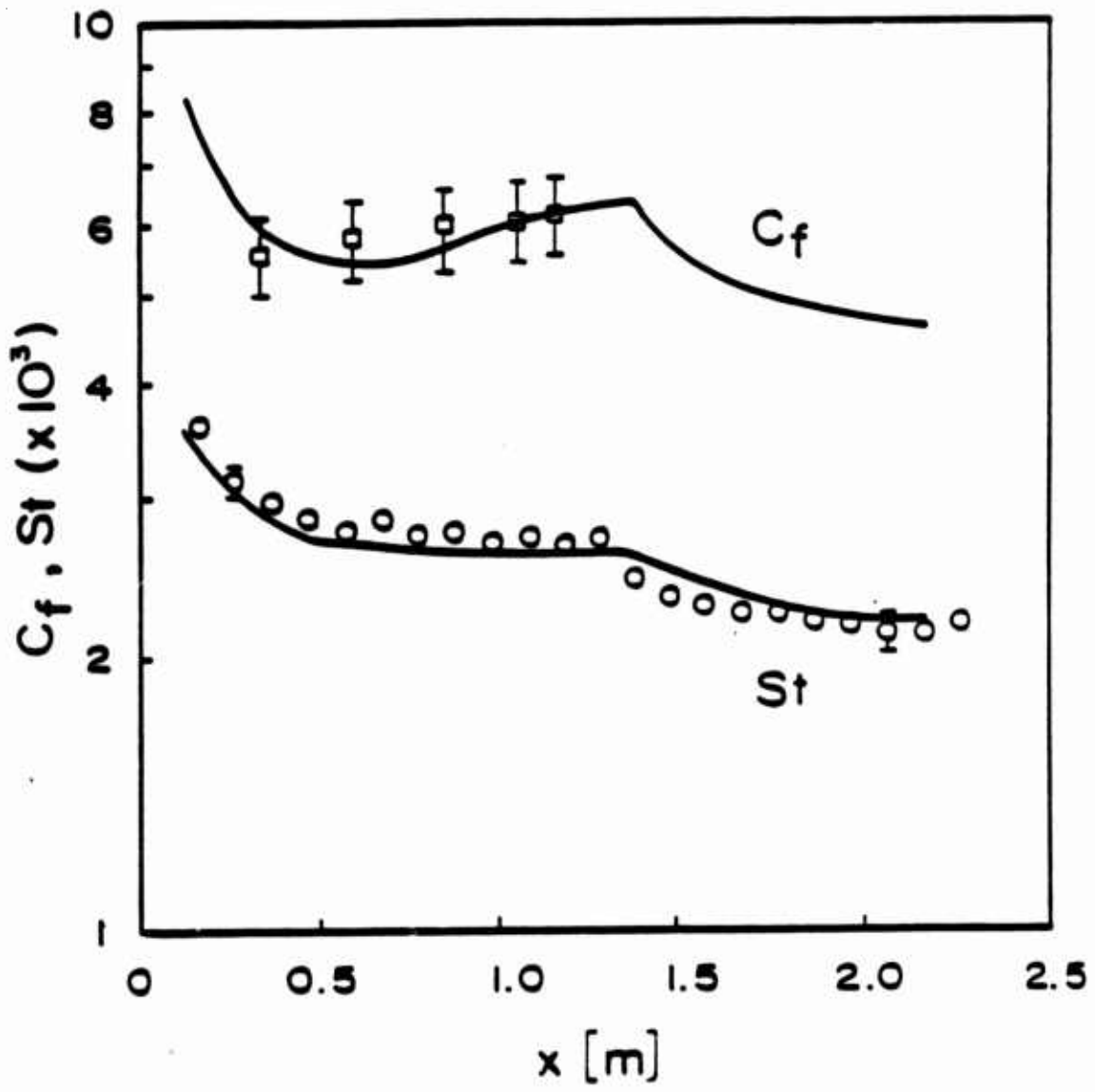


Figure 41. Comparison of Calculations with the Data of Coleman; Nonequilibrium Run; Constant Wall Temperature

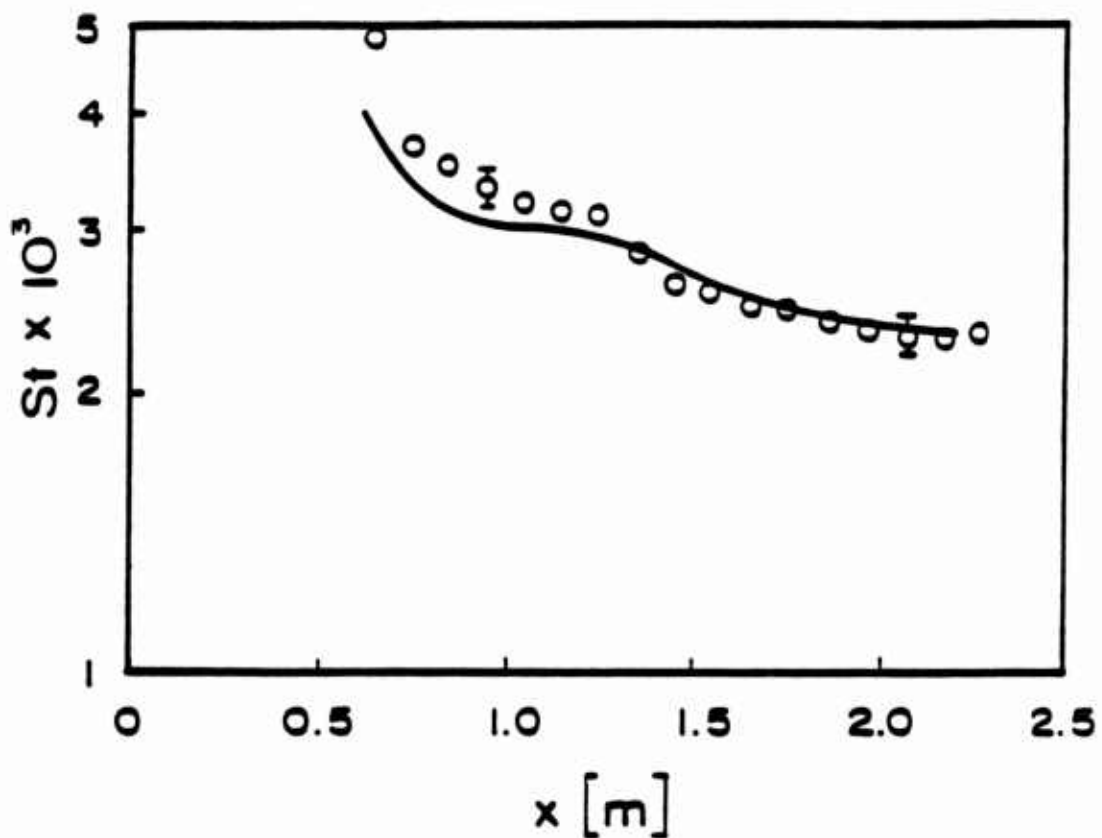


Figure 42. Comparison of Calculations with the Data of Coleman; Nonequilibrium Run; First Six Plates Unheated

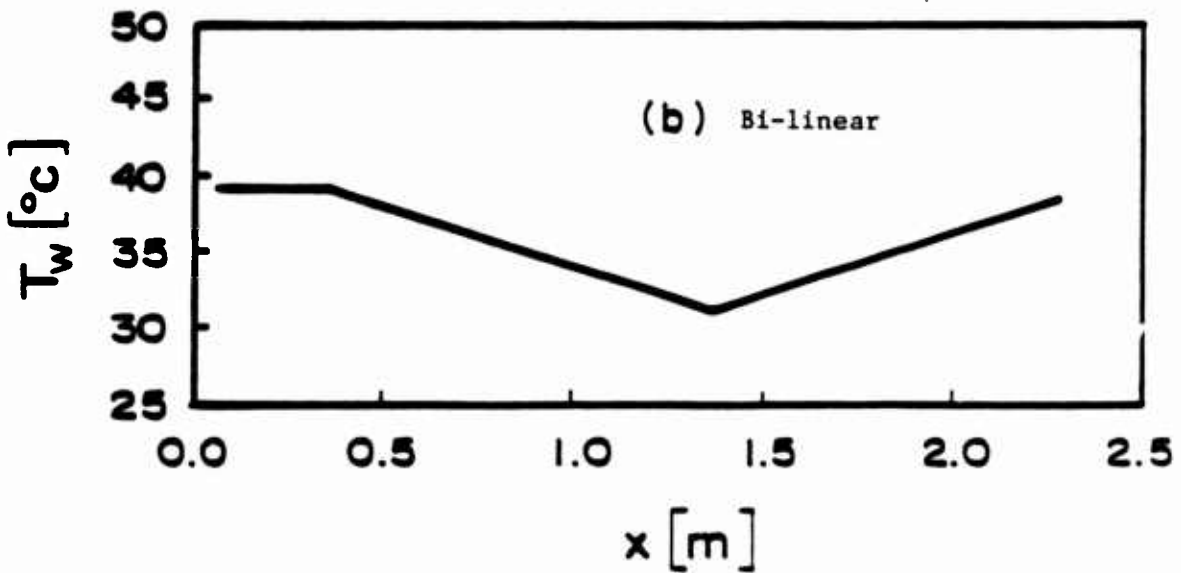
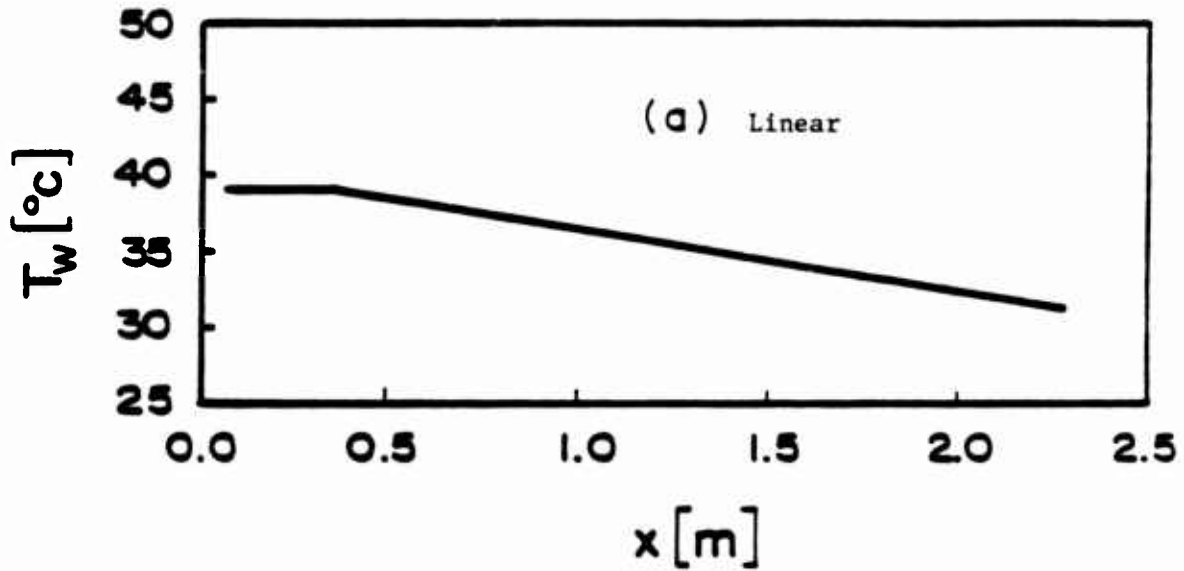


Figure 43. Wall Temperature Distribution for the Data of Coleman; Both Cases with Zero Pressure Gradient

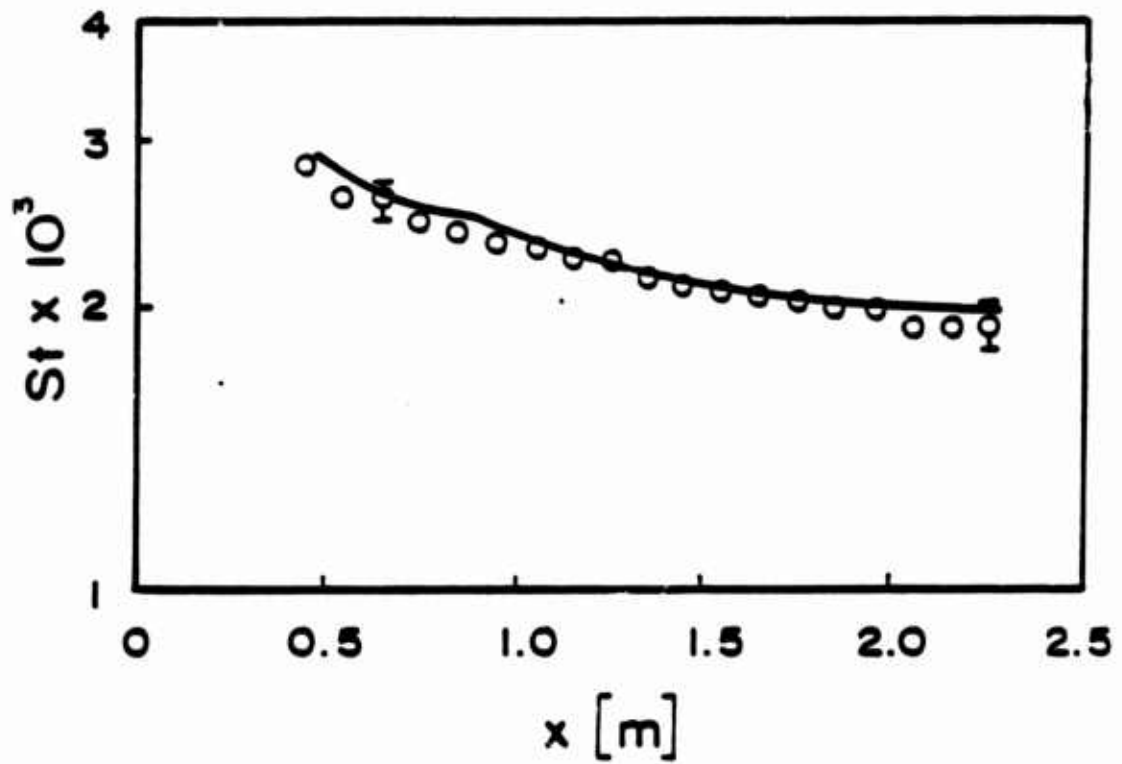


Figure 44. Comparison of Calculations with the Data of Coleman; Linear Wall Temperature Distribution

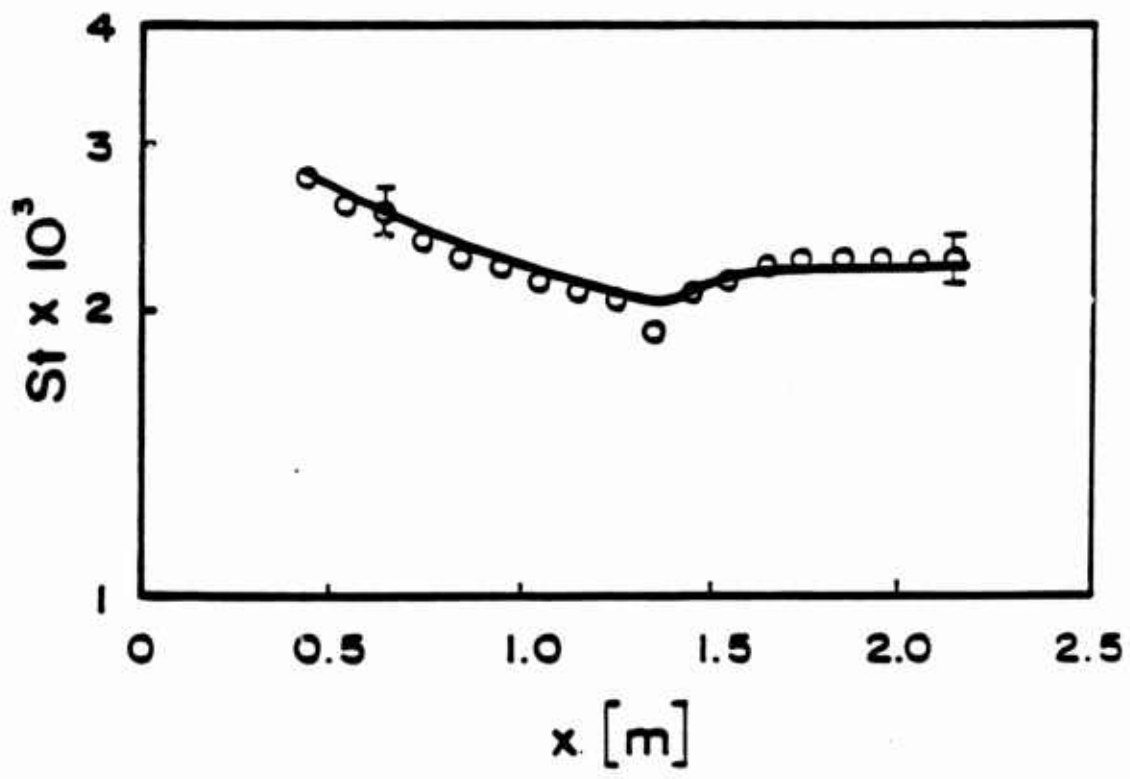


Figure 45. Comparison of Calculations with the Data of Coleman; Bi-linear Wall Temperature Distribution

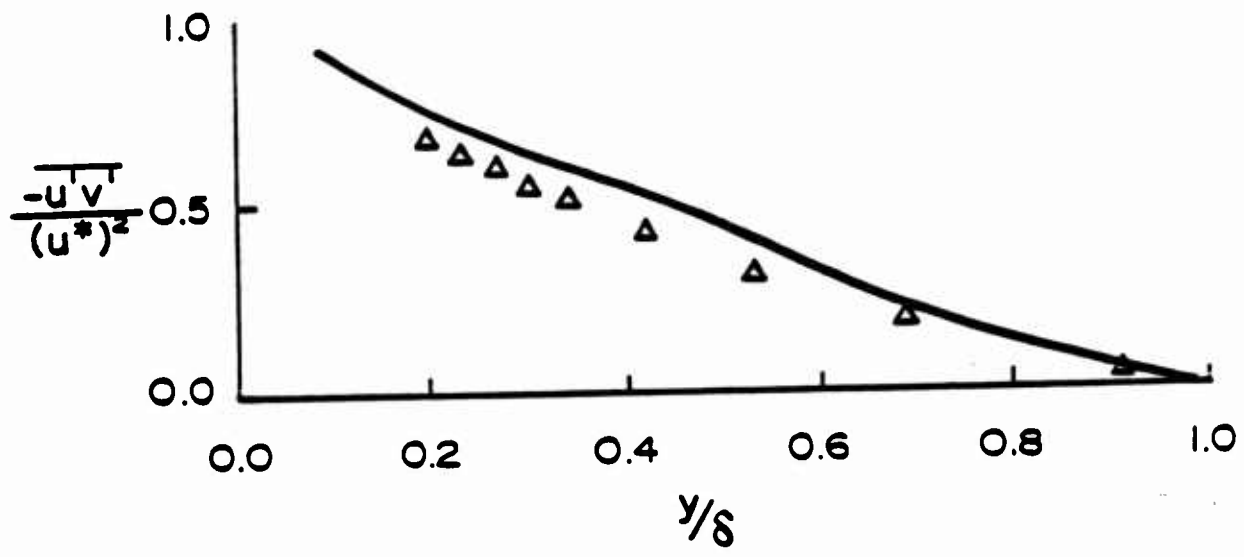


Figure 46. Typical Comparison of Calculated and Measured Reynolds Stress for Coleman's Equilibrium Pressure Gradient Run; $K_r = 0.29 \times 10^{-3}$

SECTION VIII

SUMMARY, CONCLUSIONS, AND RECOMMENDATIONS

The present work is summarized below. Also, particular conclusions and recommendations are enumerated.

1. SUMMARY

The background of predictive modeling of turbulent flow over rough surfaces has been discussed. Of the four broad predictive approaches-- solution of the full, time-dependent, Navier-Stokes equations in a micro-grid; solution of the time-averaged Navier-Stokes equations in a micro-grid; solution of the time-averaged Navier-Stokes equations in a macro-grid; and solution of the time-averaged boundary layer equations in a macro-grid--only the last two are practical with present computer speed and storage capabilities. Since the macro-grid is not fine enough to resolve the details of the roughness geometry, some form of empirical input by means of a roughness model is required.

Of the two roughness model schemes discussed, the equivalent sand-grain approach has several inadequacies. It is based totally on momentum transport data; therefore, there is no physical reason for the equivalent sand-grain size to correlate heat transfer data. This approach attempts to reduce a multi-length scale problem to a single length scale problem. In addition, there is no adequate means to determine the sand-grain equivalent for a given rough surface without taking data on that particular surface or on a similar surface.

The discrete element approach overcomes many of the inadequacies of the equivalent sand-grain approach. It accounts for the momentum and energy transport between the roughness elements and the fluid in a physically meaningful manner. It accounts for the major roughness geometry parameters (height, spacing, and shape) and does not rely on a single length scale. It includes more basic physics of the interactions between the roughness and the flow and uses a more general form of empirical input.

In the present work a discrete element model for turbulent boundary layer flow over a rough surface was rigorously derived. The necessary empirical information for the roughness model was provided by calibrating

the model using base data sets. This calibrated model was then compared with several independent data sets covering both the transitionally rough and fully rough regimes. The results of these comparisons were, in general, very good.

In the course of the present work it was discovered that the very important data set of Schlichting [3] was flawed and that his data reduction method required correction. A discussion of the reanalysis of this data set and the corrected data are presented in Appendix A. This is a very important consideration since Schlichting's data is the basis for almost all of the previous models for flow over rough surfaces.

2. CONCLUSIONS

a. The traditional equivalent sand-grain approach is restricted as a predictive model for flow over rough surfaces, especially for heat transfer predictions. It may require specific empirical input for a given rough surface.

b. The discrete element model which is derived in the present work for distributed three-dimensional roughness is based on the fundamental physical nature of the interactions between the flow and a rough surface. The resulting partial differential equations account for the mechanisms of momentum and energy transport in a physically meaningful manner.

c. In the present model the necessary empirical information for the roughness model is of a more general nature (than previous models) and the model can be calibrated for broad classes of roughness geometry. For example, the calibration given in the present work should apply to nearly all three-dimensional distributed roughnesses whose cross-sectional areas can be reasonably approximated by circles.

d. Calculations using the present discrete element model have been compared with 118 separate experimental runs on 18 separate rough surfaces. The results of these comparisons show that the present discrete element model is a predictive model of acceptable accuracy for both heat transfer and skin friction.

e. The important data set of Schlichting [3] is flawed. The corrected values given in Appendix A should be used for any comparisons with this data set. Any previous work that is based on the original Schlichting data set should be used cautiously.

3. RECOMMENDED FUTURE RESEARCH

a. The experimental data base from well-controlled experiments with well-defined rough surfaces is very limited. For example, all of the well-defined heat transfer data are based on experiments that were conducted on a single rough surface. It is recommended that an experimental program be undertaken to establish a definitive, high-quality data base for both uniformly rough and randomly rough surfaces.

b. The presence of a rough surface affects not only the value of the skin friction but also the entire momentum field within the boundary layer. Therefore, surface roughness could have a strong effect on flow separation. It is recommended that an investigation of the effect of surface roughness on flow separation be undertaken.

c. The present discrete element model is derived for three-dimensional distributed roughness. The important class of two-dimensional or strip-type roughness is characterized by different physical phenomena and requires a separate treatise. It is recommended that the discrete element method be extended to the two-dimensional roughness case.

d. Because of the lack of well-defined data for higher speed flows, the present model has been verified only for low speed flows. However, it should be applicable to higher speed flows so long as the flow in the immediate vicinity of the elements is subsonic. It is recommended that calculations using the present model be compared with data from experiments with high speed flows over well-defined rough surfaces as soon as such data become available.

e. Usually, compressible flow heat transfer data are nondimensionalized using the recovery or adiabatic wall temperature. The shear rates in a turbulent boundary layer over a rough surface can be significantly different than those for an otherwise similar flow over a smooth surface. Therefore, the adiabatic wall temperature may be significantly different. It is recommended that the effects of surface roughness on the adiabatic wall temperature be investigated.

f. Any profilometer trace that is used to quantify a randomly rough surface will have a built-in bias, since there is no way to insure that the profilometer stylus will encounter the crests of the elements. Therefore, it is recommended that the statistics of random roughness be investigated.

REFERENCES

1. Nikuradse, J., "Laws for Flows in Rough Pipes," VDI-Forschungsheft 361, Series B, Vol. 4, 1933; NACA TM 1292, 1950.
2. Morris, H. M., Applied Hydraulics in Engineering, Ronald Press Co., New York, 1963.
3. Schlichting, H., "Experiment Investigation of the Problem of Surface Roughness" Ingenieur-Archiv, Vol. VII, No. 1, 1936; NACA TM 823, 1937.
4. Pimenta, M. M., "The Turbulent Boundary Layer: An Experimental Study of the Transport of Momentum and Heat with the Effect of Roughness," Ph.D. Dissertation, Dept. Mech. Eng., Stanford Univ., 1975; Report HMT-21.
5. Coleman, H. W., "Momentum and Energy Transport in the Accelerated Fully Rough Turbulent Boundary Layer," Ph.D. Dissertation, Dept. Mech. Eng., Stanford Univ., 1976; Report HMT-24.
6. Ligrani, P. M., "The Thermal and Hydrodynamic Behavior of Thick, Rough-Wall, Turbulent Boundary Layers," Ph.D. Dissertation, Dept. Mech. Eng., Stanford Univ., 1979; Report HMT-29.
7. Uram, E. M., "Analysis of the Roughness Function and Wall Law Slope for Rough Surface Turbulent Boundary Layers," ASME Paper 81-FE-36, 1981.
8. Perry, A. E. and Joubert, P. N., "Rough-Wall Boundary Layers in Adverse Pressure Gradients," J. of Fluid Mech., Vol. 17, pp. 193-211, 1963.
9. Monin, A. S. and Yaglom, A. M., Statistical Fluid Mechanics, Vol. 1, MIT Press, 1971.
10. Perry, A. E., Schofield, W. H., and Joubert, P. H., "Rough Wall Turbulent Boundary Layers," J. of Fluid Mech., Vol. 27, pp. 383-413, 1969.
11. Dvorak, F. A., "Calculation of Turbulent Boundary Layers on Rough Surfaces in Pressure Gradients," AIAA Journal, Vol. 7, pp. 1752-1759, 1969.
12. Simpson, R. L., "A Generalized Correlation of Roughness Density Effects on the Turbulent Boundary Layer," AIAA Journal, Vol. 11, pp. 242-244, 1973.

13. Dirling, R. B., Jr., "A Method for Computing Rough Wall Heat Transfer Rates on Reentry Nose Tips," AIAA Paper No. 73-763, 1973.
14. Berg, D. E., "Surface Roughness Effects on the Hypersonic Turbulent Boundary Layer," Ph.D. Dissertation, Graduate Aeronautical Laboratories, Cal. Tech., 1977.
15. King, M. J., et al., "Roughness Characteristics of Plane Surfaces Based on Velocity Similarity Laws," ASME Paper 81-FE-34, 1981.
16. Dipprey, D. F. and Sabersky, R. H., "Heat and Momentum Transfer in Smooth and Rough Tubes at Various Prandlt Numbers," I. J. of Heat and Mass Trans., Vol. 6, pp. 329-353, 1963.
17. Nestler, D. E., "Compressible Turbulent Boundary Layer Heat Transfer to Rough Surfaces," ASME Paper 70-742, 1970.
18. Seidman, M. H., "Rough Wall Heat Transfer in Compressible Turbulent Boundary Layer," AIAA Paper 78-163, 1978.
19. Cebeci, T. and Chang, K. C., "Calculation of Incompressible Rough-Wall Boundary-Layer Flows," AIAA Journal, Vol. 16, pp. 730-735, 1978.
20. Lin, T. C. and Bywater, R. J., "The Evaluation of Selected Turbulence Models for High-Speed Rough-Wall Boundary Layer Calculations," AIAA Paper 80-C132, 1980.
21. Adams, J. C. and Hodge, B. K., "The Calculation of Compressible Transitional Turbulent and Relaminarizational Boundary Layers over Smooth and Rough Surfaces using an Extended Mixing-Length Hypothesis," AIAA Paper 77-682, 1977.
22. Liepmann, H. W. and Goddard, F. E., "Note on the Mach Number Effect Upon the Skin Friction of Rough Surfaces," J. Aeronautical Sci., Vol. 24, p. 784, 1957.
23. Lewis, M. J., "An Elementary Analysis for Predicting the Momentum and Heat Transfer Characteristics of a Hydraulically Rough Surface," J. Heat Transfer, Vol. 97, pp. 249-254, 1975.
24. Finson, M. L. and Wu, P. K. S., "Analysis of Rough Wall Turbulent Heating with Applications to Blunted Flight Vehicles," AIAA Paper 79-008, 1979.
25. Finson, M. L. and Clark, A. S., "The Effect of Surface Roughness Character on Turbulent Reentry Heating," AIAA Paper 80-1459, 1980.

26. Finson, M. L., "A Model for Rough Wall Turbulent Heating and Skin Friction," AIAA Paper 82-0199, 1982.
27. Christoph, G. A., "Law of the Wall Analysis for Turbulent Heating on Rough Surfaces," AIAA Paper 82-0197, 1982.
28. Christoph, G. H. and Pletcher, R. H., "Prediction of Rough-Wall Skin Friction and Heat Transfer," AIAA Journal, Vol. 21, No. 4, pp. 509-515, 1983.
29. Roberson, J. A., "Surface Resistance as a Function of the Concentration and Size of Roughness Elements," Ph.D. Dissertation, University of Iowa, 1961.
30. Roberson, J. A. and Chen, C. K., "Flow in Conduits with Low Roughness Concentration," J. Hydraulics Div., ASCE, Vol. 96, No. HY4, pp. 941-957, 1970.
31. Kumar, S. and Roberson, J. A., "General Algorithm for Rough Conduit Resistance," J. Hydraulics Div., ASCE, Vol. 106, No. HY11, pp. 1745-1764, 1980.
32. Healzer, J. M., "The Turbulent Boundary Layer on a Rough, Porous Plate: Experimental Heat Transfer with Uniform Blowing," Ph.D. Dissertation Dept. Mech. Eng., Stanford Univ., 1974; Report HMT-18.
33. Zukauskas, A., "Heat Transfer from Tubes in Crossflow," Advances in Heat Transfer, Academic Press, New York, 1972.
34. White, F. M., Viscous Fluid Flow, McGraw-Hill, New York, 1974.
35. Adams, J. C. and Martindale, W. R., "Hypersonic Lifting Body Boundary-Layer Analysis at High Angles of Incidence," J. of Spacecraft and Rockets, Vol. 11, No. 10, p. 721, 1974.
36. Kearney, D. W., "The Turbulent Boundary Layer: Experimental Heat Transfer with Strong Favorable Pressure Gradients and Blowing," Ph.D. Dissertation, Dept. Mech. Eng., Stanford Univ., 1970; Report HMT-12.
37. Chen C. K., "Characteristics of Turbulent Flow Resistance in Pipes Roughened with Hemispheres," Ph.D. Dissertation, Washington State Univ., 1971.
38. Leutheusser, H. J., "Turbulent Flow in Rectangular Ducts," J. of the Hydraulics Div., ASCE, Vol. 82, No. HY3, pp. 1-18, 1963.
39. Schenck, H., Theories of Engineering Experimentation, Hemisphere Publishing Co., Washington, 1979.

APPENDIX A

REEVALUATION OF SCHLICHTING'S SURFACE ROUGHNESS EXPERIMENT

In the course of working with the Schlichting [3] data we were led to question several of the assumptions used by Schlichting in his data reduction. This is not to say that Schlichting made errors in his analysis in 1936. That this work has been so widely used by so many researchers in the past forty-plus years argues for the basic soundness and importance of the work. Rather, additional data and analytical results published since 1936 now allow the use of more precise assumptions and enable a reevaluation of the original data. The present availability of the digital computer also facilitates the analysis of large data sets and allows more options to be considered than was reasonable with hand calculations.

In this appendix, results of the reevaluation of Schlichting's original data for the surfaces roughened with spheres, spherical segments, and cones are presented. It is shown that the original skin friction coefficients are higher than the corrected values by amounts ranging from 0.5% to 73%. Also, the equivalent sand roughness values were reevaluated for the same set of surfaces. These values are also presented, and it is shown that the original values are higher than the corrected values by amounts ranging from 26% to 555%.

1. SCHLICHTING'S EXPERIMENT

The experiment utilized a water tunnel with a test section of 40 mm height and 170 mm width. A 3.2-m-long section with four smooth walls preceded the 3.2-m-long section in which the upper wall was rough and the side and lower walls were smooth. Fully developed channel flow thus existed in the section containing the rough wall. The 14 rough walls with spherical, spherical segment, and conical roughness elements were those of interest in this analysis. The geometry and nomenclature for the channel and roughness elements are shown in Figure A-1, and the values of the parameters for the rough surfaces are given in Table A-1.

The effective wall location for a rough wall was defined by Schlichting as the location of a "smooth wall that replaces the rough wall in such a manner as to keep the fluid volume the same." Thus, if V is the volume of all the roughness elements on a surface of dimensions L

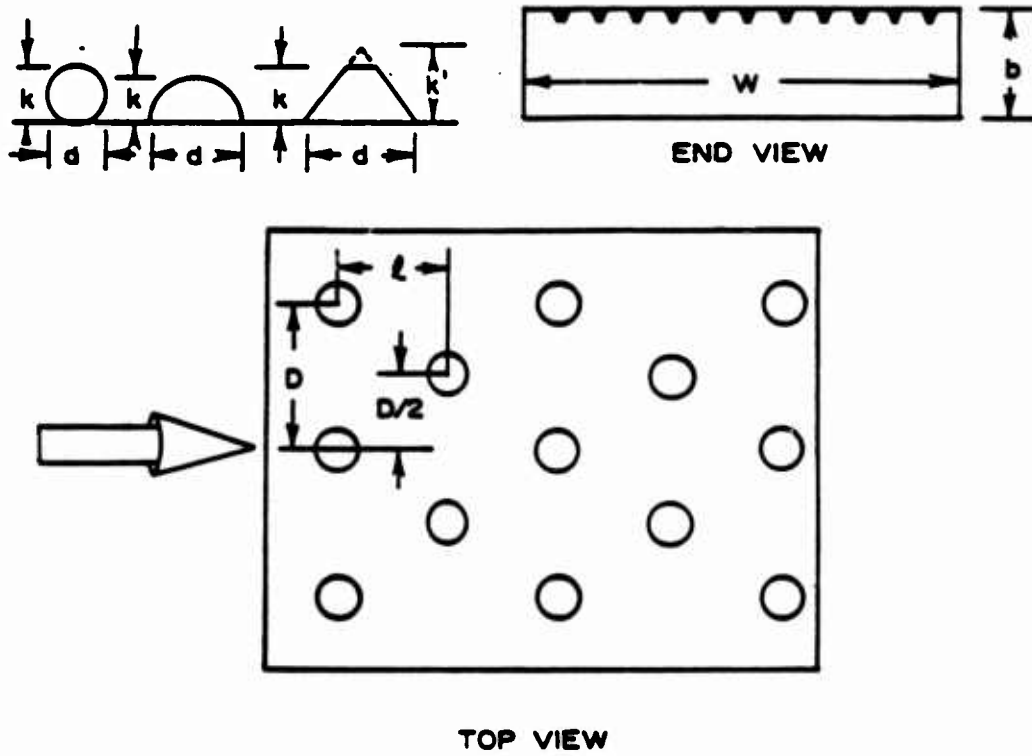


Figure A-1. Nomenclature for Schlichting's Experiment

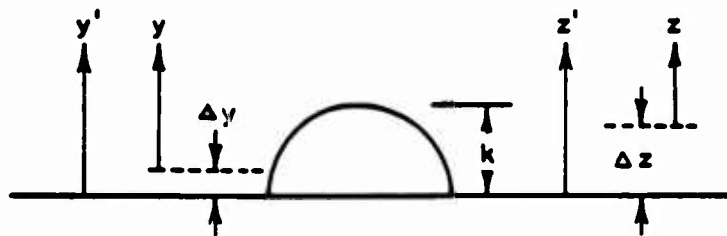


Figure A-2. Rough Wall Coordinate System Definitions

TABLE A-1. DESCRIPTION OF SCHLICHTING'S SURFACE ROUGHNESS
AND CORRECTED EQUIVALENT SAND-GRAIN ROUGHNESS

Plate No.	d (cm)	D (cm)	l (cm)	k (cm)	k' (cm)	b (cm)	SCHL. k_s/k	CORR. k_s/k
SPHERES								
XII	0.41	4	4	0.41	-- ^a	3.99	0.277	0.120
III	0.41	2	2	0.41	--	3.99	0.838	0.410
I	0.41	1	1	0.41	--	3.96	3.07	2.43
II	0.41	0.6	0.6	0.41	--	3.88	3.81	2.59
V	0.41	0.41	0.36	0.41	--	3.68	0.626	0.378
VI	0.21	1	1	0.21	--	3.99	0.819	0.430
IV	0.21	0.5	0.5	0.21	--	3.97	3.61	2.47
SPHERICAL SEGMENTS								
XIII	0.8	4	4	0.26	--	3.99	0.118	0.018
XIV	0.8	3	3	0.26	--	3.99	0.186	0.034
XV	0.8	2	2	0.26	--	3.98	0.571	0.278
XIX	0.8	0.8	0.69	0.26	--	3.85	1.40	0.953
CONES								
XXIII	0.8	4	4	0.375	0.425	3.99	0.159	0.046
XXIV	0.8	3	3	0.375	0.425	3.98	0.437	0.122
XXV	0.8	2	2	0.375	0.425	3.95	0.996	0.471

^a -- not applicable

by W , then $\Delta y = V/LW$ is the distance of the effective wall location from the smooth wall on which the roughness elements occur. This is illustrated in Figure A-2. The mean channel height, b , was then taken to be the original distance between smooth upper and lower walls (40 mm) minus Δy .

For each of the rough surfaces used, either 5 or 6 different Reynolds number runs were made. Data taken were the pressure drop in the rough wall test section and the velocity profile at the outlet plane of the rough wall test section. A pitot probe was used for the velocity measurements. The flow rate was not reported, so the reported maximum velocity, u_{\max} , is used as the reference velocity in the Reynolds number and skin friction coefficient definitions:

$$Re = u_{\max} b / \nu \quad (A-1)$$

$$C_f = 2\tau / \rho u_{\max}^2 = 2u^{*2} / u_{\max}^2 \quad (A-2)$$

where τ is the wall shear stress and u^* is the friction velocity.

Actually, for the rough wall τ is considered to be the force on the wall in the mean flow direction divided by the plan area of the wall, since the force on the wall consists of shear and form drag components. In the following, the words "wall shear stress" are used in this sense when referring to values for the rough walls.

2. SCHLICHTING'S EVALUATION OF C_f

Schlichting determined the skin friction on the rough walls by two different methods, and then reported the average of these values, $C_{f,av}$, as the value of skin friction. The first method he used (subscript 1) was based on the pressure drop measurements, while the second method (subscript 2) was based on the measured velocity profiles and a rough surface law of the wall.

For the first method, an application of the basic momentum theorem to the fully developed flow in the channel yields the equation Schlichting used

$$\tau_{r1} + \tau_s = b |dP/dx| \quad (A-3)$$

if one assumes the shear stresses on the smooth side walls are negligible.

Here, the subscripts r and s refer to the rough and smooth walls, respectively. This can be recast, using the definition of friction velocity, as

$$u_{r1}^{*2} + u_{s1}^{*2} = \frac{b}{\rho} \left| \frac{dP}{dx} \right| \quad (A-4)$$

The smooth wall friction velocity was determined by plotting the measured velocity profile on the smooth wall in u vs. $\log y$ coordinates, determining the slope n_s graphically, and by comparison with the smooth wall log law

$$u/u_{s1}^* = 5.5 + 5.75 \log (yu_{s1}^*/\nu) \quad (A-5)$$

finding

$$u_{s1}^* = n_s/5.75 \quad (A-6)$$

This determination, together with the measured pressure drop data, allowed calculation of u_{r1}^* using equation (A-4). These values are presented in Table A-2 in the dimensionless form C_{f1} for the seventy-nine runs made with the rough surfaces of interest in this study.

For the second method, Schlichting used a rough wall log law

$$u/u_{r2}^* = 5.75 \log (y/k) + A \quad (A-7)$$

where y is measured from the effective wall location as described previously and k is roughness height. For Nikuradse's fully rough sand roughness cases, $A = 8.48$ and $k = k_s$, the sand grain size. From the velocity profile measurements on each rough wall, Schlichting knew u vs. y' (see Figure A-2). By plotting u vs. $\log (y' - \Delta y)$, determining the slope n_r graphically, and comparing with equation (A-7), he was able to calculate

$$u_{r2}^* = n_r/5.75 \quad (A-8)$$

These values are presented in Table A-2 in the dimensionless form C_{f2} .

Also shown in Table A-2 are the averages of C_{f1} and C_{f2} , labeled $C_{f,av}$, which were the values reported by Schlichting.

3. REEVALUATION OF C_f

As described in the previous section, Schlichting determined his

TABLE A-2. COMPARISON OF ORIGINAL AND CORRECTED SKIN FRICTION COEFFICIENTS

Plate No. (l/k)	Re ($\times 10^{-3}$)	u_{max} (cm/sec)	SCHLICHTING			CORRECTED		
			C_{f1} ($\times 10^3$)	C_{f2} ($\times 10^3$)	$C_{f,av}$ ($\times 10^3$)	C_{fc} ($\times 10^3$)	Re_{ks}	Δz^a (cm)
SPHERES								
XII (9.75)	110	321	7.60	7.01	7.31	6.29	75	0.12
	124	385	7.44	7.21	7.33	6.24	91	0.12
	162	476	7.52	7.13	7.32	6.46	114	0.12
	190	547	7.33	7.31	7.32	6.26	130	0.12
	224	650	6.86	7.85	7.35	5.69	148	0.12
III (4.88)	107	316	10.22	11.94	11.06	8.66	299	0.12
	138	391	10.48	11.70	11.08	9.18	394	0.12
	174	500	10.06	12.13	11.07	8.70	486	0.21
	204	568	10.28	11.83	11.04	9.01	572	0.21
	251	704	10.17	11.94	11.04	8.95	700	0.21
	290	816	10.19	11.76	10.96	8.99	806	0.21
I (2.44)	107	310	19.34	17.16	18.23	18.13	2556	--
	132	384	18.95	17.40	18.17	17.87	3118	0.08
	166	508	17.77	18.70	18.23	16.42	3819	--
	195	566	17.48	18.94	18.20	16.11	4360	0.16
	224	658	17.69	18.75	18.22	16.42	5127	0.16
	263	778	17.60	18.79	18.19	16.37	5944	0.16
II (1.46)	104	313	16.76	23.80	20.13	15.46	2562	0.41
	129	384	17.86	22.92	20.31	16.73	3243	--
	166	500	18.34	22.07	20.16	17.23	4248	--
	186	586	18.36	22.01	20.14	17.17	4774	0.37
	224	646	18.70	21.86	20.25	17.57	5691	0.41
	257	746	19.04	21.43	20.22	18.00	6708	--
V (0.87)	98	311	9.62	10.77	10.19	8.08	264	--
	123	385	9.87	10.54	10.20	8.44	337	--
	162	498	9.81	10.64	10.22	8.37	438	--
	190	585	9.95	10.48	10.21	8.52	525	--
	214	662	9.94	10.49	10.21	8.56	589	0.41
	263	809	10.17	10.25	10.21	8.86	739	0.37
VI (4.86)	110	316	8.44	8.90	8.67	7.12	147	0.11
	135	390	8.20	9.18	8.68	6.82	177	--
	170	491	8.70	8.72	8.71	7.55	234	--
	200	566	8.71	8.66	8.69	7.61	276	--
	234	664	8.39	9.02	8.70	7.21	315	0.11
	275	806	8.47	8.96	8.71	7.32	373	--
IV (2.43)	107	325	14.69	14.37	14.53	13.50	1154	--
	129	396	13.44	15.74	14.57	12.02	1316	--
	186	572	13.96	15.16	14.56	12.90	1953	--
	204	646	13.68	15.45	14.55	12.59	2126	--
	245	751	13.62	15.55	14.57	12.53	2548	0.13

^a -- not determined.

TABLE A-2. COMPARISON OF ORIGINAL AND CORRECTED
SKIN FRICTION COEFFICIENTS (CONCLUDED)

Plate No. (l/k)	Re ($\times 10^{-3}$)	u_{max} (cm/sec)	SCHLICHTING			CORRECTED		
			C_{f1} ($\times 10^3$)	C_{f2} ($\times 10^3$)	$C_{f,av}$ ($\times 10^3$)	C_{fc} ($\times 10^3$)	Re_{ks}	Δz^a (cm)
SPHERICAL SEGMENTS								
XIII (15.4)	115	314	5.77	5.15	5.46	4.32	6	--
	141	389	5.15	5.76	5.45	3.72	7	0.16
	178	495	5.56	5.40	5.48	4.37	10	--
	204	574	5.54	5.39	5.46	4.40	11	--
	229	648	4.99	5.91	5.44	3.70	12	0.16
	302	830	4.69	6.25	5.44	3.33	14	0.16
XIV (11.5)	135	380	5.61	6.50	6.05	4.12	14	--
	174	497	5.85	6.72	6.03	4.57	18	0.23
	195	572	6.05	6.08	6.07	4.87	22	--
	245	700	5.10	7.08	6.05	3.68	23	--
	295	834	4.94	7.29	6.06	3.50	27	0.23
XV (7.69)	135	382	8.43	8.70	8.57	7.16	146	--
	170	502	8.54	8.53	8.54	7.42	187	0.18
	190	564	8.25	8.88	8.56	7.04	205	--
	234	687	7.83	9.37	8.58	6.51	242	--
	288	817	8.02	9.08	8.54	6.79	302	0.13
XIX (2.65)	107	316	11.29	11.40	11.35	9.93	484	--
	132	386	11.13	11.76	11.45	9.75	590	--
	158	480	11.49	11.26	11.38	10.27	734	--
	186	563	10.60	12.23	11.40	9.08	803	--
	224	671	11.44	11.31	11.37	10.21	1033	0.26
	282	818	11.46	11.37	11.42	10.25	1296	--
CONES								
XXIII (10.7)	117	321	6.04	6.83	6.43	4.67	24	--
	141	386	6.16	6.72	6.44	4.89	30	--
	178	488	5.98	6.93	6.44	4.69	37	0.30
	214	574	6.09	6.83	6.45	4.84	45	--
	251	668	6.28	6.67	6.47	5.17	55	0.30
XXIV (8.00)	112	307	8.60	8.54	8.57	7.31	79	--
	141	384	8.12	9.12	8.61	6.88	95	--
	186	495	7.94	9.33	8.62	6.77	123	--
	209	567	7.61	9.67	8.61	6.39	136	--
	251	662	7.41	9.87	8.60	6.19	159	0.38
	324	890	7.50	9.79	8.61	6.38	211	0.38
XXV (5.33)	115	310	11.37	11.42	11.40	10.32	375	--
	145	388	10.22	12.50	11.33	8.93	428	--
	178	476	10.20	12.62	11.38	8.91	530	--
	209	564	10.54	12.20	11.39	9.38	638	--
	251	668	10.51	12.29	11.39	9.34	761	0.30
	295	787	10.55	12.19	11.36	9.42	909	0.34

^a -- not determined.

C_{f1} values by neglecting the shear on the two smooth side walls. If the side wall shear is included, application of the basic momentum theorem yields

$$\tau_r = b \left| \frac{dP}{dx} \right| - \left(\frac{W + 2b}{W} \right) \tau_{s,av} \quad (A-9)$$

where $\tau_{s,av}$ is the average shear stress on the three smooth walls. The value of smooth wall shear was determined as described previously from a smooth bottom wall velocity profile measured in a plane parallel to and midway between the side walls.

Examination of the data of Leutheusser [38] for the shear distribution around the walls of a smooth channel of aspect ratio 3:1 for turbulent fully developed flow shows that the shear stress in this center plane is larger than the average shear stress over the channel perimeter by 10 to 20%, depending on Reynolds number. The present authors have used the following relationship between the average shear stress and $\tau_{s,meas}$, the smooth wall value of the centerplane determined by Schlichting:

$$\tau_{s,meas} = 1.10 \tau_{s,av} \quad (A-10)$$

This was chosen with the realization that, for the larger aspect ratio used by Schlichting, the influence of the corner flows on the average shear stress should be slightly less than in Leutheusser's case. In addition, of course, Leutheusser had no influence of a rough upper wall on his flows.

Recasting (A-9) and (A-10) in terms of friction velocities,

$$u_{rc}^{*2} = \frac{b}{\rho} \frac{dP}{dx} - \left(\frac{W + 2b}{1.10 W} \right) u_{s,meas}^{*2} \quad (A-11)$$

where the rc subscript indicates a corrected rough wall value. All values on the right hand side of (A-11) were reported by Schlichting, allowing calculation of u_{rc}^* for each run. These values are reported in Table A-2 in the dimensionless form C_{fc} . Comparison of $C_{f,av}$ and C_{fc} shows the originally reported values are larger than the corrected ones by 0.5% to 73%, depending on Reynolds number and surface roughness.

Now consider the velocity profile slope method of determining wall shear. Using the z-coordinate shown in Figure A-2 to avoid confusion

with Schlichting's Δy , (A-7) can be written as

$$u = 5.75 u_{r2}^* \log(z' - \Delta z) - 5.75 u_{r2}^* \log k + Au_{r2}^* \quad (A-12)$$

For a given velocity profile on a given surface, the final two terms in (A-12) are constants, so u_{r2}^* can be calculated from a slope determination using the measured data pairs (u, z') if Δz is known a priori.

In using this approach, Schlichting assumed that his Δy (as defined previously) was equal to the Δz in (A-12), which is the wall shift required to give a velocity profile slope of 5.75 in u^+ vs. $\log z$ coordinates. Although the definition of Schlichting's Δy is a very logical one when considered on physical grounds, it is unrelated to any characteristics (assumed or proven) of the velocity profile.

Unfortunately, for the cases investigated by Schlichting, the skin friction determined using this technique is highly sensitive to the value of Δz . This is illustrated in Figure A-3, which shows the results obtained for the value of C_f using this technique and considering a range of Δz values from zero to the roughness element height. The velocity profile data used are for plate III, $Re = 107,000$. The slope determinations were made using a linear least-squares regression in u vs. $\log(z' - \Delta z)$ coordinates. Plotted for comparison with the curve are two points. One is Schlichting's C_{f2} (graphical slope determination) plotted using his value of Δy . The other is the corrected value determined from the pressure drop measurements (C_{fc}) plotted at the optimum value of Δz (discussed in the following subsection).

When u^* is not known from an independent measurement, the question of which Δz choice gives the best linear regression is generally one which cannot be answered unambiguously when actual velocity profiles are being evaluated. This is illustrated in Figure A-4, which shows the standard error of estimates (Schenck, [39]) vs. $\Delta z/k$ for the results which are presented in Figure A-3. For this particular case, there is essentially no difference in the standard error over the range $\Delta z/k$ from 0.0 to 0.2, and the difference for $\Delta z/k$ from 0.0 to 0.5 is only $\pm 5\%$ about the average value of standard error in that range.

After considering the sensitivity of the velocity profile slope method to the assumptions required to obtain a value of u^* , it was

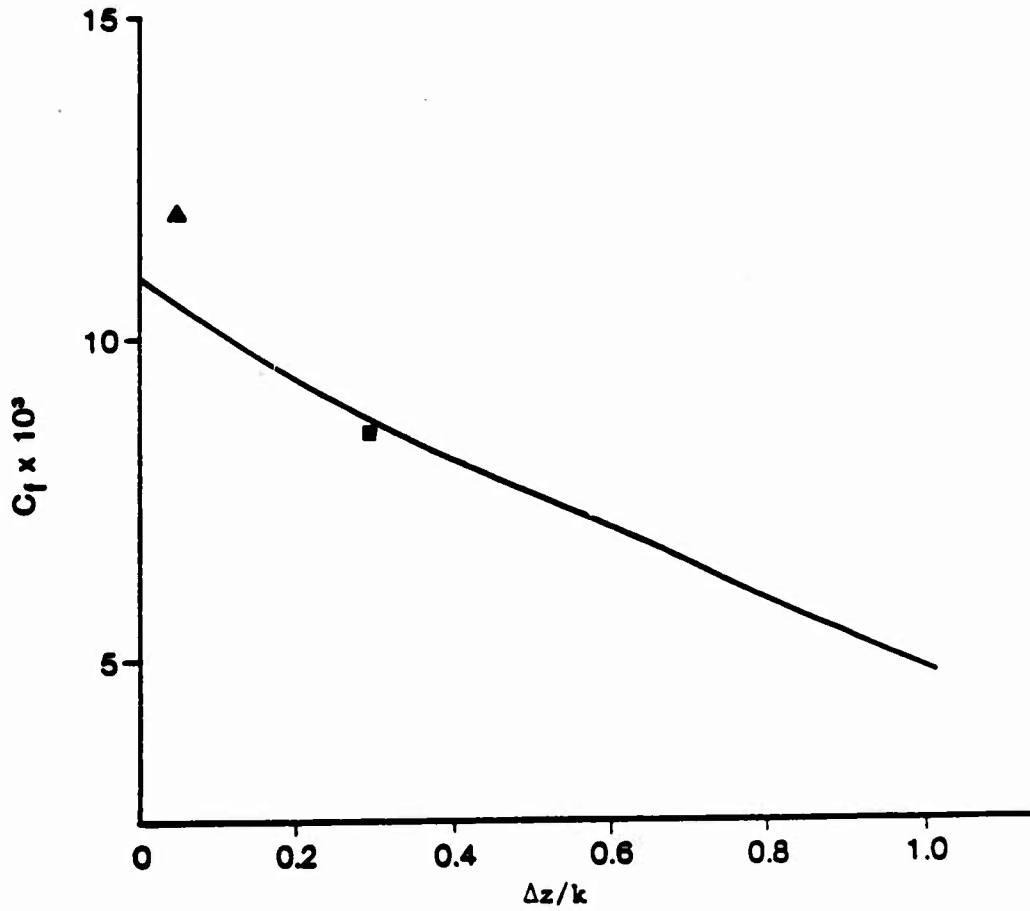


Figure A-3. Demonstration of Influence of Effective Wall Location on Skin Friction Calculated From Velocity Profile Slope; Plate III, $Re = 107,000$, ▲ $-C_{f2}$, ■ $-C_{fc}$

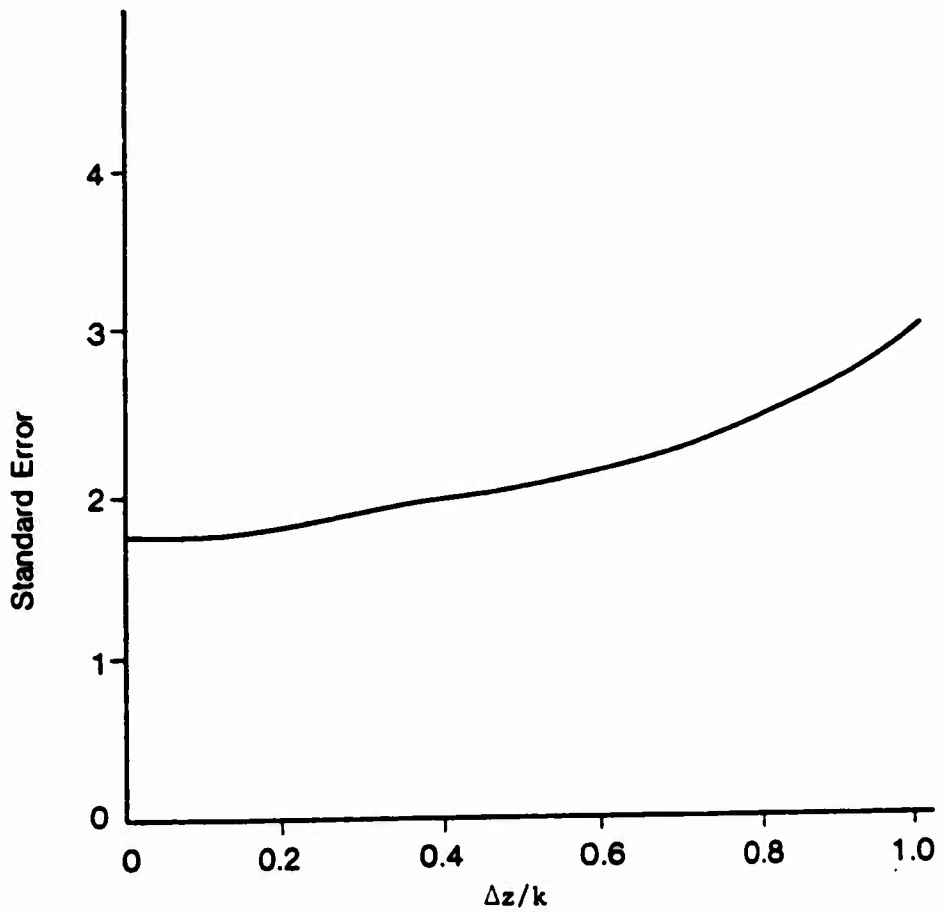


Figure A-4. Standard Error of Estimates for Velocity Profile Regressions for the Effective Wall Locations in Figure A-3

concluded that for the conditions of the Schlichting experiment this approach produces estimates of u^* for which the uncertainties are much larger than for those estimates based on pressure drop measurements. Therefore, the corrected (C_{fc}) values based on the pressure drop measurements are recommended as the best estimates of the true values of C_f in Schlichting's experiment.

4. REEVALUATION OF EQUIVALENT SAND ROUGHNESS

For each of the surfaces he tested, Schlichting determined an equivalent sand roughness, k_s . He did this by comparing the rough wall log law in the form

$$u/u^*_{r,av} = 5.75 \log(y/k) + A \quad (A-13)$$

to the form Nikuradse reported for his velocity profile data in the fully rough regime

$$u/u^* = 5.75 \log(y/k_s) + 8.48 \quad (A-14)$$

It should be noted that in (A-13),

$$y = y' - \Delta y \quad (A-15)$$

while Nikuradse [1] did not explicitly define the origin of his y coordinate used in (A-14). Schlichting set (A-13) and (A-14) equal, assumed all of his data were in the fully rough regime, and obtained

$$5.75 \log(k_s/k) = 8.48 - A \quad (A-16)$$

By computing an average value of A for each velocity profile using (A-13) and then calculating a mean value of A from all the profiles on each plate, he was then able to use (A-16) to solve for a k_s/k value for each of the rough surfaces he tested. These values are listed in Table A-1 for the surfaces of interest in the present study.

In view of the discussion in the preceding sections, the use of $u^*_{r,av}$ and Δy in (A-13) are open to serious question. It is more appropriate to use the corrected friction velocity and the wall shift Δz such that

$$u/u^*_{rc} = 5.75 \log[(z' - \Delta z)/k] + A \quad (A-17)$$

If (A-17) is used in determining an equivalent sand roughness, then Δz values must be determined before the computation can proceed.

Monin and Yaglom [9] show that, within the logarithmic layer, the quantity

$$z_0 = (z' - \Delta z) \exp(-\kappa u/u^*) \quad (\text{A-18})$$

is independent of distance from the wall. Thus, if the friction velocity and the data pairs (u, z') in a velocity profile are known, z_0 can be determined as a function of $(z' - \Delta z)$ for various Δz values. The optimum Δz value is then the one which gives values of z_0 which are the closest to being constant with $(z' - \Delta z)$. The optimum Δz values were determined in this study using the above approach and a criterion of minimum standard error of estimates from a linear least squares regression of z_0 on $(z' - \Delta z)$ with zero slope. The Karman constant, κ , was taken as 0.40 for consistency with the slope in (A-17).

In using this procedure, the velocity profile points must be read from Schlichting's [3] figures. The symbols for the different profiles are not distinguishable in most cases in the NACA English translation, so the original German version was used. Shown in Table A-2 are the calculated "optimum" Δz values for each of the velocity profiles which could be read from the figures.

For each of the profiles for which Δz was calculated, a linear least squares regression of the form of (A-17) was used to determine a value of A. Then (A-16) was used to calculate the corresponding k_s/k value. The mean values of k_s/k (shown in Table A-2) were then determined for each surface. Comparisons show that Schlichting's original k_s/k values are higher than the corrected values by 26% to 55%.

In using (A-16) to determine k_s/k , it is assumed that $(z' - \Delta z)$ for Schlichting's data and Nikuradse's y are equivalent. In other words, the origins for the coordinate systems must be those which give a slope of 5.75 in the log regions for both sets of data. It has been shown previously that Δz meets this requirement by its definition. However, since Nikuradse did not explicitly define his origin for y , the sensitivity of his results to a wall shift must be considered.

Fortunately, Nikuradse's results are much less sensitive to assumed wall position than are those of Schlichting. Nikuradse tested

configurations over a range of r/k from 15 to 507, where r is pipe radius and k is the average sand size. The analogous parameter in Schlichting's configurations, b_2/k , ranged from 6.1 to 13.8 for the surfaces considered in this study. Schlichting defined b_2 as the distance from the rough wall to the maximum in the velocity profile across the channel. If it is assumed that the virtual or effective wall location lies between the bottom and the top of the roughness elements, then the points in Nikuradse's velocity profiles are much less effected than are Schlichting's, since as z' becomes much greater than Δz , $\log(z' - \Delta z)$ approaches $\log(z')$.

Using the corrected k_s values for each surface and the corrected friction velocities u_{rc}^* , a roughness Reynolds number

$$Re_{k_s} = u_{rc}^* k_s / \nu \quad (A-19)$$

was calculated for each of Schlichting's runs which were considered. These values are recorded in Table A-2. It should be noted that for all runs using plates XIII, XIV, and XXIII, the calculated roughness Reynolds numbers are in the transitionally rough regime, not in the fully rough regime as assumed by Schlichting. Of course, the method by which the k_s values were determined assumes fully rough flow, so the meaning of the k_s values for these three plates is not the same as for those plates on which fully rough flow existed.

APPENDIX B

INTEGRAL BOUNDARY LAYER EQUATIONS
FOR FLOW OVER A ROUGH WALL

The integral forms of the boundary layer equations are often very useful when approximate boundary layer analyses are desired. Also, their development provides natural definitions for skin friction coefficient, Stanton number, and the usual integral length scales such as momentum thickness, displacement thickness, enthalpy thickness, etc.

For boundary layer flow over a rough surface, the following equations have been derived in the text. Furthermore, we recall that for most surfaces of interest $(1 - \alpha_x)_{ave} = (1 - \alpha_y) = (1 - \alpha)$.

Continuity:

$$\frac{\partial}{\partial x} [\rho(1 - \alpha)u] + \frac{\partial}{\partial y} [\rho(1 - \alpha)v] = 0 \quad (B-1)$$

Momentum:

$$\begin{aligned} \rho(1 - \alpha)u \frac{\partial u}{\partial x} + \rho(1 - \alpha)v \frac{\partial u}{\partial y} = & - \frac{\partial}{\partial y} [(1 - \alpha)\tau] \\ & + (1 - \alpha)\rho_e U_e \frac{dU_e}{dx} - \frac{1}{2} \rho C_D u^2 \frac{d}{Ll} \end{aligned} \quad (B-2)$$

Energy:

$$\begin{aligned} \rho(1 - \alpha)u \frac{\partial h}{\partial x} + \rho(1 - \alpha)v \frac{\partial h}{\partial y} = & - \frac{\partial}{\partial y} [(1 - \alpha)q] \\ & - (1 - \alpha)\tau \frac{\partial u}{\partial y} - u\rho_e (1 - \alpha)U_e \frac{dU_e}{dx} \\ & + \frac{1}{2} \rho C_D u^3 \frac{d}{Ll} + \frac{\pi \mu Nu_d (h_R - h)}{LlPr} \end{aligned} \quad (B-3)$$

First, we will consider the integral momentum equation. Multiplying continuity by $(u - U_e)$, adding it to the momentum equation and rearranging yields

$$\begin{aligned} - \frac{\partial}{\partial x} [\rho(1 - \alpha)u(U_e - u)] - \frac{dU_e}{dx} (1 - \alpha)(\rho_e U_e - \rho u) \\ + \frac{\partial}{\partial y} [\rho(1 - \alpha)uv] - U_e \frac{\partial \rho(1 - \alpha)v}{\partial y} \end{aligned}$$

$$= - \frac{\partial}{\partial y} [(1 - \alpha)\tau] - \frac{1}{2} \rho C_D u^2 \frac{d}{Ll} \quad (B-4)$$

Integrating equation (B-4) across the boundary layer with respect to y and recalling that $u_w = v_\infty = 0$, $\tau_w = -\tau_y = 0$ and $\tau_\infty = 0$ yields

$$\begin{aligned} & - \frac{\partial}{\partial x} \left[U_e^2 \int_0^\infty \rho(1 - \alpha) \frac{u}{U_e} \left(1 - \frac{u}{U_e} \right) dy \right] \\ & - \frac{dU_e}{dx} \rho_e U_e \int_0^\infty (1 - \alpha) \left(1 - \frac{\rho u}{\rho_e U_e} \right) dy \\ & + U_e (1 - \alpha)_w \rho_w v_w \\ & = - (1 - \alpha)_w \tau_w - \frac{1}{2} \frac{1}{Ll} \int_0^\infty \rho C_D (d) u^2 dy \end{aligned} \quad (B-5)$$

If we make the following definitions

$$\text{momentum thickness} = \theta = \int_0^\infty (1 - \alpha) \frac{\rho u}{\rho_e U_e} \left(1 - \frac{u}{U_e} \right) dy \quad (B-6)$$

$$\text{displacement thickness} = \delta^* = \int_0^\infty (1 - \alpha) \left(1 - \frac{\rho u}{\rho_e U_e} \right) dy \quad (B-7)$$

$$\text{skin friction coefficient} = \frac{C_f}{2} = \frac{(1-\alpha)_w \tau_w + \frac{1}{2} \frac{1}{Ll} \int_0^\infty \rho C_D (d) u^2 dy}{\rho_e U_e^2} \quad (B-8)$$

equation (B-5) takes the familiar form

$$\begin{aligned} \frac{C_f}{2} &= \frac{d\theta}{dx} + (2\theta + \delta^*) \frac{1}{U_e} \frac{dU_e}{dx} + \frac{\theta}{\rho_e} \frac{d\rho_e}{dx} \\ & - \frac{\rho_w (1 - \alpha_w) v_w}{\rho_e U_e} \end{aligned} \quad (B-9)$$

In the last term of equation (B-9), the factor $(1 - \alpha_w) v_w$ is the average transpiration velocity based on the total plan area.

Next we will consider the energy equation. We multiply momentum, (B-2), by u ; define stagnation enthalpy, $h_0 = h + u^2/2$; multiply continuity by h_0 ; and combine these two equations with energy to obtain

$$\begin{aligned}
& \frac{\partial}{\partial x} [\rho(1 - \alpha)uh_o] + \frac{\partial}{\partial y} [\rho(1 - \alpha)vh_o] \\
& = - \frac{\partial}{\partial y} [(1 - \alpha)q] - \frac{\partial}{\partial y} [(1 - \alpha)u\tau] \\
& \quad + \frac{\pi\mu Nu_d (h_R - h)}{L\ell Pr}
\end{aligned} \tag{B-10}$$

Integrating equation (B-10) across the boundary layer with respect to y and recalling $u_w = v_w = \tau_w = q_w = 0$ we get

$$\begin{aligned}
(1 - \alpha)_w q_w + \int_0^\infty \frac{\pi\mu Nu_d (h_R - h)}{L\ell Pr} dy \\
= \int_0^\infty \frac{\partial}{\partial x} [\rho(1 - \alpha)u(h_o - h_{oe})] \\
- \rho(1 - \alpha)_w v_w (h_o - h_{oe})_w
\end{aligned} \tag{B-11}$$

where we have, without any loss in generality, made the stagnation enthalpy at the boundary layer edge, h_{oe} , the datum for stagnation enthalpy. Normalizing equation (B-11) with $\rho_e U_e (h_w - h_e)$ and expanding the integral we get

$$\begin{aligned}
\frac{(1 - \alpha)_w q_w + \int_0^\infty \frac{\pi\mu Nu_d (h_R - h)}{PrL\ell} dy}{\rho_e U_e (h_w - h_e)} &= - \frac{\rho_w (1 - \alpha)_w v_w (h_o - h_{oe})_w}{\rho_e U_e (h_w - h_e)} \\
&+ \frac{1}{\rho_e U_e (h_w - h_e)} \frac{d}{dx} \int_0^\infty \rho_e U_e (h_w - h_e) \frac{\rho(1 - \alpha)u(h - h_e)}{\rho_e U_e (h_w - h_e)} dy \\
&- \frac{1}{2} \frac{1}{\rho_e U_e (h_w - h_e)} \frac{d}{dx} \int_0^\infty \rho_e U_e^3 \frac{\rho(1 - \alpha)u(U_e^2 - u^2)}{\rho_e U_e^3} dy \tag{B-12}
\end{aligned}$$

If we make the following definitions

$$\text{Stanton number} = St = \frac{(1 - \alpha)_w q_w + \int_0^\infty \frac{\pi\mu Nu_d (h_R - h)}{PrL\ell} dy}{\rho_e U_e (h_w - h_e)} \tag{B-13}$$

$$\text{enthalpy thickness} = \delta_h = \int_0^\infty (1 - \alpha) \frac{\rho u}{\rho_e U_e} \frac{h - h_e}{h_w - h_e} dy \tag{B-14}$$

$$\text{dissipation thickness} = \delta_d = \int_0^{\infty} (1-\alpha) \frac{\rho u}{\rho_e U_e} \left(1 - \frac{u^2}{U_e^2} \right) dy \quad (\text{B-15})$$

$$\text{Eckert number} = E_c = \frac{U_e^2}{2(h_w - h_e)} \quad (\text{B-16})$$

equation (B-12) takes the familiar form

$$\begin{aligned} St = \delta_h \left[\frac{1}{\rho_e} \frac{d\rho_e}{dx} + \frac{1}{U_e} \frac{dU_e}{dx} + \frac{1}{h_w - h_e} \frac{d(h_w - h_e)}{dx} \right] \\ + \frac{d\delta_h}{dx} - E_c \frac{d\delta_d}{dx} - \delta_d \left[\frac{E_c}{\rho_e} \frac{d\rho_e}{dx} + \frac{3E_c}{U_e} \frac{dU_e}{dx} \right] \\ - (1-\alpha)_w \frac{\rho_w v_w}{\rho_e U_e} + (1-\alpha)_w v_w \frac{\rho_w}{\rho_e} E_c \end{aligned} \quad (\text{B-17})$$

As an alternate formulation, we can normalize equation (B-11) with respect to the stagnation enthalpy defect, $\rho_e U_e (h_{ow} - h_{oe})$, and define a stagnation Stanton number and enthalpy thickness

$$St_o = \frac{(1-\alpha)_w q_w + \int_0^{\infty} \frac{\pi \mu u_d (h_R - h)}{Pr L} dy}{\rho_e U_e (h_{ow} - h_{oe})} \quad (\text{B-18})$$

$$\delta_{ho} = \int_0^{\infty} (1-\alpha) \frac{\rho u}{\rho_e U_e} \frac{h_o - h_{oe}}{h_{ow} - h_{oe}} dy \quad (\text{B-19})$$

to get the other familiar form

$$\begin{aligned} St_o = \frac{d\delta_{ho}}{dx} + \delta_{ho} \left[\frac{1}{\rho_e} \frac{d\rho_e}{dx} + \frac{1}{U_e} \frac{dU_e}{dx} \right. \\ \left. + \frac{1}{h_{ow} - h_{oe}} \frac{d(h_{ow} - h_{oe})}{dx} \right] - (1-\alpha)_w \frac{\rho_w v_w}{\rho_e U_e} \end{aligned} \quad (\text{B-20})$$

APPENDIX C

ON THE PROBLEM OF ROUGHNESS ELEMENT TEMPERATURE

In the derivation of the energy equation for the rough surface boundary layer it was assumed that the temperature of the roughness element was known. The problem of defining this temperature is addressed below.

The temperature distribution within the element will, in general, be three-dimensional. This temperature distribution could be found by solving the three-dimensional conduction equation with appropriate boundary conditions. This would be a significant undertaking on the order of solving the two-dimensional boundary layer equations. Also, since the temperature profile must be determined at each iteration of the boundary layer equations, the required computations would be increased by an order of magnitude.

Fortunately, the exact temperature distribution in the element is of little concern, since the major concern is the total heat transfer rate between the fluid and the substrate. This heat transfer is affected by the roughness elements in two ways:

- (1) The elements influence the nature of the turbulence and the momentum field, thereby influencing the energy field in the boundary layer.
- (2) The elements influence the path for conduction for the fluid to the substrate in such a way as to:
 - (a) Increase the effective surface area (fin effect); or
 - (b) Insulate the surface.

Effect (1) must be accounted for in the models of the turbulence and the momentum field. Effect (2) is included in the model of the energy field by way of the blockage terms and the distributed heat source (sink) terms. It is the heat source (sink) term that requires a definition of roughness element temperatures.

The lumped mass approach described below gives a simple method to define an element temperature that accounts for the important effects of conduction through the element and contact resistance at the boundary between the element and the surface.

Figure C-1 shows a schematic diagram of the element and the nomenclature used in this appendix. It is assumed that the mass of the element is lumped at the centroid. For steady state

$$q = \int_0^k \pi d H (T_R - T(y)) dy = \frac{T_w - T_R}{R_1 + R_2} \quad (C-1)$$

Solving for T_R yields

$$T_R = \frac{T_w + \pi(R_1 + R_2) \int_0^k (d)HT(y)dy}{1 + \pi(R_1 + R_2) \int_0^k (d)Hdy} \quad (C-2)$$

where

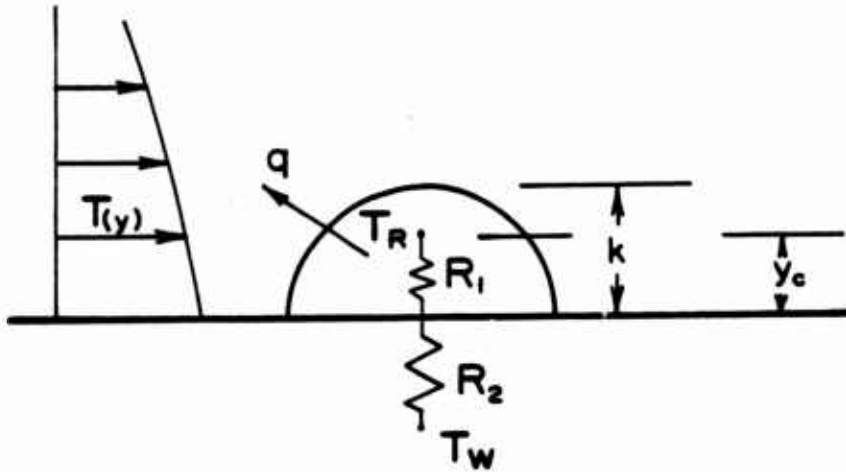
$$R_1 = \frac{1}{K_R} \int_0^{y_c} \frac{dy}{\frac{1}{4} \pi d^2} \quad (C-3)$$

and

$$y_c = \frac{\int_0^k (d^2)ydy}{\int_0^k (d^2)dy} \quad (C-4)$$

The reader should note that in the limit, as $R_1 + R_2 \rightarrow 0$, $T_R \rightarrow T_w$; so, for highly conductive, firmly bound elements the element temperature approaches the wall temperature. On the other hand, as $R_1 + R_2 \rightarrow \infty$, i.e., weakly conductive and/or loosely bound elements, the element temperature approaches a weighted average of the surrounding fluid temperature

$$\text{as } R_1 + R_2 \rightarrow \infty, T_R \rightarrow \frac{\int_0^k (d)HT(y)dy}{\int_0^k (d)Hdy} \quad (C-5)$$



- q = rate of heat transfer between element and fluid
- R_1 = conductive resistance between centroid and surface
- R_2 = contact resistance at boundary
- k = element height
- T_R = "temperature" of the element
- T_W = temperature of the substrate
- $T(y)$ = temperature of the fluid
- y_c = location of the centroid
- H = convective heat transfer coefficient
- d = local element diameter

Figure C-1. Roughness Element Heat Transfer Schematic and Nomenclature

INITIAL DISTRIBUTION

DTIC-DDAC	2
AUL/LSE	1
ASD/ENSZ	1
AFATL/DLODL	2
AFATL/CC	1
HQ USAF/SAMI	1
OO-ALC/MHWRB	1
AFIS/INT	2
HQ TAC/DRA	1
HQ USAFE/DOQ	1
HQ PACAF/DOQQ	2
HQ TAC/INAT	1
ASD/XRX	1
USA TRADOC SYS ANAL ACTY	1
COMIPAC (PT-2)	1
HQ PACAF/OA	1
USA BALLISTIC RESCH LAB	1
AFATL/CCN	1
AFATL/DLODA	1
FTD/SDNF	1
HQ AFSC/DLW	1
REDSTONE SCI INFO CNTR	1
NAVAL SYS CMD (TECH LIB)	1
NAVAL AIR TEST CNTR (CT/176)	1
SANDIA NATIONAL LABS	1
NWC (CODE 3205)	1
AFWAL/FIMM	1
NASA LANGLEY RSCH CNTR MS 406	1
AFWL/NTSA	2
THE RAND CORP (LIB-D)	1
AD/XRS	1
ASD/XR	1
AFATL/DLC	13
BMO/SYMS	1
AFWAL/FIMG	1
AFOSR/AEROSPACE SCIENCES	1
AFWAL/FIM	1